

ELECTRIC QUANTUM WALKS WITH INDIVIDUAL ATOMS

MASTER THESIS

BY

MAXIMILIAN GENSKE

FIRST SUPERVISOR: PROF. DR. STEPHAN SCHLEMMER
SECOND SUPERVISOR: PROF. DR. DIETER MESCHEDÉ



UNIVERSITÄT ZU KÖLN

ANGEFERTIGT IM
INSTITUT FÜR ANGEWANDTE PHYSIK
UNIVERSITÄT BONN

OCTOBER 23, 2012

Abstract

The experimental realisation of *electric quantum walks*, i.e. quantum walks that are subject to a force, is presented with individual caesium atoms. Hereby, the behaviour of a charged quantum particle in a static electric field is simulated in a time as well as space discrete system. Building on previous achievements [1], the demonstration of ordinary quantum walks of up to 100 steps is shown. Further thorough theoretical studies expose the underlying simulator properties of such a quantum walk system experiencing a force. Similarities to the continuous time analogon as well as characteristic features that are indebted to the discrete evolution of the system are presented. The implementation of a direct digital synthesizer allows the experimental application of discrete forces in the system by employing frequency ramps, and thus leads to the realisation of electric walks. Results are given for selected force parameters, showing the phenomenon of *Bloch oscillations*. Additionally, pure ballistic transport of the electric quantum walk due to strong Landau-Zener tunnelling in the strong force regime is demonstrated.

Contents

1. Introduction	1
2. The theory of 1D quantum walks	3
2.1. Quantum walks in position space	3
2.2. The Fourier picture of quantum walks	6
3. Experimental control of single atom systems	11
3.1. Experimental setup	11
3.2. Qubit preparation and manipulation	14
3.3. Spin-dependent transport	16
3.4. Acceleration of trapped atoms in an optical lattice	18
3.4.1. Principle of operation	18
3.4.2. The Direct Digital Synthesizer	19
3.4.3. Characterisation and performance of the DDS box	23
4. Quantum walks with individual atoms	29
4.1. The experimental walk operator	29
4.2. Experimental procedure	30
4.3. Spin-decoherence model	32
4.4. Results	34
5. Electric quantum walks	41
5.1. Theory	41
5.1.1. Bloch oscillations	41
5.1.2. Electric quantum walks in position space	42
5.1.3. Resonant tunnelling	45
5.1.4. The force effect in k -space	46
5.1.5. Spectrum of the electric walk operator	47
5.2. Experimental realisation	53
5.2.1. Procedure	53
5.2.2. Results	55
6. Conclusion and Outlook	63
A. DDS box	65
B. Characteristic polynomial of the electric walk operator	67
Bibliography	69

Chapter 1.

Introduction

Ever since the dawn of quantum mechanics the world of physics has come to face more and more counter-intuitive characteristics of nature. After the one-century lasting efforts to understand and describe this theory thoroughly, people finally started to make use of it by artificially constructing desired systems. However, increasing size and complexity of these make it very challenging - if not impossible - to test models and theories sufficiently. This is owing to the exponentially increasing demands of classical computation. Already in 1985 Richard P. Feynman, therefore, raised the idea of a quantum computer [2]. Throughout the years much work has been done on this, steadily advancing both on the theoretical and technological side, which has eventually opened the hunt for such a machine.

Closely related to this goal is the concept of quantum simulations. This encompasses the idea of mimicking quantum behaviour of complex, hardly controllable quantum systems with other well-controlled, decoherence-reduced ones. The aim is to get a deeper insight into characteristics and properties of the initial system by studying the artificially created one only. A very important role plays the field of cold atoms in this context. The invention of the laser technology in the 60's and later the development of laser cooling methods [3] have allowed scientists to work in a regime where atomic and molecular systems can be controlled and manipulated very precisely. Further cooling and trapping techniques [4] made it possible, for instance, to achieve a Bose-Einstein condensate - a quantum phase of matter [5,6] -, and to test exciting phenomena such as superfluidity by investigating vortices [7]. An optical lattice loaded with an ultracold gas of neutral atoms is able to reproduce periodic potentials which are typical for crystalline solids. For example, such a system could demonstrate the superfluid to Mott insulator transition [8]. Very importantly, an optical lattice also holds the chance to manipulate and investigate few-body systems, where usual approximations relying on a large number of particles are not applicable any more. A very fruitful accomplishment has been the manipulation and control of single-atom systems. This so-called bottom-up approach allowed the implementation of a conveyor belt for single atoms [9] or more recently a single atom interferometer [10], for instance.

In the race for realising a quantum simulator, a promising candidate is the so-called *quantum walk*. This is the quantum mechanical counter part to the well known classical random walk. Owing to quantum interferences during the walk steps, the distribution as well as other properties exhibit different behaviour than classically expected. Particularly the ballistic spreading of this kind of walk reflects the potential advantages over the diffusive classical one [11]. A positive aspect is the believed exponential speed up regarding classical algorithms [12,13]. Experimental proposals and realisations are manifold, ranging from trapped ions [14,15] over atoms in an optical cavity [16] to pure photonic systems [17]. At the focus of this thesis is the quantum walk which was previously realised in Prof. Meschede's group by means of single neutral Caesium atoms in a one-dimensional optical lattice [18]. Improved results of this experimental quantum

walk are presented in chapter 4.

Experimentally, quantum walks are in general still very challenging, and only recently they could be extended to two dimensions in an optical fiber network [19]. Theoretically, however, the investigations have developed to a considerable state. It became apparent that quantum walks are not just interesting in the light of quantum algorithms, but can serve as a quantum simulator of complex systems in its own right due to the discreteness of the system [20]. It could be shown that the quantum mechanical interaction of two "walkers" lead to a novel molecular binding mechanism [21]. Furthermore, quantum walks in a random environment reveal the effect of Anderson localisation [22]. Even the topic of topological phases can be tackled with quantum walks [23].

The main focus of this thesis is on quantum walks that are subject to a force. Due to its formal resemblance to an electron in a static electric field this shall be called *electric quantum walk*. A detailed theoretical treatment of such a quantum walk system is outlined in chapter 5, showing also the quantum transport phenomenon of *Bloch oscillations* that is typically exhibited by associated electrons. Usually, low coherence times make it impossible to observe these oscillations in solid materials directly. They have therefore first been demonstrated by using ultracold atoms in optical lattices just a couple of decades ago [24–26]. Quantum walks make it possible to simulate, and to study this continuous time effect also in a discrete time and space environment. Building on previous achievements in Prof. Meschede's group, electric quantum walks shall now be shown experimentally in single-atom systems. The necessary force is induced in the set-up by acceleration of the 1D optical lattice. This is achieved by controlling the dynamics of both lattice arms independently by means of a direct digital synthesizer (see chapter 3). The high reliability of this device allows for a textbook-like application of the force, herewith realising the first electric quantum walks with individual atoms. Corresponding results can be studied in chapter 5.

Chapter 2.

The theory of 1D quantum walks

The classical random walk is a crucial concept in the realm of stochastic. Subsequently, the idea found its way to other areas such as economics [27] or biology [28], for example. The random walk describes a trajectory in which the walker makes consecutive left-or-right decisions. For the one-dimensional case, the resulting distribution is of well-known Gaussian form, and hence has a *diffusive* temporal spreading [29]. This walk can generally occur in a discrete as well as in a continuous fashion. Depending on the circumstances the respective model is chosen.

The quantum version of the random walk works analogously to its classical counterpart. Here, however, instead of probabilities, quantum mechanical probability amplitudes have to be considered. The idea is to utilise internal states in order to bring the system into a coherent superposition, and subsequently to delocalise the system over the spatial structure depending on its internal state. Both operations are individually described by a unitary operation acting on the quantum system. While being coherently delocalised, the system's probability amplitudes can interfere, hereby causing classically unexpected behaviour. The most pronounced feature is a *ballistic* expansion of the walk's spatial distribution. The quantum walk (QW or "walk") was first introduced by Aharonov et al. in 1993 [11]. Henceforth, it has drawn some considerable attention on the theoretical as well as experimental side. The reason for this can be found in its potential regarding quantum information processing, i.e. its possible contribution to quantum algorithms [13]. The quantum walk can generally be performed in a many-dimensional space. In the following only the discrete and one-dimensional case shall be at the focus of interest. First, the mathematical setting shall be lined out followed by an example of a system performing the quantum walk in position space. Afterwards, the remarkable properties of a quantum walk are explained more fundamentally by considering the underlying mathematical system in its momentum space representation.

2.1. Quantum walks in position space

The system under consideration has two internal quantum states, and is often abbreviated as *qubit* or two-level *spinor*. For reasons that will become apparent below, the two-fold Hilbert space spanned by the spinor basis states $\{|\uparrow\rangle, |\downarrow\rangle\}$ is called *coin-space*, with $\mathcal{H}_{\text{coin}} = \mathbb{C}^2$. On top of that, the system is confined to a one-dimensional line with discrete positions. So let $\mathcal{H}_{\text{space}} = \ell^2(\mathbb{Z})$ be the Hilbert space spanned by the position basis states $\{|n\rangle : n \in \mathbb{Z}\}$. The total Hilbert space \mathcal{H}_{tot} connects both subspaces via their tensor product, i.e. $\mathcal{H}_{\text{tot}} = \mathcal{H}_{\text{space}} \otimes \mathcal{H}_{\text{coin}}$. The full states existing in this Hilbert space are of the form $|\psi\rangle = |n\rangle \otimes |s\rangle^1$, where $s = \{\uparrow, \downarrow\}$. It is noteworthy at this point that real physical systems are described by spatially continuous wavefunctions rather

¹Define $|n\rangle \otimes |s\rangle = |n, s\rangle$ in favour of abbreviation.

than discretised states. This picture, however, remains a very good approximation for quantum particles of small finite width confined to particular points in space. This, for instance, is the case for cold atoms in optical lattices. So in favour of simplicity one shall stick to the outlined mathematical model, as also presented in [13].

At each step the walker has to make a decision on going into one of the two possible directions with a certain probability. The idea is to store the information within the internal states of the system. In the formalism of quantum mechanics an operator determines the properties of such a system. Hence, the probability of moving right or left is induced by the so-called *coin-operator* \hat{C} , which represents a unitary transformation. The name resembles the classical case situation of flipping a coin at each position in order to make a directional decision. The action of this operation can be understood as a rotation in the coin-space $\mathcal{H}_{\text{coin}}$. Geometrically, this Hilbert space is interpreted as a sphere - the so called Bloch sphere [30]. Every spinor state of the system is represented by a point on this sphere and its corresponding Bloch vector. The spin observable is commonly expressed in terms of a linear combination of the three Pauli matrices and the identity matrix, since the set $\{\sigma_i : i = 0, 1, 2, 3\}$, where $\sigma_0 = \mathbb{1}$, spans the full vector space of two-dimensional Hermitian matrices [31]. So a rotation in the coin-space can be understood as a rotation of the Bloch vector that is generated by the Pauli matrices. The resulting unitary coin operation can therefore be written as $\hat{C}_{\text{gen}}(\theta) = e^{-i\gamma} e^{-i\theta \mathbf{r} \cdot \boldsymbol{\sigma} / 2}$, where \mathbf{r} is the axis about which the system is rotated by θ , $\boldsymbol{\sigma}$ is the vector of Pauli matrices, and $e^{-i\gamma}$ represents a global phase accumulation. This rotation can be alternatively expressed in matrix form. Following the unitarity conditions one can define the most general coin as

$$\hat{C}_{\text{gen}}(\theta) = e^{-i\gamma} \begin{pmatrix} \cos(\theta/2) e^{i\alpha} & -\sin(\theta/2) e^{-i\beta} \\ \sin(\theta/2) e^{i\beta} & \cos(\theta/2) e^{-i\alpha} \end{pmatrix}, \quad (2.1)$$

where $(\alpha, \beta, \gamma, \theta) \in \mathbb{R}$, and $0 \leq (\alpha, \beta, \gamma) \leq 2\pi$, $0 \leq \theta \leq \pi$. In the Bloch sphere picture the parameters α, β, γ describe the orientation of the axis of rotation and θ is the angle by which the system is rotated. The latter is equivalent to a statement about the imbalance of the coin. To obtain an unbiased (or balanced) coin the system needs to be rotated by $\theta = \frac{\pi}{2}$. For the walker this means to have equal probabilities in going to the left and right, respectively, and therefore imitating in a single event the classical balanced coin-flip.

After having set the spinor- or spin states, the actual translation of the system has to be performed. A unitary shift operator \hat{S} can be formulated in such a way that it coherently translates the system exactly one position state to the right or left according to its spin state, respectively. The mathematical form reads

$$\hat{S} = \begin{cases} |n, \uparrow\rangle \rightarrow |n+1, \uparrow\rangle \\ |n, \downarrow\rangle \rightarrow |n-1, \downarrow\rangle \end{cases}. \quad (2.2)$$

Consecutive application of coin- and shift operator results in one quantum walk step. So the unitary walk-operator \hat{W} acting on the total Hilbert space \mathcal{H}_{tot} , which combines both actions, can be formulated as

$$\hat{W} = \hat{S} \cdot (\hat{\mathbb{1}}_{\text{space}} \otimes \hat{C}) \quad , \quad (2.3)$$

where $\hat{\mathbb{1}}$ represents the identity-operator, reflecting that \hat{S} acts on $\mathcal{H}_{\text{space}}$ as well as $\mathcal{H}_{\text{coin}}$, whereas \hat{C} acts on $\mathcal{H}_{\text{coin}}$ only. A full quantum walk of N steps is obtained by iteratively applying the one-step operator \hat{W} N times to an initial state $|\psi_0\rangle$, i.e.

$$|\psi_N\rangle = \hat{W}^N |\psi_0\rangle. \quad (2.4)$$

(a) Random Walk											(b) Quantum Walk												
	-5	-4	-3	-2	-1	0	1	2	3	4	5		-5	-4	-3	-2	-1	0	1	2	3	4	5
0						1						0						1					
1					$\frac{1}{2}$		$\frac{1}{2}$					1					$\frac{1}{2}$		$\frac{1}{2}$				
2				$\frac{1}{4}$		$\frac{1}{2}$		$\frac{1}{4}$				2				$\frac{1}{4}$		$\frac{1}{2}$		$\frac{1}{4}$			
3			$\frac{1}{8}$		$\frac{3}{8}$		$\frac{3}{8}$		$\frac{1}{8}$			3			$\frac{1}{8}$		$\frac{1}{8}$		$\frac{5}{8}$		$\frac{1}{8}$		
4		$\frac{1}{16}$		$\frac{4}{16}$		$\frac{6}{16}$		$\frac{4}{16}$		$\frac{1}{16}$		4		$\frac{1}{16}$		$\frac{2}{16}$		$\frac{2}{16}$		$\frac{10}{16}$		$\frac{1}{16}$	
5	$\frac{1}{32}$		$\frac{5}{32}$		$\frac{10}{32}$		$\frac{10}{32}$		$\frac{5}{32}$		$\frac{1}{32}$	5	$\frac{1}{32}$		$\frac{5}{32}$		$\frac{4}{32}$		$\frac{4}{32}$		$\frac{17}{32}$		$\frac{1}{32}$

Figure 2.1.: Spatial probability evolution of (a) the classical random walk and (b) the quantum Hadamard walk for 5 steps. Already after 3 steps the distribution of (b) reveals a signature of the quantum world. The probabilities that deviate from the classical values are highlighted: orange for higher and green for lower values than the classical counterpart.

The real space distribution of this walk can then be acquired by projecting the state $|\psi_N\rangle$ onto every position state $|n\rangle$. Owing to the system's spinor structure, one needs to perform the projection for both spin states in order to gain a total probability distribution.

Clearly, the properties of the walk strongly depend on the initial state $|\psi_0\rangle$, and more importantly on \hat{C} . According to (2.1) all sorts of coin-operators can be realised. In the following, however, a standard example of the quantum walk in the unbiased case shall be presented. This also allows for direct comparison with the balanced classical random walk. A frequently used operator in this context is the so-called *Hadamard-coin* \hat{C}_H , and is defined as

$$\hat{C}_H = \frac{1}{\sqrt{2}} \begin{pmatrix} 1 & 1 \\ 1 & -1 \end{pmatrix} \quad \text{or} \quad \hat{C}_H = \begin{cases} |\uparrow\rangle \rightarrow \frac{1}{\sqrt{2}}(|\uparrow\rangle + |\downarrow\rangle) \\ |\downarrow\rangle \rightarrow \frac{1}{\sqrt{2}}(|\uparrow\rangle - |\downarrow\rangle) \end{cases}, \quad (2.5)$$

where the latter might give a more demonstrative picture of the effect on the system. One can see that this form can be obtained from (2.1) by setting $\alpha = \pi/2$, $\beta = \pi/2$, and $\gamma = \pi/2$.

In order to get a better intuition of the evolution of a quantum walk with $\hat{C} = \hat{C}_H$, position probabilities for the first five steps of a walker with initial state $|\psi_0\rangle = |0, \uparrow\rangle$ are explicitly presented in table 2.1. Discrepancies between the quantum and the classical random walk are visible for such small numbers of N . After the first two steps the quantum walk is identical to the classical version. However, this changes after the third step. The coin operation \hat{C} then causes the spinor states located in the same position state to interfere. Consequently, this gives rise to an altered spatial probability distribution compared to the classical analogon. Looking at quantum walks in position space for a larger number of steps, one can clearly see distinct characteristics (see figure 2.2). It becomes immediately apparent that the quantum walk peaks at off-center positions of the distribution. For a well defined initial spin state the walk shows a strongly asymmetric behaviour, where the orientation of the initial spin determines also the orientation of the asymmetry (see figure 2.2(b)). The intuitive picture of this behaviour is the following: since the Hadamard coin does not treat the two spinor states equally, the walker experiences constructive interference in the one and destructive interference in the other direction. Alternatively, an initial state of equal, but complex superposition of both internal states is considered, e.g. $|\psi_0\rangle = \frac{1}{\sqrt{2}}(|0, \uparrow\rangle + i|0, \downarrow\rangle)$. Owing to the real structure of the Hadamard coin the real part of the walker never mingles with the complex part, and vice versa. Consequently, no interference can occur between those

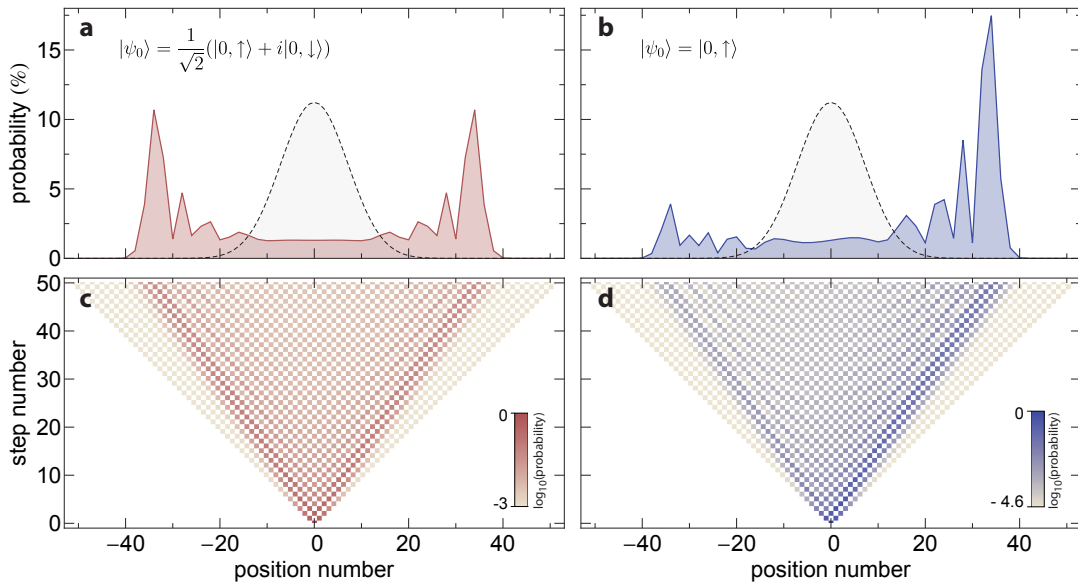


Figure 2.2.: Distribution of a 50-step quantum walk with (a) an equal, but imaginary superposition of the two qubit states, and (b) a spin-up configuration. The symmetric classical distribution is plotted in both cases in gray for comparison. The evolution of the respective quantum walk probability distribution is shown in (c) and (d), respectively. Here, the confinement of the walk to the $N/\sqrt{2}$ region for the Hadamard walk as well as the almost homogeneous spreading between the peaks can be nicely observed. Probabilities are plotted for even, i.e. non-zero, position numbers only.

two parts, leading to two independent asymmetric walks in opposite directions (see figure 2.2(a)).

As touched on before, the standard deviation of a classical random walk is well-known to follow a diffusive behaviour, namely $\sigma = \sqrt{N}$. Here, σ denotes the standard deviation. Contrary to this, the quantum walk displays a ballistic relation, i.e. $\sigma \propto N$. For example, analytical analysis of the balanced quantum walk proves a spreading over an interval $[-N/\sqrt{2}, N/\sqrt{2}]$ (see section 2.2). This linear dependence is the origin for a potential speed up of algorithms based on quantum rather than classical random walks. The confinement can be visually confirmed by looking at figure 2.2. Generally, the exact details of a certain quantum walk are determined by the form of the chosen coin operator \hat{C} and the initially prepared state $|\psi_0\rangle$. A closer look at the dynamics of such a general quantum walk shall be taken in the following.

2.2. The Fourier picture of quantum walks

To obtain deeper insight into characteristics and properties of the described quantum walk, it is useful to look at the underlying discrete evolution operator \hat{W} . Due to the discreteness of space, the spatial translational invariance of the system is also discretised, which naturally demands a momentum representation of the system. The spatial periodicity results in a finite-sized k -space. To be able to describe the dynamics of a system, one typically calculates the dispersion relation, i.e. the energy as a function of the momentum. Conceptionally, it is crucial to realise that the evolution described by the step operator is approximately equivalent to the evolution generated by an effective

time-independent Hamiltonian \hat{H}_{eff} . It holds that

$$\hat{W} = e^{-i\hat{H}_{\text{eff}}\Delta t/\hbar}, \quad (2.6)$$

where Δt corresponds to the time duration of a single step. So a walk of N steps stroboscopically simulates the evolution generated by the Hamiltonian \hat{H}_{eff} at times $N\Delta t$. From this relation it can be seen that the eigenvalues of \hat{H}_{eff} are defined only up to 2π (define $\hbar = \Delta t = 1$). It can then be proven that the spectrum of \hat{H}_{eff} indeed describes the asymptotic dynamics of the quantum walk [32]. Note that similar to the fact that momentum becomes quasi-momentum in the presence of a spatial periodic structure, energies become *quasi-energies* in the case of a temporal periodicity [23].

The momentum representation is gained by using common Fourier transformation going from the initial real state basis $\{|n\rangle : n \in \mathbb{Z}\}$ to the momentum state basis $\{|k\rangle : k \in \mathbb{K}\}$, i.e. transforming $\mathcal{H}_{\text{space}} = \ell^2(\mathbb{Z})$ into $\mathcal{H}_k = L^2(\mathbb{K})$, where $\mathbb{K} = [-\pi, \pi]$. The corresponding algebraic operations are

$$|n\rangle = \frac{1}{\sqrt{2\pi}} \int dk e^{-ikn} |k\rangle \quad \text{and} \quad |k\rangle = \frac{1}{\sqrt{2\pi}} \sum_n e^{ikn} |n\rangle. \quad (2.7)$$

In order to apply this transformation to the system \hat{W} , one needs to express \hat{C} and \hat{S} (see (2.1) and (2.2)) explicitly in terms of the position states $|n\rangle$. The coin operation only acts on $\mathcal{H}_{\text{coin}}$, i.e. is diagonal on $\mathcal{H}_{\text{space}}$ and thus also diagonal on \mathcal{H}_k . Consequently, even in the momentum basis the coin operation is fully represented by a 2×2 unitary matrix. The shift operator, however, acts on both subspaces of the Hilbert space \mathcal{H}_{tot} . The Fourier transformation of \hat{S} into \hat{S}_k yields

$$\hat{S} = \sum_n |n+1\rangle\langle n| \otimes |\uparrow\rangle\langle\uparrow| + \sum_n |n-1\rangle\langle n| \otimes |\downarrow\rangle\langle\downarrow|, \quad (2.8)$$

$$\xrightarrow{\text{FT}} \hat{S}_k = \underbrace{\int_{-k}^k dk |k\rangle\langle k|}_{\hat{\mathbb{1}}_k} \otimes \underbrace{\left[e^{-ik} |\uparrow\rangle\langle\uparrow| + e^{ik} |\downarrow\rangle\langle\downarrow| \right]}_{\hat{S}_k^{\text{spin}}}. \quad (2.9)$$

While in the position state basis \hat{S} naturally couples two adjacent states, in the momentum representation the shift operator couples the momentum variable k to the spin state, but is diagonal in the state $|k\rangle$. The resulting walk operator \hat{W}_k acting on the new total Hilbert space $\mathcal{H}_{\text{tot}} = \mathcal{H}_k \otimes \mathcal{H}_{\text{coin}}$ can then conveniently be written as

$$\hat{W}_k = \hat{S}_k \cdot (\hat{\mathbb{1}}_k \otimes \hat{C}) = \hat{\mathbb{1}}_k \otimes \underbrace{(\hat{S}_k^{\text{spin}} \cdot \hat{C})}_{\hat{W}_k^{\text{spin}}}. \quad (2.10)$$

Hence, the quantum walk in the momentum representation can be reduced to a system acting on the spinor states only. Using matrix formalism, the system reveals a diagonal form composed of 2×2 block matrices given by the product $(\hat{S}_k^{\text{spin}} \cdot \hat{C})$. Assuming \hat{C} is of general form (2.1), the system can now be explicitly expressed in its reduced version

$$\hat{W}_k^{\text{spin}} = \begin{pmatrix} e^{-ik} & 0 \\ 0 & e^{ik} \end{pmatrix} \cdot \hat{C}_{\text{gen}}(\theta) = e^{-i\gamma} \begin{pmatrix} \cos(\frac{\theta}{2}) e^{i\alpha} e^{-ik} & -\sin(\frac{\theta}{2}) e^{-i\beta} e^{-ik} \\ \sin(\frac{\theta}{2}) e^{i\beta} e^{ik} & \cos(\frac{\theta}{2}) e^{-i\alpha} e^{ik} \end{pmatrix}. \quad (2.11)$$

The analysis of the quantum walk boils down to diagonalising the matrix given in (2.11). Owing to its unitary nature, the matrix' eigenvalues are points on the complex

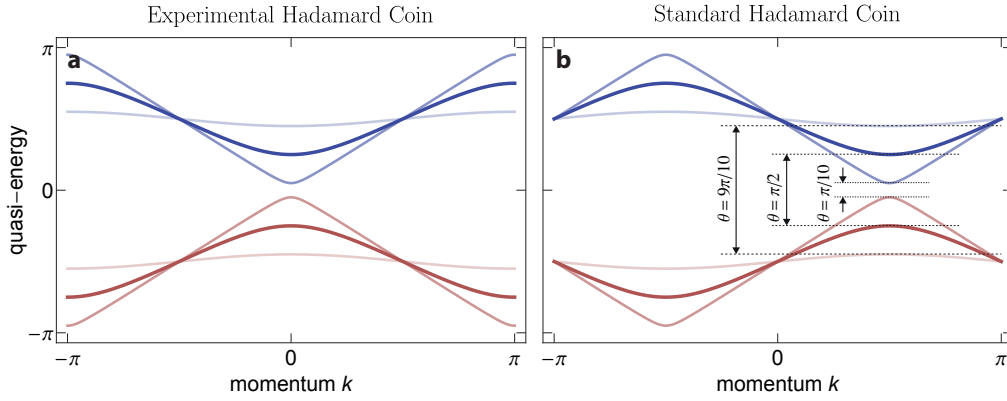


Figure 2.3.: Quasi-energy bands for (a) the experimental Hadamard- and (b) the standard Hadamard-coin as defined in the text. The latter is rescaled in order to be centred about the x-axis. The coin angles are $\theta = 9\pi/10$, $\pi/2$ and $\pi/10$, and corresponding bands are assigned by the labelled band gaps in (b). Respective bands of (a) and (b) are shifted against each other, but they describe the same dynamics. This is robust against any change of the coin.

unit circle. By bringing the eigenvalues into the form $\lambda = e^{i\omega}$, the quasi-energies of the system are solely determined by ω . One can then show that

$$\omega_{\pm} = \gamma \pm \arccos [\cos(k - \alpha) \cos(\theta/2)] . \quad (2.12)$$

The corresponding eigenvectors of the system in the spinor-basis are given by

$$\hat{e}_{\omega}^{\pm}(k) = N(k) \begin{pmatrix} 1 \\ \frac{e^{i\beta}}{\sin(\theta/2)} [\cos(\theta/2) e^{i\alpha} - e^{i\gamma} e^{ik} e^{i\omega_{\pm}}] \end{pmatrix}, \quad (2.13)$$

where the normalisation constant $N(k)$ can be calculated to be

$$N(k) = \frac{1}{\left[2 + \frac{2}{\tan^2(\theta/2)} - \frac{2}{\tan(\theta/2) \sin(\theta/2)} \cos(\omega_{\pm} + k + \gamma - \alpha) \right]^{1/2}} . \quad (2.14)$$

The quantum walk is asymptotically described by a pair of quasi-energy bands. Focussing first on the eigenvalues, it can be seen that the dynamics are fundamentally the same for all coins that are equally biased, i.e. have a fixed angle θ . Although the rotation parameters α and γ enter the relations, they only cause a horizontal or vertical shift of the bands, respectively. The latter can even be fully neglected by rescaling the quasi-energy appropriately. The off-diagonal parameter β does evidently not have an impact on the dispersion relation at all. Contrary to this, the angle θ dominates the shape of the curves. In figure 2.3 the quasi-energy ω is plotted as a function of k for two coin realisations: The angle-dependent Hadamard coin $\hat{C}_H(\theta)$ with $\alpha, \beta, \gamma = \pi/2$, and one that imitates the Euclidean space rotation matrix² resulting from setting $\alpha, \beta, \gamma = 0$. The latter shall also be referred to as the *experimental Hadamard* coin $\hat{C}_{EH}(\theta)$. For both coins the balanced version for $\theta = \pi/2$ as well as the cases $\theta = \pi/10$ and $\theta = 9\pi/10$ are shown. The latter angles describing the situations in which the spin is nearly flipped or untouched, respectively. The corresponding

²Euclidean rotation matrix: $R(\theta) = \begin{pmatrix} \cos(\theta/2) & -\sin(\theta/2) \\ \sin(\theta/2) & \cos(\theta/2) \end{pmatrix}$

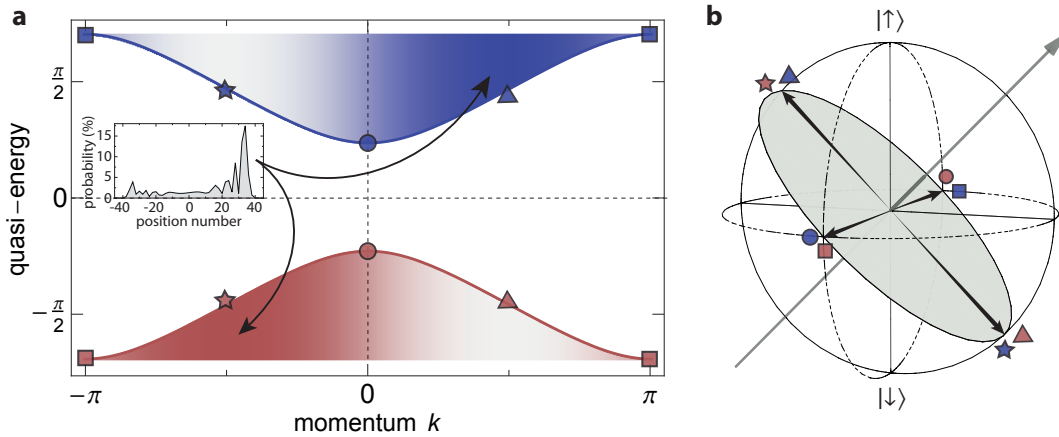


Figure 2.4.: In (a) quasi-energy bands of a balanced quantum walk are plotted. Shaded regions represent the magnitude of the corresponding projection amplitude of an initial system $|\psi_0\rangle = |0, \uparrow\rangle$ onto \hat{e}_ω^\pm . Hereby, the quantum walk's shape (inset) can be explained. In (b) the plane is shown in which the Bloch vector rotates, while going along the bands. Selected points are marked accordingly. Due to the orthogonality of the bands both Bloch vectors are always π out of phase.

quasi-energies (2.12) approach a linear or constant form in these limits accordingly. When scanning the angle θ , one can see that the dispersion relations' crossing opens up and forms a band gap. This gap steadily equals twice this angle in magnitude and maximises for $\theta = \pi$.

In order to investigate the details of a specific initial system performing the quantum walk, its projection onto the "walk"-system is considered. Assuming the system is initially localised in space, Fourier transformation reveals an equal population of all k -states (see (2.7)). Consideration of the spin degree of freedom shows that the eigenstates of a quantum walk are linear combinations of the original spinor eigenstates, and that they have an intrinsic k -dependence (see (2.13)). Therefore, for a given k an initial spin state $|s\rangle$ maps itself onto the two branches of the dispersion relation with varying individual amplitudes a and b , hereby respecting $a\hat{e}_\omega^+(k) + b\hat{e}_\omega^-(k) = \frac{1}{\sqrt{2\pi}}|s\rangle$, where $a, b \in \mathbb{C}$. Nonetheless, the eigenstates \hat{e}_ω^\pm are still represented as points on the same Bloch sphere as before. In fact, when following one of the bands, the k -dependence of the eigenstate lets the Bloch vector follow the trajectory of a circle in a plane cutting the Bloch sphere under an angle of $\theta/2$ as illustrated in figure 2.4(b) [23].

Ultimately, finding $|a|^2$ and $|b|^2$ gives a quantitative picture of the projection. In figure 2.4(a) these quantities are represented by the color above and underneath the bands. Here, the coin was chosen to be $\hat{C}_{\text{EH}}(\pi/2)$ and the initial state was $|\psi_0\rangle = |0, \uparrow\rangle$. The intensity of the color is proportional to the magnitudes of a and b , indicating the expected non-uniform projection. The dynamics of the corresponding quantum walk can now be directly understood by considering the band structure of the underlying static effective Hamiltonian. From figure 2.4(a) it can be seen that most of the initial state projects onto one side of a respective band only. The bands share the same tangential direction at those sides. Knowing that the group velocity of the system is given by $\frac{\partial\omega}{\partial k}$, and realising that most of the system is located on the band where $\frac{\partial\omega}{\partial k}$ is largest in magnitude, leads to the understanding that most of the wave packet travels with maximally allowed speed. The direction of movement is governed by the sign of the tangent. This is indeed what can be observed from the inset of figure 2.4(a),

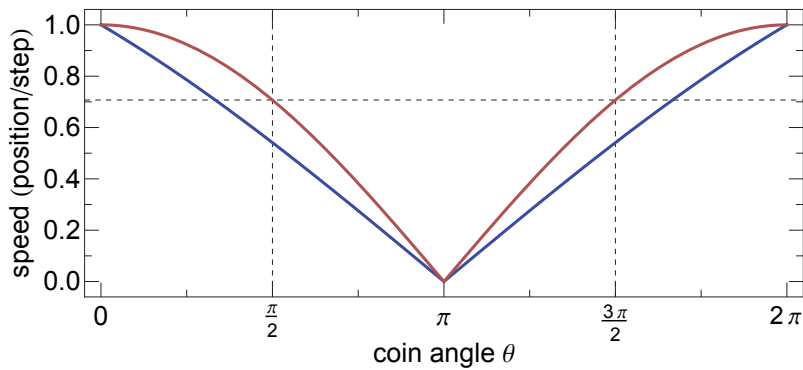


Figure 2.5.: Plotting the quantum walk's RMS speed v^{RMS} (blue) as well as the maximum speed $|v_g^{\text{max}}|$ (red) as a function of the coin angle θ . Both graphs show a very strong coin dependence, where the two extrema are represented by not having a coin at all ($0, 2\pi$) and causing full spin-flips (π).

and what was shown previously (figure 2.2). It explains on a dynamical level why the distribution shows peaks close to its edges, therefore explaining the ballistic nature of the walk.

Furthermore, the analytic form of the bands allow for a more quantitative analysis of the dynamics. Differentiation of (2.12) results in an expression of the velocity, i.e.

$$v_g(k) = \frac{\partial \omega_{\pm}}{\partial k} = \pm \frac{\cos(\theta/2) \sin(k - \alpha)}{\sqrt{1 - \cos^2(k - \alpha) \cos^2(\theta/2)}}, \quad (2.15)$$

which in turn allows for the calculation of the maximum speed of the walk, yielding

$$v_g^{\text{max}} = \pm \cos(\theta/2). \quad (2.16)$$

The units of these quantities are position number per step. For a balance walk ($\theta = \frac{\pi}{2}$) the maximal speed is therefore $1/\sqrt{2}$. The peak of the walk is consequently at around $N/\sqrt{2}$ as already stated above. Additionally, by integrating the squared velocity over the entire k -space the speed of the root-mean-square value (RMS) can be obtained as follows

$$v^{\text{RMS}} = \sqrt{\frac{1}{2\pi} \int_{-\pi}^{\pi} v_g^2(k) dk} = \sqrt{1 - \sin(\theta/2)}. \quad (2.17)$$

Figure 2.5 shows the RMS speed as well as the maximum speed as a function of the coin angle. The strong dependence on the angle originates from the fact that a change in θ translates into an in-/decrease of the band gap, which in turn leads to flatter or steeper flanks of the bands, respectively. It shall be again stressed that this picture applies only in an asymptotic context. A few number of steps are not represented by this very clearly.

In conclusion, the Fourier picture allows to see the quantum walk as a quantum mechanical simulator in its own right. The effective description of this time-discrete system by energy-bands allows for investigations of associated quantum mechanical effects. Thus, it is not only worthwhile to experimentally realise a quantum walk (see chapter 4), but also to probe the properties of the predicted energy bands. One associated effect is called *Bloch oscillations* [33] and deals with the transport properties in such a system. Entering the momentum space description by applying a force to the system, allows to test the corresponding motional behaviour. This shall be subject to further theoretical and experimental investigations in chapter 5.

Chapter 3.

Experimental control of single atom systems

The usage of individual atoms as quantum mechanical objects of study requires experimental access to internal as well as external degrees of freedom. The experimental setup presented here utilises single caesium atoms and a one-dimensional optical lattice for spatial trapping. Previously, this has led to the realisation of an atom interferometer [10] and also to the first demonstrated quantum walks in such a system [18]. This chapter first introduces the general setup, before methods for internal state control and the employed spin-dependent transport scheme are outlined. This is followed by a section on a newly installed technology which enables to control the global motion of the system.

3.1. Experimental setup

The general setup was installed in the past and is presented in great detail in [1, 34]. Although most features have been maintained, changes to the apparatus have been made in favour of improvement and experimental capability. The most noteworthy being the change from a one arm arrangement, in which the laser beam was retro-reflected to form the lattice, to a configuration where the optical standing wave is now formed by two individual counter propagating light beams. The latest layout of the apparatus can be seen in figure 3.1. All experiments described in the following were done using this arrangement.

The setup is based on a titanium:sapphire laser (Ti:Sa) which provides the optical power for the used one-dimensional lattice. The emitted light has a frequency of about 865.9nm. The initial laser beam is split into two individual arms. Both of them are guided through acousto-optic modulators (AOM) that allow for intensity stabilisation and frequency control settings in the MHz-range. Subsequent coupling into optical fibres guarantee a good wavefront quality in the following. Standard $\lambda/4$ and $\lambda/2$ waveplates are used to gain linearly polarised beams up to a purity¹ of 10^{-5} , before they enter the vacuum cell and form the one-dimensional optical lattice with a characteristic spacing of $\lambda/2 = 433\text{nm}$. Before atoms are trapped to the lattice, they are pre-cooled by means of a magneto-optical trap. With a microwave antenna the two ground states of caesium can be coherently coupled via electro-magnetic radiation in order to perform qubit manipulation operations (see section 3.2). An electro-optic modulator (EOM) is used to allow for qubit state-dependent transport by rotating one of the arms linear polarisation (see section 3.3). Finally, trapped atoms are illuminated for imaging with the same beams that also serve as optical molasses. The imaging can occur in a spin-dependent or -independent fashion, respectively. The former requires the so called

¹The EOM limits this purity to 10^{-4} in the respective dipole trap arm.

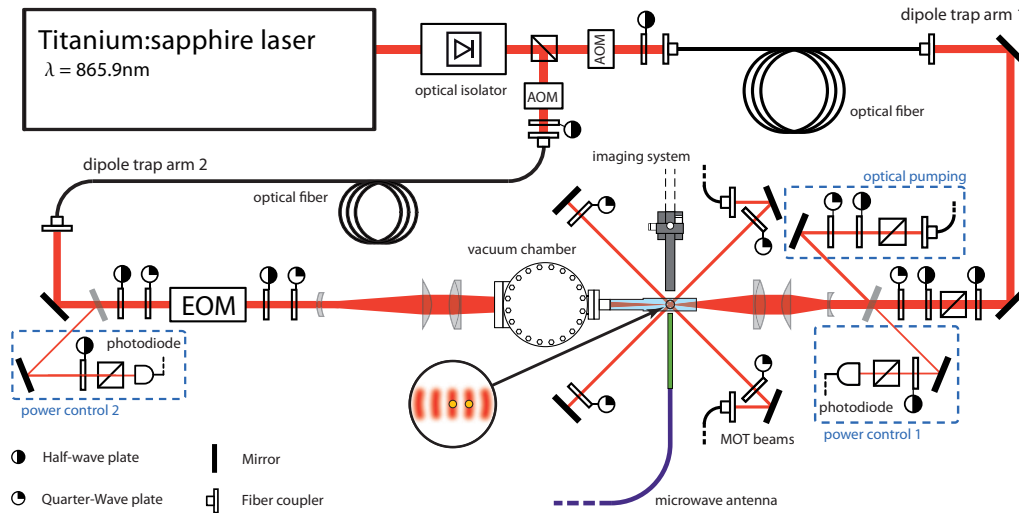


Figure 3.1.: Experimental setup. Adapted from [1].

push-out technique [35]. Numerical post-analysis of images crucially allows single site detection of the atoms.

MOT The MOT has become the standard tool to (pre-)cool and trap dilute atom gases. It is therefore intensively studied in the literature, see [3, 36, 37]. The working principle is based on radiation pressure generating a velocity-dependent damping force (molasses). An additional quadrupole field lets this force become directional by exploiting the intrinsic spin of the photons and the associated selection rules in the light-matter interaction process. The MOT employed in the presented experiment utilizes the D_2 -Caesium transition line at 852.3nm [38] to cool down the atoms by means of appropriate spectroscopically frequency stabilised laser beams. For the actual cooling process the $|F = 4\rangle \rightarrow |F' = 5\rangle$ cyclic transition is used. Additional repumping needs to be operated on the $|F = 3\rangle \rightarrow |F' = 4\rangle$ to guarantee the compensation of undesired decaying processes. From the very dilute background gas ($\sim 3 \times 10^{-11}$ mbar) sufficiently many caesium atoms are caught and subsequently cooled below $100\mu\text{K}$. Once this temperature is achieved, further spatial trapping by the optical lattice becomes possible. Here, the quantities depend in detail on the adjustment of the experimental parameters.

1D optical lattice Optical lattices are based on the fact that off-resonant light-matter interaction causes a conservative potential [39]. The attractive or repulsive nature of the resulting force depends on the sign of the detuning. The trap employed here is red-detuned, and hence attracts atoms to regions of high light intensity. The operated Ti:Sa has a typical output power of about 3.2W at an operation wavelength of $\lambda = 865.9\text{nm}$. The phase- as well as frequency stability is achieved by internal electronics, plus the use of an external cavity in the latter case. Frequency tuning can be achieved by changing the characteristics of the internal resonator and/or altering the RF-signal controlling the AOMs. The installed two-arm setup requires phase stability of the signals driving the respective AOMs. This is achieved by a direct digital synthesizer (DDS), which phase locks its two individual outputs, and additionally allows for efficient frequency ramping (see section 3.4). At the same time, the AOMs are used to set the intensities of the

individual lattice arms, and are utilised for the intensity stabilisation of such. A fraction of each arm's laser power is extracted and monitored with a fast photodiode (1MHz bandwidth). Home-built servo amplifiers combined with voltage-controlled attenuators (VCA - ZX73-2500+ by minicircuits) are then able to correct the RF-signal's amplitude, and thus the intensity of the diffracted light with a bandwidth of about 50kHz. The set point is assigned by either the computer control or a manual voltage source. The overlap of both beams, which ultimately leads to the lattice inside the vacuum chamber is gained by optimising the coupling of one lattice arm into the opposite fibre coupler. Furthermore, the linear polarisations of both arms need to be aligned such that their relative angle is as close to zero as possible (see section 3.3). Just before the vacuum chamber the beams are focused by means of a respective telescope. The resulting beam waist is $w_0 = 18\mu\text{m}$ for both dipole trap arms. However, it could be measured that the corresponding intensities vary in the usual trapping region of the atoms. Due to a relative shift of the focii, dipole trap arm 1 (DT1) provides twice as high intensities in this region than DT2 for identical beam powers. Moreover, while the DT1 laser arm only has to pass the glass cell before hitting the atoms, the DT2 beam needs to traverse a vacuum chamber window. It could be measured that the window has a considerable impact on the purity of the linear polarisation due to a strain-induced birefringence. The optical retardation is about $\lambda/50$. An optimal angle of orientation with respect to the optical table was found to be about 58° (plus multiples of 90°), corresponding to the eigenaxes of the glass window.

Atoms are initially loaded into an optical trap with a depth of about 0.4 mK. Additional molasses cooling allows to decrease the atoms' temperature further to $\sim 10\mu\text{K}$. By collecting the fluorescing photons, imaging of the system can be performed (see below). For the actual experimental sequence the trap depth is adiabatically lowered to about $100\mu\text{K}$ by decreasing the light intensities accordingly. Next to these intensities, the trap frequencies of the lattice depend on the waist for the radial, and on the wavelength for the axial direction, respectively [39]. The usually employed beam power of 6 mW in both arms then leads to a radial trap frequency of about 1 kHz. The axial trap frequency can be measured to be 80 kHz.

Detection system The correct analysis and interpretation of the presented single atom system requires the measurability and detection of such atoms with a resolution below a single lattice site. As mentioned above, the imaging processes comprises the collection of fluorescence photons. The used self-assembled objective of numerical aperture $\text{NA} = 0.29$ has an intrinsic diffraction limit of ~ 5 lattice sites. The fluorescence signal is viewed by an EMCCD camera which allows single photon detection. The pixel-to-meter calibration constant is ≈ 1.47 (pixel/lattice site). The amount of collected photons is clearly dependent in detail on the characteristics of the molasses beams, but the detection rate for the usually employed settings is about 75000 counts/s. For single-site resolution imaging the camera exposure time² is usually 1 s. Numerical post-processing of the taken image is then carried out by means of an advanced deconvolution algorithm respecting the discrete spatial separation of the atoms and their fluorescence strength. Hereby, single-site resolution detection is finally achievable with an efficiency of up to 99%. Again, a description at length of all components of this imaging set-up can be found in [1].

²In preliminary characterisation measurements such as determination of the spectrum, a Ramsey-sequence or atom survival test, for example, single site resolution is not necessary, and hence the exposure time can be chosen considerably shorter (~ 0.2 ms).

3.2. Qubit preparation and manipulation

The general aim is not just to trap single caesium atoms, but to reduce them to an effective two-level system, the so called qubit. Hereby, the simplest quantum mechanical system can be achieved. Having said this, no real atomic system provides a pure two-level structure. Nonetheless, by choosing states carefully regarding experimental preparation capability, intrinsic lifetime and experimental coupling efficiency, the atom can effectively be reduced to the desired system. Generally, a detailed view on engineering single atoms in the presented system can be found in [1]. Figure 3.2 shows the hyperfine structure of both ground states of the employed caesium atom. The energy splitting results from an externally applied quantisation field of about $|B_0| = 3 \text{ G}$. The states of interest are $|F = 4, m_F = 4\rangle$ and $|F = 3, m_F = 3\rangle$ which shall be denoted as $|\uparrow\rangle$ and $|\downarrow\rangle$ in the following, respectively. The σ^+ -polarised optical pumping beam, which is nearly overlapped with the DT1 lattice arm (see figure 3.1), manages to prepare the system in the $|\uparrow\rangle$ state with an efficiency of $> 99\%$. This high value is measured by a spin-dependent detection scheme. Here, a sufficiently strong laser beam couples only the $|F = 4, m_F = 4\rangle$ to an excited state, and literally pushes the corresponding atoms out of the trap [35]. The natural lifetime of the qubit states is extremely long since they only decay via their magnetic dipole moment. However, here the lifetime is limited by the so called longitudinal relaxation time T_1 [40], which is given by spontaneous photon scattering of the atoms, and occurs with a rate of one every 100 ms. This is on a much larger time scale than all experimental qubit operations as well as typical experimental sequences, and can henceforth be neglected. In other words, the effective reduction to a two-level system described by the Hilbert space³ $\mathcal{H}_{\text{qubit}} = \mathbb{C}^2$ is hereby justified.

The two qubit states can be brought into any arbitrary superposition $a|\uparrow\rangle + b|\downarrow\rangle$, $a, b \in \mathbb{C}$. This takes place by coherent coupling via a microwave radiation field of appropriate frequency. The necessary devices are shown in figure 3.2(b). A signal generator is pre-programmed to output a certain frequency (typically $\sim 159.8 \text{ MHz}$) upon a pulse trigger. This signal is mixed with another signal that is fixed in frequency (9.04 GHz) to reach the actual transition frequency. Before the amplification, an attenuator allows to generally switch on/off the signal, or to dynamically shape its amplitude, respectively.

As stated in chapter 2, any superposition of two qubit states can be represented as a point on the so called Bloch sphere with a corresponding three-dimensional Bloch vector \mathbf{u} . By considering the semi-classical interaction picture of a near resonant light field with a two-level system, the dynamics can be sufficiently approximated by the so called *Bloch equations*. When a radiation field of the form $A_{\text{rf}} \cos(\omega_{\text{rf}}t + \phi_{\text{rf}})$ is assumed, where A_{rf} is the amplitude, ω_{rf} the frequency and ϕ_{rf} denotes the phase, then the Bloch equations can be written in the simplified form⁴ [40, 41]

$$\dot{\mathbf{u}} = -\mathbf{\Omega} \times \mathbf{u}, \quad (3.1)$$

where $\mathbf{\Omega} = (\Omega_R \cos \phi_{\text{rf}}, -\Omega_R \sin \phi_{\text{rf}}, \delta)$, with Ω_R being the Rabi-frequency and δ denotes the detuning between the actual transition frequency of both qubit states and ω_{rf} . Assuming a rectangular microwave pulse of duration t_{rf} , the rotation angle θ_{rf} resulting from this action is then defined as the temporal integration of the Rabi-frequency Ω_R over t_{rf} . Experimentally, Ω_R is usually fixed and t_{rf} adjusted as desired. To calibrate the pulse length the qubit population transfer is monitored for an on-resonance light field. For a full population transfer to the other state a rotation angle of $\theta_{\text{rf}} = \pi$ is necessary.

³ $\mathcal{H}_{\text{qubit}} = \mathcal{H}_{\text{qubit}}$

⁴Here, the rotating wave approximation (RWA) has been applied.

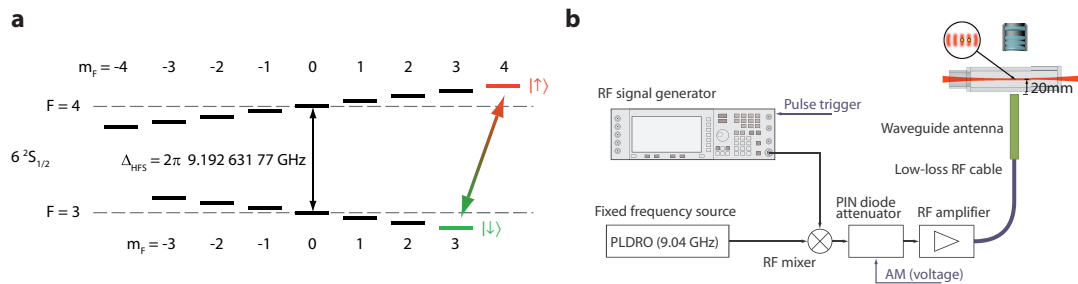


Figure 3.2.: (a) Level scheme showing the split hyperfine substructure of the two caesium ground states. (b) Experimental realisation of a microwave application to perform qubit operations. Adapted from [1].

The corresponding pulse time has a length of $t_\pi \sim 11\mu\text{s}$. Note that in order to find the correct resonance frequency a microwave spectrum is taken. Here, the detuning δ is varied across the resonance, and the resulting sinc-function behaviour of the population probability is recorded. In free space, i.e. without the presence of the dipole trap, the resonance is measured to be $\omega_0^{4\leftrightarrow 3} = 2\pi \times 159.810\text{MHz}(+9.04\text{GHz})$. In principle, this value should be the same for the systems within the trap. However, due to differential light shift effects a state dependent energy shift will occur, thus altering the resonance frequency accordingly. During actual experimental sequences only resonant microwave fields are used.

To be able to express the general action of the microwave pulse in terms of a unitary operator \hat{U} , the Bloch vector picture is transformed into Dirac notation. The corresponding matrix representation yields [1]

$$\hat{U}_{\theta_{\text{rf}}, \phi_{\text{rf}}} = \begin{pmatrix} \cos(\theta_{\text{rf}}/2) & i \sin(\theta_{\text{rf}}/2) e^{i\phi_{\text{rf}}} \\ i \sin(\theta_{\text{rf}}/2) e^{-i\phi_{\text{rf}}} & \cos(\theta_{\text{rf}}/2) \end{pmatrix}. \quad (3.2)$$

This expression can also be compared to the coin operator $\hat{C}_{\text{gen}}(\theta)$ as defined in (2.1). It becomes apparent that the abstract parameters α, β, γ have now a concrete connection to experimental quantities, which can be easily controlled. In fact, by setting the phase to $\phi_{\text{rf}} = \frac{\pi}{2}$ the experimental Hadamard coin is recovered (see section 4.2). Generally, any superposition of both qubit states $|\uparrow\rangle$ and $|\downarrow\rangle$ can be achieved very reliably by carefully tuning the characteristics of the microwave, giving rise to the realisation of the coin-operator.

Once the desired state is prepared and the radiation field switched off, the system precesses in the horizontal plane according to (3.1). However, this behaviour will be influenced by dephasing or decoherence mechanisms. There are two different kinds of such processes: *homogeneous* and *inhomogeneous* dephasing. These are quantified by the transversal relaxation times T_2 and T_2^* , respectively [40, 42]. To probe these decoherence times, a standard Ramsey sequence is performed [43]. Here, the initially prepared $|\uparrow\rangle$ -state is coherently driven into an equal superposition of both spin states by means of a resonant $\frac{\pi}{2}$ -pulse. The system then precesses in the equatorial plane for a duration τ until a second $\frac{\pi}{2}$ -pulse is applied. By scanning the phase of the second pulse the population is sinusoidally varied. Spin-dependent measurements can then record the so-called Ramsey fringe. The contrast drops in size when τ is increased, though. The decoherence time is defined as the value of τ for which the contrast is 50%. Inhomogeneous dephasing can be removed by applying a spin-echo, i.e. a π -pulse, halfway through the sequence. The corresponding benchmark times are $T_2 = 200\mu\text{s}$ and

$T_2^* = 400\mu\text{s}$, respectively. Decoherence processes can be manifold and their impact on the Ramsey fringe contrast is discussed in depth in [42]. Fluctuations of magnetic fields generally cause a temporal changing Zeeman splitting, and hence a slightly changing resonance frequency, which results in dephasing. However, characterisation measurements have shown that fluctuating magnetic fields can be excluded as the main source of limitation here⁵. Another possibility is dephasing due to excitation processes within the trap. This could be caused by jitter which would mainly result from electronic phase noise on the RF-signal controlling the AOMs. In section 3.4.3 it is shown that the negative effects due to this can also be neglected. Clearly, instabilities in all other lattice properties can cause negative effects. However, the main reason for the upper limitations on the coherence times in the optical lattice is believed to be the occurrence of differential light shift effects which can be associated with polarisation impurities. This gives rise to internal- and vibrational state-dependent potentials, which subsequently leads to dephasing, because atoms occupy a range of different radial states. The lattice polarisation impurities can originate from the birefringence of the vacuum window (see above) or a misaligned EOM. Particularly the latter has strict technical limitations to the purity. In fact, reducing the effects to a minimum to guarantee a sufficient coherence time has been experimentally very challenging.

3.3. Spin-dependent transport

Next to the preparation of internal qubit states, it is also very interesting to consider a coherent *spatial* preparation of such. In order to achieve controlled coherent delocalisations of a single atom, which ultimately can lead to interference effects of the system with itself, a spin-dependent transport mechanism is required. Such a scheme has been developed and successfully implemented in the past [1, 44]. The working principle is based on the light polarisation-dependent interaction of each qubit state, and shall be sketched in the following.

For reasons of simplicity, first the fine-structure of caesium is considered. In this picture the qubit states are given by the two possible ground state levels $|J = 1/2, m_J = 1/2\rangle$ and $|J = 1/2, m_J = -1/2\rangle$, and are denoted by $|\uparrow'\rangle$ and $|\downarrow'\rangle$, respectively. The mechanism is explained by recalling the scalar as well as vectorial nature of the light-matter interaction. The former reveals that blue detuned light causes a repulsive potential, and red detuning light an attractive one [39]. The vectorial property then constrains the coupling between states of different magnetic quantum number m_J depending on the polarisation, i.e. $\Delta m_J = +1$ for σ^+ , and $\Delta m_J = -1$ for σ^- -polarised light (see figure 3.3(a)). It shall be assumed that only the two excited states $6^2P_{1/2}$ and $6^2P_{3/2}$ contribute to the energy shift. When putting all this together, it becomes apparent that for a correctly tuned light frequency halfway between those excited states, the contributions of the couplings to the excited $m_J = \pm 1/2$ states cancel out (dashed lines). Therefore, an individual qubit state couples to one, but different polarisation only, and hence transport of systems depending on their internal state is possible by spatially shifting an optical lattice of respective polarisation.

As a matter of fact, tuning the frequency exactly halfway between the two fine states does not quite reveal the desired result. A correct treatment requires the transfer of the intuitive picture above to the actually chosen qubit basis. Hereby, the method of expanding the hyperfine states in terms of the fine structure- as well as the nuclear spin states by using *Clebsch-Gordan coefficients* is used [45]. This basis transformation

⁵The coherence time T_2/T_2^* in free space, i.e. without a lattice, exceeds 0.5/1 ms.

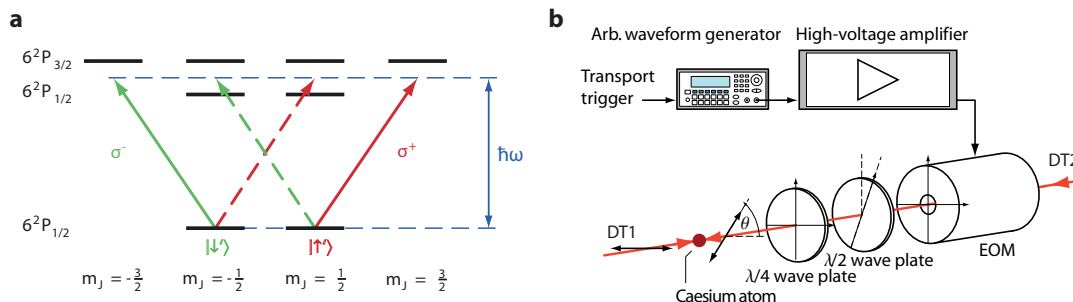


Figure 3.3.: (a) Level scheme showing the fine substructure of the caesium ground state and the first two excited states. (b) experimental implementation of the EOM. Adapted from [1].

then leads to

$$|\uparrow\rangle = |I = 7/2, m_I = 7/2\rangle, \quad (3.3)$$

$$|\downarrow\rangle = \sqrt{\frac{7}{8}} |I = 7/2, m_I = 7/2\rangle \otimes |\downarrow'\rangle - \sqrt{\frac{1}{8}} |I = 7/2, m_I = 7/2\rangle \otimes |\uparrow'\rangle, \quad (3.4)$$

where I represents the nuclear spin of the caesium atom and m_I the corresponding magnetic quantum number. So while the $|\uparrow\rangle$ state purely couples to σ^+ light, the $|\downarrow\rangle$ experiences a slight mixture of σ^- - and σ^+ -polarised light. This impurity has to be taken into account in the experimental realisation (see below). The potential $U_{|\uparrow\rangle}(\lambda)$ for the $|\uparrow\rangle$ state and chosen σ^+ polarisation, respectively, can be analytically determined as a function of the wavelength λ [44]. In order to guarantee pure coupling of this spin state to the chosen polarisation, the potential needs to drop to zero, i.e. $U_{|\uparrow\rangle}(\lambda) = 0$. Calculations yield the magic wavelength of $\lambda_{|\uparrow\rangle} = 865.9\text{nm}$.

Imagining a lattice composed of linearly polarised light as employed in the experiment, the intensity I can be decomposed into the sum of two individual lattices of σ^+ - and σ^- -polarisation, respectively, i.e.

$$I(\mathbf{r}) = I_{\sigma^+}(\mathbf{r}) + I_{\sigma^-}(\mathbf{r}). \quad (3.5)$$

If the angle θ between the linear polarisations of both lattice arms is zero, both lattices coincide and no spin-dependent effect is visible. Spatial rotation of one of the polarisations brings the system into the so called lin- θ -lin configuration. It can be shown that this angle induces a relative shift of both lattices. The spatial intensity distribution is now given by

$$I_{\sigma^\pm}(\mathbf{r}, \theta) = A^2(\mathbf{r}) \cos^2(f(\mathbf{r}) \mp \theta/2). \quad (3.6)$$

So changing the angle θ will translate both spin-dependent lattices in opposite directions, hereby realising the spin-dependent transport. Experimentally, the rotation of θ is achieved by an electro-optic modulator (350-150 by Conoptics), which is placed in the beam path of DT2 (see figure 3.3(b)). Applying a voltage to this device in combination with a $\lambda/4$ -plate between EOM and vacuum chamber rotates θ as required. To make the transport sufficient, the relative shift needs to be at least $\lambda/2$, i.e. a rotation of π , such that the lattices coincide again. This shall be referred to as a single transport step in the following. However, the installed EOM model does not allow this amount of rotation at room temperature⁶. Therefore, one of the EOM's end caps is connected to

⁶Note that this was not the case in the previous single-arm configuration, where due to the double pass only half of the rotation needed to be performed.

a peltier element and a CPU water cooling system to reduce the temperature to 17°C . The temperature is stabilised by a standard PID controller. In order to minimise temperature gradients the EOM is additionally covered in foam rubber. For translating one lattice site, the EOM needs to be ramped up to about $V_{\lambda/2} = 700\text{V}$. In fact, one step is the most the EOM can do. The subsequent decrease of the applied voltage causes the lattices to shift in opposite directions than before. Hence, in order to keep the system's transport direction a spin flip is required after a single transport step. Furthermore, the ramping time can not be arbitrarily chosen. The discussed intrinsic impurity of the coupling results in a wobbling of the respective trap during the transport. This causes excitation of higher vibrational states, and destroys coherences of the system accordingly. This effect, however, can be compensated if the transport is done in a certain time. This *magic transport time* depends in detail on the characteristics of the trap, but is around $24\mu\text{s}$ for a typically employed trap depth of $100\mu\text{K}$. Generally, the EOM offers a maximum polarisation purity of 10^{-4} , which limits the coherence time as stated above. This value depends delicately on the EOM's alignment.

3.4. Acceleration of trapped atoms in an optical lattice

3.4.1. Principle of operation

While the spin-dependent transport scheme is able to shift atom systems depending on their internal state, it is unable to move the system globally. For this the entire lattice needs to be translated. This can be achieved by detuning the two lattice arms relatively to each other. An immediate understanding is delivered by the familiar picture of a Doppler shift: Imagining an atom moving at a velocity of

$$v = \frac{\lambda}{2} \delta\nu \quad (3.7)$$

in the presence of two counter-propagating light fields at frequency ν_1 and $\nu_2 = \nu_1 + \delta\nu$, respectively. In the moving frame of the system both frequencies are shifted by an equal, but opposite amount such that the two frequencies coincide. The result is a static standing wave potential in the moving frame of the atom. In the static or laboratory frame, however, this potential, and likewise a trapped atom, moves at speed (3.7) along the lattice axis. This picture holds firmly in the case of two Gaussian laser beams as used in the presented setup [35].

Assuming that the frequency detuning has an intrinsic time dependence, i.e. $\delta\nu(t)$, the trapped atoms experience an acceleration according to

$$a = \frac{dv}{dt} = \frac{\lambda}{2} \frac{d(\delta\nu)}{dt}. \quad (3.8)$$

So by ramping the frequency of one of the lattice arms (or both simultaneously in opposite directions) leads to corresponding acceleration and deceleration processes of the system. However, it is necessary that the ramping takes place in a phase continuous fashion to ensure that no atoms get literally kicked out of the trap. As long as the acceleration stays below a certain threshold the atoms will remain trapped in one potential minimum and will follow the dynamics of the lattice. The maximum acceleration a_{cr} is approximated by the value for which the potential generated by the acceleration over a distance $\lambda/4$, i.e. $U_{\text{acc}} = M a \lambda/4$ exceeds the trapping potential U_0 , where M is the mass of a single caesium atom. For a typical value of $U_0 = k_B \times 100\mu\text{K}$

this values can be calculated to be $a_{\text{cr}} \approx 2.9 \cdot 10^3 g$, with g being the standard acceleration due to free fall. Gaining control over the precise adjustment of the lattice arms' frequencies gives rise to an experimental control of movement and acceleration of the optical lattice system. This also allows to deliver atoms deterministically to positions of interest, hereby creating an *optical atom conveyor belt*, whose functionality has been shown before [35, 46, 47]. More importantly though, the acceleration can be used to test the quantum transport properties of a quantum walk as motivated in chapter 2. For that purpose, a home-built device employing a direct digital synthesizers has been constructed, which is able to control and detune both frequencies relative to each other.

3.4.2. The Direct Digital Synthesizer

Direct digital synthesizers (DDS) are nowadays a standard tool for creating analogue signals depending on digital inputs. Their high frequency precision and low phase-noise features up to the GHz-range make them very suitable for being RF-sources. Here, a dual output DDS has been installed. Unlike the previously used voltage controlled oscillator (VCO), the DDS allows precise tuning of the signals' frequencies which operate the acousto-optic modulators (see figure 3.4). Thus, it allows to dynamically control the frequencies of the laser arms in the MHz regime. Consequently, the DDS offers the possibility to move and accelerate the optical lattice at will, as discussed above.

The AD9954 DDS Chip

The offer of DDS chips are manifold and they vary with respect to resolution, maximum output frequency and performance qualities. Here, the DDS chip AD9954 from Analog Devices shall be introduced. This chip was utilised and ultimately implemented in the setup in its evaluation board version. It offers two synchronised AD9954 chips, allowing for a double frequency output.

Working principle The AD9954 generates a sinusoidal waveform up to 160 MHz by means of a 14-bit digital-to-analog converter (DAC) with an output power of about -5dB. All information about the used DDS chip as well as associated schematics can be found in [48]. Generally, the evaluation board takes digital input signals and converts them with the aid of internal logic circuits into a function which can be represented as a digital "phase wheel". An external reference clock discretely takes the system around this wheel according to the clock's frequency. Every point on the phase wheel represents one sampling point of the sinusoidal output signal. The latter is finally achieved by the mentioned DAC⁷. The AD9954 allows for a clock frequency of up to 400 MHz. The frequency precision at this value is 0.1 Hz. Although the device is equipped with an internal clock multiplier, in order to keep residual phase stability at a maximum a 400 MHz source is used to support the DDS board. The clock employed is a Hewlett Packard 8640B signal generator, which is phase stabilised by an internal microwave cavity [50]. A high quality reference is needed for the DDS, since noise properties would directly propagate into corresponding characteristics of the output signal. The clock's input power is specified by the board to be around 0.0 dBm, i.e. 220 mV_{rms}.

The communication with the DDS board takes places via a serial interface. Tuning words describing the information, e.g. for frequency or phase (32-bit or 14-bit), are transmitted to the chip where they address chosen registers. The binary form of any

⁷Detailed information about the working principles of a DDS in general can be found in [49].

frequency tuning word, for example, is given by

$$B_F = F \times \frac{2^N}{\text{clock}}, \quad (3.9)$$

where F is the frequency quantity in physical units of Hz, N is the fixed binary length of the tuning word and clock denotes the frequency of the external reference. Internal logic then accesses respective registers, and uses their stored information to shape the output properties of the AD9954. As a matter of fact, the device's information processing speed is fundamentally limited by the duration of four cycles of the reference clock, i.e. $t_{\text{fund}} = 4/(400 \times 10^6) \text{ s} = 10 \text{ ns}$. In the default running mode of the chip the frequency output is static. By exploiting intrinsic synchronisation functions of the evaluation board, the two frequency output channels (Ch1, Ch2) can be phase locked to each other (for an analysis of the residual phase noise see section 3.4.3). Usually the DDS is operated at simultaneously emitted output frequencies of 80 MHz. Higher harmonics and other emitted higher frequencies are suppressed with a built-in low-pass filter by at least 65 dB.

Frequency ramping One of the main reasons to have chosen the AD9954 among the offered DDS chips is its ability to drive frequency ramps. There are two main ramp operation modes: The *linear sweep* mode and the *RAM* mode. The linear sweep mode only needs information about the start- and end-frequency as well as the temporal frequency gradient. Upon the software activation of this mode and an additional trigger, the DDS automatically changes discretely the frequency output until the end-frequency is reached. The RAM mode on the other hand is based on 1024 32-bit frequency addresses to which information needs to be written. When activating this mode the DDS jumps from one frequency address to the next after a pre-defined time-step. Whereas the sweep mode only allows for linear ramps, the RAM mode offers the opportunity to realise any kind of customized ramp-shapes. However, the huge drawback of the latter is the duration of a potential rewriting process, which, assuming that all 1024 addresses get new information, lasts $t_{\text{RAM}} = 1024 \times 32 \times t_{\text{fund}} \approx 0.33 \text{ ms}$. Despite the differences, both modes allow for bi-directional ramping of the frequency, which in turn offers acceleration and movement of the optical lattice in both directions along the lattice axis. Additionally, both modes crucially fulfil the requirement of phase continuous ramping. Due to the mentioned time delay of the RAM mode, though, all frequency ramps presented in this thesis are based on the linear sweep mode. The general method is to fix the frequency of one of the channel outputs (Ch2) and to simultaneously use the linear sweep mode on the other chip (Ch1).

DDS box

In order to make the DDS technology implementable, the sole evaluation board is not sufficient. Hence, a box has been constructed that contains all necessary components to handle the DDS board and its outputs in a convenient way. Figure 3.4 shows the layout of this DDS box. The casing (Feltron 2008-0705) was chosen such that all components could fit into the box in one plane. Most importantly, the communication to the DDS chips via a serial connection is obtained by using a microcontroller (mbed NXP LPC1768) that can be addressed by a computer via a standard USB-port. The power connection is a typical $\pm 15\text{V}$ input, which is then regulated down to 5V, 3.3V and 1.8V by voltage regulators, respectively. While the last two voltages are needed to supply the evaluation board, 5V are used to internally supply the mbed microcontroller. The

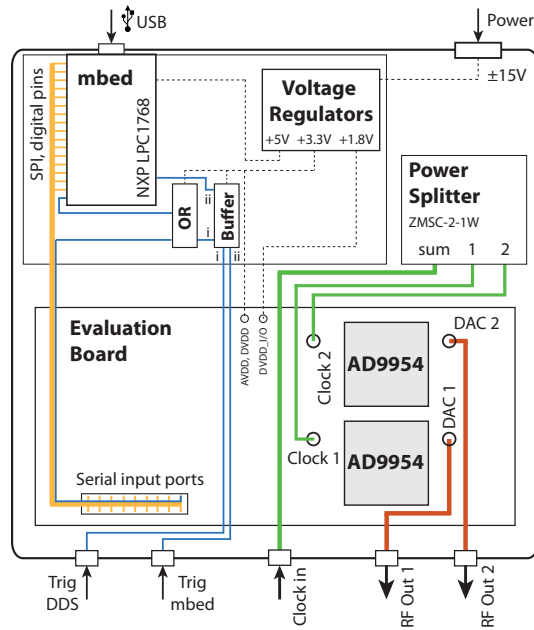


Figure 3.4.: Schematics of the home-built DDS box. The core of this box is the AD9954 evaluation board and an mbed microcontroller, allowing to control the desired RF-output by means of a USB-connection. Different colors indicate different signals and their functions.

reference clock signal is equally split inside the box by a power splitter (Minicircuits ZMSC-2-1W), since both DDS chips require an individual clock input. Because the power splitter causes losses in the clock signal, the total input power of the reference clock needs to be adjusted to the required 0.0 dBm at the evaluation board. This leads to a necessary total input power of $P_{\text{clock,total}} \approx 1 V_{\text{rms}} = 4 \text{ dBm}$. The initial signal is fed to the box by a standard BNC connector. Furthermore, the mbed microcontroller communicates with the DDS evaluation board via its serial peripheral interface bus (SPI). All tuning words are written by this means. Additional digital pins are used for triggering or specific addressing purposes. A full picture of the mbed-DDS connection can be found in Appendix A. Further, see [48] for a detailed description of each pin. The microcontroller’s software code can be easily programmed by using the associated online ”C++” compiler. The desired file is then transferred via the USB connection.

In order to facilitate a high timing-resolution of frequency ramps, the box does not only rely on the USB connection to a computer, but can be triggered by an extra TTL signal. The box offers two options: Either the microcontroller can be triggered or the respective pulse reaches the DDS board directly. In both cases the 5V input trigger signal is reduced to the working voltage of 3.3V by a buffer (MC14050BCP). Depending on the trigger’s nature, this signal is fed to the mbed (microcontroller trigger) or to an OR-gate (HEF4071), where it is combined with a corresponding signal from the microcontroller. The output of the buffer then serves as the DDS trigger. Buffer and OR-gate have a typical delay time of 100ns and 55ns, and therefore cause a trigger delay of 100ns and 155ns of the mbed- and DDS trigger, respectively. However, these delay times can be neglected as they are much smaller than the time resolution of the experiment control ($\sim 2\mu\text{s}$). Finally, the DDS output channels are connected to SMA-connection sockets.

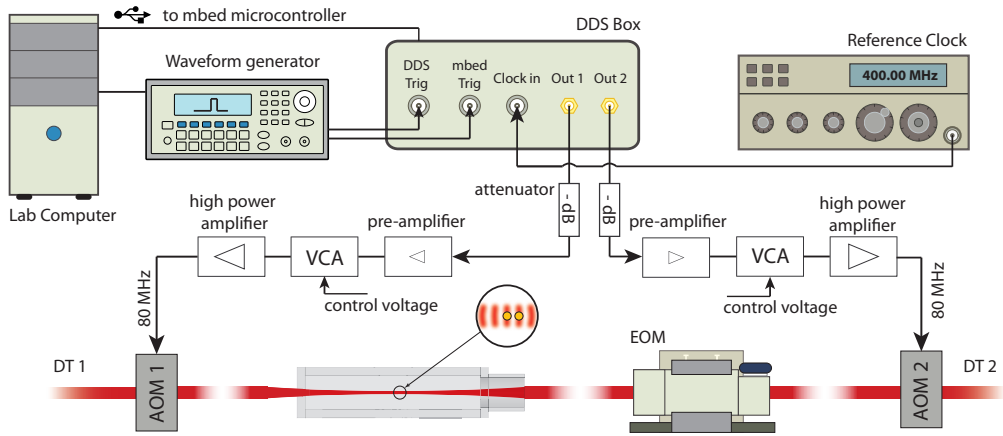


Figure 3.5.: Schematics of the AOM-circuit with the implemented DDS-box.

Implementation into the current setup

The DDS box was implemented in the current setup as shown in figure 3.5. The 400 MHz reference source is connected to the box via its designated port as described above. Whereas the communication connection from computer to DDS box is direct, the box receives the trigger pulses from a waveform generator which can be programmed prior to the experimental sequence. By this it is ensured that the trigger is sent with the desired timing. The two phase-locked outputs of the new RF-source are embedded in the present setup by means of a combination of attenuators and a pre-amplifier (Minicircuits ZHL-03-5WF), which replace the previously used arrangement of VCO and power splitter. The final signal is then sent to a voltage controlled attenuator (VCA - Minicircuits ZX73-2500-S+). Here, the amplitude of the signal is modified depending on a control voltage. This voltage is either applied in a static way, or by means of a servo controller. The latter allows to vary the voltage according to some error signal, hereby intensity stabilising the lattice beams. The outputs of the VCAs are finally guided to a high power amplifier that increase the signals' power by 30dB up to 1W. This is the maximally allowed power input of the AOMs, which complete the line of devices. The initially introduced attenuators and the pre-amplifier are chosen in such a way that when the VCA transmits the full power, the signal never exceeds this figure of 1W.

In order to get the desired output signals, and particularly to drive precise frequency ramps, the communication of the DDS box with the controlling computer is key. Generally, global parameters like the clock frequency or the default static output frequencies of both channels as well as the type of frequency ramp mode used (see section 3.4.2) are intrinsically embedded in the programmed source code. The compiled programme is run from the mbed's flash memory, and causes an output of two 80 MHz signals as soon as the device is switched on, for example. This, however, is not sufficient to change parameters ad hoc. For that purpose a separate serial connection is emulated allowing to communicate live with the mbed via the USB line. Parameters for detuning one of the frequencies, and thereby inducing dynamics to the lattice can then be changed via an interface⁸ on the run. The interface is able to send and receive information to and from the mbed, respectively. The general working principle for frequency ramps is that the

⁸The interface is formed by the online available software "HTerm", which is a terminal programme featuring serial ports.

mbed waits until all necessary parameters are filled, before going into a loop where it can receive trigger signals. Upon sending such a trigger to the mbed the programmed ramp is activated. This implements the idea of preventing possible time delays by transferring the main information to the microcontroller and transforming all internal parameters into tuning words before the actual sequence. Clearly, the exact form and structure of the code is adjusted to the respective experimental circumstances. A more detailed example of a used programme code is given in section 5.2.1.

3.4.3. Characterisation and performance of the DDS box

Heating atoms due to phase noise

Despite the fact that the two AD9954 DDS-chips' outputs are phase stabilised to each other, there is a remaining and inevitable relative phase noise due to small imperfections of the respective signal paths. Since this residual phase noise translates directly into associated properties of the standing wave potential formed by the two light waves passing through the AOMs, a quantitative analysis of the noise is necessary. Common noise of the signals, on the other hand, is not reflected in the optical lattice.

The phase noise of two signals with respect to each other can be measured by mixing them. The disturbance becomes then visible as amplitude noise of the mixed signal. In general, multiplication of two waves generates a superposition of two new waves: one oscillating at the frequency difference of the initial two and the other one at their sum. Applying low-pass filtering processes to this signal leaves only the low-frequency component which can be described by

$$V_{\Delta f}(t) = V_0 \cos [2\pi \Delta f t + \Delta\phi_0 + \Delta\phi(t)] , \quad (3.10)$$

where V_0 describes the amplitude of the signal, $\Delta\phi_0$ is the relative phase difference between the two mixed signals and $\Delta\phi(t)$ represents the time-dependent residual phase noise. When tuning both frequencies to the same value, the remaining signal has dominantly a DC nature according to $\Delta\phi_0$, but fluctuates due to the phase noise. In addition, by setting the relative phase to exactly 90° the cosine function in (3.10) can be linearly approximated, i.e. $V_{\Delta f}(t) \approx V_0 \Delta\phi(t)$. Determining $V_{\Delta f}(t)$ plus finding V_0 independently gives the possibility for a direct measurement of the residual phase noise which is commonly characterised in its root mean square value (rms):

$$\Delta\phi_{\text{rms}} = \frac{V_{\Delta f, \text{rms}}}{V_0} . \quad (3.11)$$

Here, the two 80 MHz DDS output signals were mixed by a phase detector (minicircuit RPD-1). The relative phase difference could be conveniently adjusted exploiting the phase offset features of the DDS board. The phase detector's output was then amplified by a low noise amplifier (Stanford Research Systems SR560) in order to better distinguish the actual noise signal from intrinsic noise of the measurement device. After an applied low-pass filter, a spectrum analyser (Agilent Technologies N9010) was able to detect the frequency spectrum of the phase noise in units of volts. In order to convert this signal into radians, V_0 was measured with an oscilloscope by deliberately detuning one of the two channels by 1kHz. Paying attention to necessary calibration factors the phase noise spectrum $\Delta\phi(\nu)$ could be finally found in its desired units. An important quantity that can be deduced from this is the one-sided noise spectral density function $S_\phi(\nu)$, where $S_\phi(\nu) = \Delta\phi_{\text{rms}}^2(\nu)$ [51]. For this expression it holds that

$$\Delta\phi_{\text{rms}}^2 = \int_0^\infty S_\phi(\nu) d\nu , \quad (3.12)$$

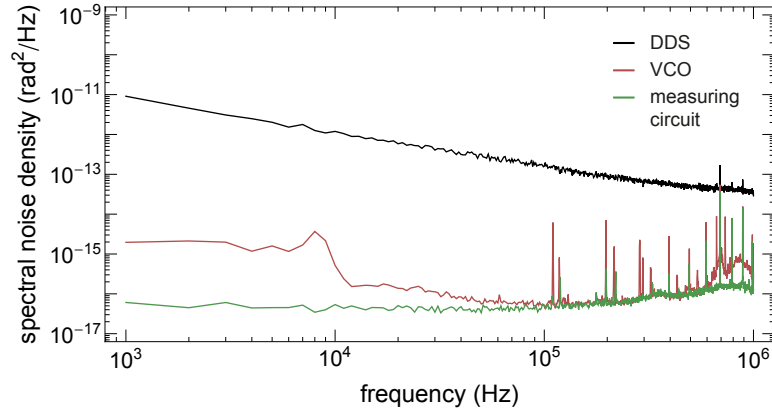


Figure 3.6.: Measured spectral noise density as a function of frequency. The $S_\phi(\nu)$ of mixed DDS-box output signals (black) is compared to the previously employed single VCO source (red). The green curve represents measured noise without any input signal. The DDS phase noise follows a $1/f$ -relation.

owing to the additive nature of the power quantity. $S_\phi(\nu)$ is plotted in figure 3.6, and by numerical integration the DDS' rms-noise value was calculated according to (3.12) to be $\Delta\phi_{\text{rms}} \approx 10^{-4}$ rad over a range of $[0, 1\text{MHz}]$. The noise almost shows a pure $1/f$ -dependence. For comparison also the noise from the previously employed VCO circuit is plotted. Since in this case the signal is created by one source only, the phase noise can only result from the used signal splitting device. The overall VCO noise is therefore strongly suppressed compared to the DDS noise.

To determine the impact of the measured noise on the optical lattice, it is essential to realise that the phase of the trap changes exactly in the same way as the electronic signals. So a fluctuating electronic phase is equivalent to a spatially shaking standing wave, where the exact correspondence can be deduced from

$$\frac{\Delta\phi(t)}{2\pi} = \frac{\Delta x(t)}{(\lambda/2)} \quad \rightarrow \quad \Delta x(t) = \frac{\Delta\phi(t)}{2k}, \quad (3.13)$$

with k being the size of the lattice' wavevector. The small position fluctuation give rise to a force in the co-moving frame according to $F = M\Delta\ddot{x}(t)$. Assuming that the trapping regions can be approximated by a one-dimensional harmonic oscillator, the resulting Hamiltonian yields⁹

$$\hat{H} = \underbrace{\frac{\hat{p}^2}{2M} + \frac{1}{2}M\omega_{\text{ax}}^2\hat{x}^2}_{\hat{H}_0} - \underbrace{M\Delta\ddot{x}(t)\hat{x}}_{\hat{H}_1(t)}, \quad (3.14)$$

with ω_{ax} being the axial trap frequency and M is the mass of a caesium atom. As long as the fluctuations are small, i.e. $E_1 \ll E_0$ (energies of the associated Hamiltonian), first order perturbation theory can be used to calculate the excitation rate of the system to a different eigenstate of the harmonic trap [52]. The interaction picture yields for the excitation rate

$$\Gamma_{m \leftarrow n} = \frac{1}{T} \left| \frac{-i}{\hbar} \int_0^T \langle m | H_1(t) | n \rangle e^{i\omega_{\text{ax}}t} \right|^2, \quad (3.15)$$

⁹Note that only shaking along the lattice axis is assumed. Hence, the radial motion is neglected and the problem becomes one-dimensional.

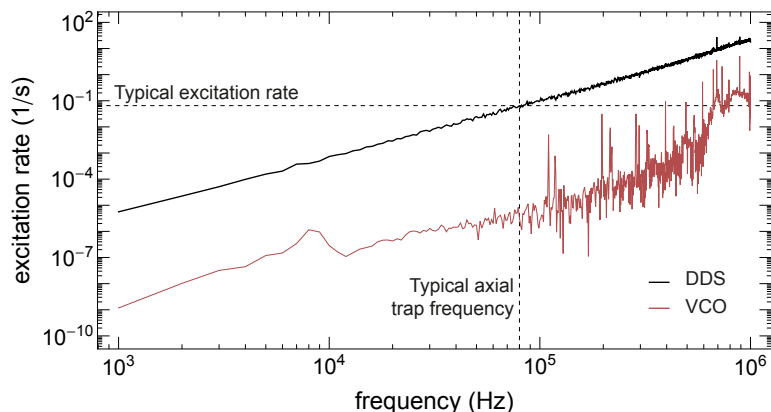


Figure 3.7.: Expected axial excitation rate due to measured residual phase noise of the two DDS output channels (black). For a typical trap frequency of 80kHz the rate is about 0.1s^{-1} . The excitation rate caused by the previously installed VCO circuit is at this frequency about 5 orders of magnitude lower (red).

where m and n represent different states of the harmonic oscillator. When computing this expression the occurring autocorrelation function of $\Delta x(t)$ can be expressed in terms of the noise spectral density (3.12) via the so-called *Wiener-Khinchin* theorem [51]

$$S_x(\nu) = \int_{-\infty}^{\infty} \langle \Delta x(t) \Delta x(t + \tau) \rangle e^{-2\pi i \nu \tau} d\tau. \quad (3.16)$$

Assuming that the atoms are sufficiently cooled such that they initially occupy the ground state only, the excitation rate to the next higher level can be calculated to be [53, 54]

$$\Gamma_{1 \leftarrow 0} = \frac{2\pi^3}{\hbar} M \nu_{\text{ax}}^3 S_x(\nu). \quad (3.17)$$

By converting the measured $S_\phi(\nu)$ into $S_x(\nu)$ by means of (3.13), the excitation rate can be plotted as a function of the axial trap frequency ν_{ax} (see figure 3.7). It can be seen from this graph that an excitation rate of about 0.1s^{-1} can be expected for a typically employed trap frequency of $\nu_{\text{ax}} \approx 80\text{kHz}$. As this is on a time scale that is much longer than a scattering event for example (10s^{-1}), it can be deduced that excitation processes and hence also the atom's lifetime in the optical lattice are not limited by electronic phase noise. Prove of the latter statement delivers the measurement of lifetimes in a lattice controlled by the DDS or a VCO, respectively. Without the presence of cooling molasses the survival is about 5s in both cases. As the residual phase noise of the DDS exceeds that of the VCO by many orders of magnitude, both outcomes should be clearly distinguishable if the phase noise was a limiting factor. Nonetheless, a correct prediction of an atom's lifetime limited by this heating mechanism is not possible with the used method since the harmonic approximation does not hold for higher excited states. Ultimately, the length of a typical experimental sequence is $\sim 1\text{ms}$, and thus the effect of excitation due to electronic phase noise can be neglected. Note that heating processes might occur due to other fluctuation behaviour such as intensity or pointing instabilities, for example. The analysis of those, however, is beyond the scope of this thesis.

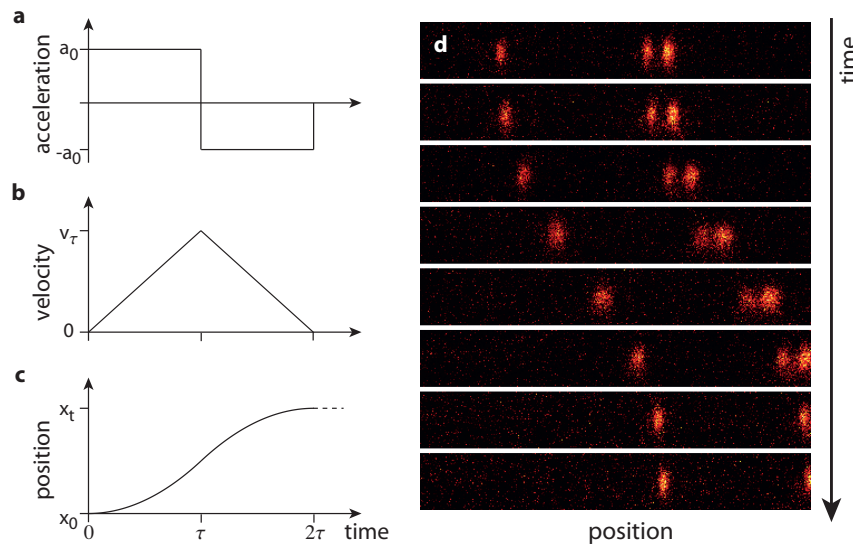


Figure 3.8.: Demonstration of a triangular frequency ramp sequence. In (a)-(c) the behaviour of the acceleration, velocity and position are presented according to (3.8) and (3.7). Live images of atoms experiencing such a sequence are shown in (d). The total sequence length was $2\tau = 20$ s with a detuning gradient of 1 Hz/s. It can be seen how the imaging time of 1 s smears out moving atoms halfway through the sequence.

Accelerating trapped atoms

The effect of an accelerated lattice shall now be explicitly demonstrated by imaging trapped atoms. As explained in section 3.4.2, arbitrary shapes of frequency ramps are technically possible, but due to timing issues solely linear ramps, i.e. constant accelerations are employed. Generally, idle times between ramping steps can be introduced, or consecutive applications of ramps in the same direction are possible. The only requirement is that the system needs to be brought back to a static case in the end, in order to allow for single-site detection imaging. The simplest of such sequences is where the detuning follows the shape of a triangle, i.e. is composed of two consecutive equal, but opposite ramps. To give a proof of principle, this triangular detuning ramp is sufficient. The corresponding behaviour of the experienced acceleration, velocity and position of an atom according to (3.7) and (3.8) can be seen in figure 3.8(a)-(c). In order to make the dynamics of the atoms visible, a low detuning gradient of 1 Hz/s was realised over a deliberately chosen long single ramp time of $\tau = 10$ s. Atoms were imaged live during this ramp sequence. Note that this was possible since the imaging time (1 s) was short compared to the entire sequence length of 2τ . Figure 3.8(d) shows images of the moving atoms, and nicely reveals the quadratic path that is followed by them. The end-position agrees fully with the theoretically expected one.

Here, meeting theoretical predictions means a deterministic delivery of atoms with a precision exceeding the single-site resolution limit. This performance is to be independent of the ramp time and acceleration strength as long as the latter is chosen sufficiently below the critical acceleration a_{cr} (see section 3.4.1). Potential error sources preventing this precision might be found in software flaws caused by rounding problems or temporal trigger instabilities, for example. However, the efficiency could be measured to be $> 98\%$ for performed transports of moderate accelerations ($< 100g$). This transport efficiency will significantly drop when approaching a_{cr} , though. At this point atoms start to hop between lattice sites during the ramp or might even get lost.

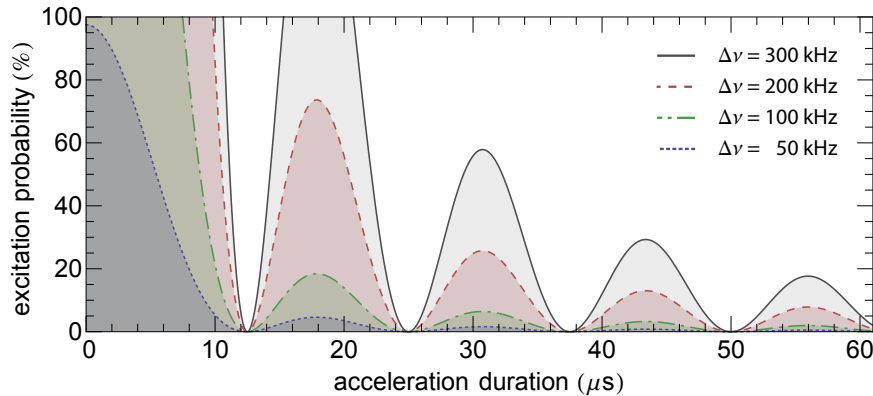


Figure 3.9.: Theoretically predicted excitation probabilities of an atom trapped to the ground state of a harmonic oscillator experiencing a static force. The probabilities are plotted as a function of the ramp length τ of a linear frequency ramp, and are given for different values of the final detuning. An optimal transport time for a trap frequency of $\omega_{\text{ax}} = 2\pi \times 80$ kHz is given by $\sim 12.5\mu\text{s}$.

Assuming that one will always stay well below a_{cr} , the system might still be negatively influenced. So far the internal states of the lattice have been neglected. However, excitation processes might occur upon acceleration, which destroy coherent evolutions. The theoretical treatment of this excitation is completely analogous to section 3.4.3. Here, however, the force is not caused by an oscillating phase noise, but rather by a constant acceleration over a certain single ramp duration τ , meaning that the perturbing Hamiltonian \hat{H}_1 in (3.14) can de facto be seen as time-independent over the interval $[0, \tau]$, i.e.

$$\hat{H} = \frac{\hat{p}^2}{2M} + \frac{1}{2}M\omega_{\text{ax}}^2\hat{x}^2 - Ma_0\Pi(t_\tau)\hat{x}, \quad (3.18)$$

where a_0 is the constant acceleration strength, $\Pi(t)$ denotes the Heaviside *pi*-function¹⁰ and the time t_τ is here given in units of τ . Using again the form of (3.15), the corresponding excitation probability can be computed to be

$$P_{0 \rightarrow 1}^{\text{acc}} = \frac{2Ma_0^2}{\hbar\omega_{\text{ax}}^3} \sin^2\left(\frac{\omega_{\text{ax}}^2\tau}{2}\right). \quad (3.19)$$

Usually, the acceleration itself is not the parameter of interest, but rather one that couples acceleration a_0 and ramp time τ . Here, this parameter shall be the maximal detuning $\Delta\nu$ at the end of a single ramp, i.e. at time τ . When employing a linear ramp, the acceleration can be described as $a_0 = \lambda\Delta\nu/(2\tau)$ according to (3.8). Evidently, by decreasing τ the acceleration needs to become larger to guarantee the same final detuning, and vice versa. By substituting the expression into (3.19), it can be seen that this inverse proportionality causes the excitation probability to asymptotically decay as $1/\tau^2$. However, the oscillatory behaviour of the \sin^2 -function also allows to find local excitation minima for a certain acceleration at short ramp durations. Figure 3.9 shows the excitation probability of different detunings $\Delta\nu$ as a function of τ . Although the $1/\tau^2$ dependence varies strongly, the local minima all coincide. An optimal transport time, which minimises duration as well as excitation probability, is given by $\sim 12.5\mu\text{s}$ for a typically used trap frequency of $\omega_{\text{ax}} = 2\pi \times 80$ kHz. Below this ramp time

¹⁰ $\Pi(t) = \begin{cases} 1 & \text{for } 0 \leq t \leq 1 \\ 0 & \text{else} \end{cases}$

the excitation probability approaches a considerable value quite rapidly. In fact, the perturbation theory approach breaks down in cases where the excitation probability significantly exceeds one, as it is the case for very short acceleration times. Despite the fact that an excitation minimum can always be found for longer ramp times, for a final detuning of about 10 kHz (and below) the excitation probability is close to zero, and therefore negligible for any value of τ above the minimal time of $\sim 12.5\mu\text{s}$.

Note that the presented discussion is based on the assumption that the ramp is purely continuous. However, since the DDS switches frequencies discretely during the ramp, this is strictly speaking not the case. The typical time¹¹ after which the frequency is changed by a pre-defined size is 100ns. This is on a much smaller time scale than what is given by the trap frequencies. It is therefore presumed that the atoms do indeed experience a continuous ramp, and hence that the discussion above firmly holds.

¹¹The smallest possible value is 10ns. However, this would strongly constrain the range of possible acceleration strengths a_0 due to the discrete nature of the DDS.

Chapter 4.

Quantum walks with individual atoms

After having introduced all necessary experimental tools, the realisation of quantum walks with single Caesium atoms shall be presented in this chapter. Such quantum walks have already been achieved previously [1]. However, the results presented here show qualitative as well as quantitative improvement. This chapter leads through the applied experimental sequence and gives a suggestion for an applicable decoherence model, before finally demonstrating the measured results.

4.1. The experimental walk operator

An ideal quantum walk is described by the walk operator (2.3). As described in section 3.2 the state preparation of the atom and the microwave coupling between the $|3, 3\rangle$ and $|4, 4\rangle$ states is so efficient that the coin operation can in principle be experimentally achieved to a very high reliability. However, due to the alternating shift directions of the two spin-dependent lattices, the realisation of the shift operator cannot occur as in the ideal theoretical picture. The different actions rather describe two shift operators that translate into opposite directions. Extending the definition of (2.2), these are given by

$$\hat{S}_{\rightleftharpoons} = \begin{cases} |n, \uparrow\rangle \rightarrow |n+1, \uparrow\rangle \\ |n, \downarrow\rangle \rightarrow |n-1, \downarrow\rangle \end{cases} \quad \text{and} \quad \hat{S}_{\leftrightharpoons} = \begin{cases} |n, \uparrow\rangle \rightarrow |n-1, \uparrow\rangle \\ |n, \downarrow\rangle \rightarrow |n+1, \downarrow\rangle \end{cases} . \quad (4.1)$$

Both shift operators always appear in pairs. Consequently, this leads to an extension of \hat{W} to form the experimental walk operator

$$\hat{W}_{\text{exp}} = \left[\hat{S}_{\leftrightharpoons} \cdot (\hat{\mathbb{1}}_{\text{space}} \otimes \hat{C}) \cdot \hat{S}_{\rightleftharpoons} \cdot (\hat{\mathbb{1}}_{\text{space}} \otimes \hat{C}) \right] . \quad (4.2)$$

As before, the full quantum walk is obtained by consecutively applying \hat{W}_{exp} to an initially prepared system $|\psi_0\rangle$. The state after $N' = 2N$ steps reads

$$|\psi_N\rangle = \hat{W}_{\text{exp}}^{N'} |\psi_0\rangle . \quad (4.3)$$

It can be shown that \hat{W}_{exp} reveals the same dynamics as the textbook operator \hat{W} . However, the probability distribution is found to be mirror-inverted. This can be fundamentally explained by expressing the walk again in its Fourier picture. Proceeding analogously to section 2.2, by fixing \hat{C} to the form of a balanced experimental Hadamard coin \hat{C}_{EH} , the k -space representation reads

$$\hat{W}_{\text{exp},k}^{\text{spin}} = \begin{pmatrix} e^{ik} & 0 \\ 0 & e^{-ik} \end{pmatrix} \cdot \frac{1}{\sqrt{2}} \begin{pmatrix} 1 & -1 \\ 1 & 1 \end{pmatrix} \cdot \begin{pmatrix} e^{-ik} & 0 \\ 0 & e^{ik} \end{pmatrix} \cdot \frac{1}{\sqrt{2}} \begin{pmatrix} 1 & -1 \\ 1 & 1 \end{pmatrix} . \quad (4.4)$$

Evidently, this has the same form as \hat{W}_k^{spin} applied twice, with the only difference that the last acting shift operator is rotated by π in matrix representation. It can further be shown that for the specific coin angle of $\theta = \pi/2$

$$\hat{W}_{\text{exp},k}^{\text{spin}} = -\hat{R}_\pi \left(\hat{W}_k^{\text{spin}} \right)^2 \hat{R}_\pi^{-1}, \quad (4.5)$$

where $\hat{R}_\pi = \begin{pmatrix} 0 & -1 \\ 1 & 0 \end{pmatrix}$. So the rotation of the last shift operator swaps the eigenvalues of the ideal walk operator. As a result the mapping of a given state onto the bands as discussed in section 2.2 is reversed. This leads to flipping the sign of the associated group velocity, hence giving rise to a mirror-inverted probability distribution. Note that this is generally true for all initial states $|\psi_0\rangle$, but might not be observed due to intrinsic mirror symmetry such as in the $|s_0\rangle = \frac{1}{\sqrt{2}}(|\uparrow\rangle + i|\downarrow\rangle)$ spin configuration.

4.2. Experimental procedure

The successful realisation of a quantum walk with the presented experimental setup is composed of two parts. First, after optimising all experimental parameters, the trapped atoms need to be prepared and characterised. Only then the actual experimental quantum walk sequence can be run in a second step. Table 4.1 lists in a chronological fashion the steps to be undertaken in order to guarantee experimental success.

At the very beginning the survival of atoms in the trap is measured. Here, the trap depth is varied just as in the later performed sequence from initially 0.4mK (trapping, cooling, imaging) over 0.1 mK (sequence) back to 0.4 mK (imaging). The survival probability should be close to unity, but might drop a little due to atom miscounting or rare cases of losses. The allowed tolerance figure is just a few percent, though. The preparation of the atom in the $|4, 4\rangle$ ground state is done by optical pumping. A survival measurement after the application of a push-out beam is used to determine the efficiency of this state preparation. Ideally, all atoms should be removed from the trap after this sequence. These two test measurements are the basis of all experimental sequences. Then, one can embark on characterising the atoms' properties with respect to the trap, the qubit manipulation and the spin-dependent transport. First, the resonance frequency between the $|4, 4\rangle$ and the other qubit state $|3, 3\rangle$ must be determined. As mentioned in section 3.2, the free space resonance $\nu_0^{4\leftrightarrow 3}$ is altered by differential light shift effects. A precise measurement of the actual value of this frequency is inevitable for appropriate knowledge about the form of the coin-operator applied later. Once the correct resonance frequency is known, a typical Ramsey sequence can be executed as introduced in section 3.2. This measurement serves as a monitor for the reigning coherence times. Achieving the presented benchmark values of $T_2 = 200\mu\text{s} / T_2^* = 400\mu\text{s}$ have been the biggest experimental challenge due to many reasons (c.f. chapter 3).

The next step then focusses on the spin-dependent transport. To increase the transport efficiency it is ensured that atoms are axially cooled to their ground state. The method here is to directly couple to the lower vibrational state via microwave radiation. To achieve an overlap of both intrinsically orthogonal quantum states, the EOM is used to shift the two spin-dependent lattices slightly apart. A detailed description of this cooling mechanism is given in [34]. The signature of successful cooling is the disappearance ($< 3\%$) of the blue sideband in a recorded microwave spectrum. The cooling is later implemented as a part in the entire quantum walk sequence. Thereafter, the system is tested for maintaining its coherences while being transported spin-dependently. Associated dephasing issues are indebted to excitation processes during the transport.

step	procedure	comment
1	survival & push-out test	values to obtain: $\sim 100\%$ & 0%
2	microwave spectrum	free space resonance: $159.810 \text{ MHz}(+9.04\text{GHz})$
3	coherence time test	benchmarks: $T_2 = 200\mu\text{s} / T_2^* = 400\mu\text{s}$
4	axial sideband cooling	blue sideband is to decrease below $\sim 3\%$
5	magic transport time test	typical magic transport time $\sim 24\mu\text{s}$
6	performing QW sequence	see figure 4.1

Table 4.1.: Necessary preliminary characterisation and preparation measurements to perform experimental quantum walks. The procedures are given in chronological order and associated benchmarks are noted.

However, the *magic transport time* of $\tau_{\lambda/2} \sim 24\mu\text{s}$ for a trap depth of $100\mu\text{K}$ suppresses vibrational excitations, and thus maintains the length of the coherence times. The optimisation process is done by maximising the Ramsey contrast, hereby utilising a single atom interferometer [10]. After performing these preliminary characterisation measurements the apparatus is in principle in a state to perform quantum walks.

Figure 4.1 summarises the experimental steps of a single quantum walk sequence. It consists of five parts: Trapping and cooling of the atoms, initial imaging, state preparation of the atoms, performing the quantum walk and final imaging. Initially, there are about 5 atoms on average loaded to the lattice in order to increase the statistics. The atoms must be well separated from each other in order to be able to correctly identify them before and after the sequence. If atoms happen to appear too close to each other, i.e. the initial separation is less than the transport length caused by the following sequence, they will be sorted out by a post-processing software programme. The trapping itself and the spreading of the atoms can be optimised by tuning the MOT parameters. After the loading process the atoms are imaged for 1s in order to guarantee sufficient photon counting for the single-site resolution deconvolution. The position of every loaded atom functions in the following as the zero point. The atoms are then optically pumped into the qubit state $|\uparrow\rangle$, and axially cooled as described above. Finally, the atoms' desired initial quantum state is set. Typically, either the atoms are left in $|\uparrow\rangle$ or are brought into the $\frac{1}{\sqrt{2}}(|\uparrow\rangle + i|\downarrow\rangle)$ spin-state upon application of an according microwave pulse. Hereby, the initial preparation and imaging of the atoms is completed.

During the actual sequence, triggering the resonant microwave pulse of certain length and phase, which realises the coin, as well as the conditional shift operation by means of the EOM is achieved by pre-programmed waveform generators. Let a single operation block be composed of two coin and two (opposite) shift operations (see (4.2)), then the time length of this is given by twice the sum of microwave pulse, transport time and a small settling time ($\tau_{\text{set}} = 3\mu\text{s}$) in between. Although any unitary qubit operation can in principle be realised, for a typical quantum walk sequence the phase of the microwave pulse is set to $\pi/2$ and the length to a corresponding $3\pi/2$ rotation. According to (3.2) the experimental coin operation reads

$$\hat{C}_{\text{exp}} = \frac{-1}{\sqrt{2}} \begin{pmatrix} 1 & -1 \\ 1 & 1 \end{pmatrix} = -\hat{C}_{\text{EH}}. \quad (4.6)$$

A similar unbiased coin would be accomplished by a $\pi/2$ -pulse. However, experimental data has shown that the $3/2\pi$ -pulse results in a more robust¹ overall system. Since

¹It is believed that a consecutive application of this kind of pulse results in an effective multiple spin-echo process.

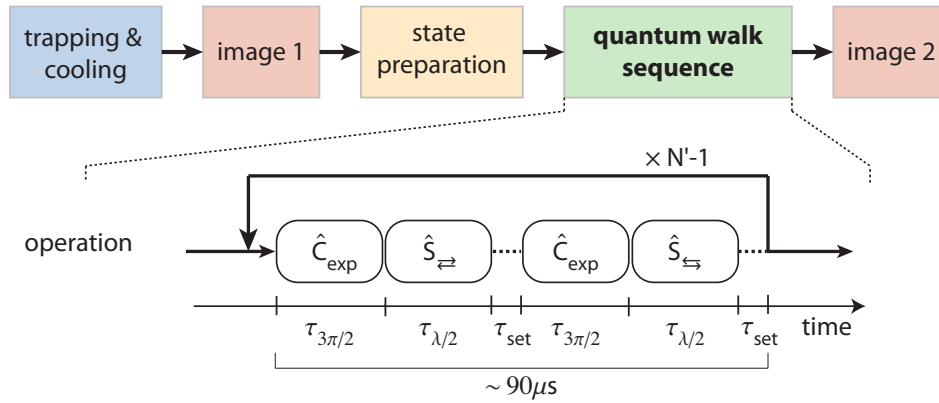


Figure 4.1.: Schematics showing the realisation of quantum walks with caesium atoms. The necessary alternating occurrence of the two shift operators only allows for an even step size of the walk. The length of a single sequence is $\sim 90\mu\text{s}$.

the length of such a coin is $\tau_{3\pi/2} \approx 3/2 \times 11\mu\text{s} = 16.5\mu\text{s}$, the entire length of the experimental walk operator is according to above $\sim 90\mu\text{s}$, and the length of a single step $\sim 45\mu\text{s}$. A repetition of this sequence block of N' times results in a $2N'$ -step quantum walk.

After completion of the sequence the lattice depth is increased, and the still coherently distributed atom is now probed with near resonant imaging light. Upon fluorescing, i.e. photon scattering, the atomic wave function collapses into one of the lattice sites with the corresponding probability. The atom is then again imaged for 1s, i.e. for the same time as before the sequence. The initial and final image is analysed, and the knowledge about the transport length is used to deliberately exclude unwanted data. The maximal possible distance defines a radius of interest. If there happen to appear more than one atom within this radius in two consecutive pictures, those detections will be neglected, since an unambiguous identification is not guaranteed. The repetition number of the sequence is chosen such that after this selection process about 200 atoms on average contribute to the final data set. Comparing the measured position to the initially measured starting point finally reveals the travelled distance of every individual system. Repeating the entire sequence for sufficiently many times allows for the reconstruction of the quantum walk's probability distribution.

4.3. Spin-decoherence model

Despite the fact that measured coherence times are much longer than the typical length of a single quantum walk step, decoherence effects are not at all avoidable nor negligible. As mentioned in section 3.2 these are mainly believed due to the radial motion of the atoms in the presence of differential light shifts. It is therefore inevitable to include these unwanted effects in a quantitative analysis.

Generally, decoherence can be understood as the *irreversible* disappearance of quantum coherences due to a coupling of a respective quantum system to an environment [55]. Their consecutive interactions lead to a *non-unitary* evolution of the system, e.g. the quantum walk in the present case. This non-unitarity requires the formalism of density matrix operators instead of the quantum state picture used before [56]. The

quantum walk density matrix operator is defined as follows

$$\rho_{\hat{W}} = \sum_{n,n',s,s'} \rho_{n,n',s,s'} |n, s\rangle \langle s', j'|, \quad (4.7)$$

where n and s indicate the position and spin states, respectively. An application of the walk operator (2.3) to a present quantum state needs to be replaced in this picture by an operation \mathcal{U} that maps the present density matrix operator to a new one. More explicitly this can be written as

$$\mathcal{U}\rho_{\hat{W}} = \sum_i \mathbb{U}_i \rho_{\hat{W}} \mathbb{U}_i^\dagger, \quad (4.8)$$

where \mathbb{U} is the so called *Kraus operator* describing the non-unitarities, and i denotes an index that runs over the evolutionary instances. In the unitary case \mathbb{U} is just the standard quantum walk operator (2.3). In the non-unitary case, however, an associated projection operation \mathbb{P}_i is added, which can be seen as a measurement process. Coherences are not fully removed from the system after every application of \mathcal{U} , though. Decoherence processes rather occur only with a certain probability p . Consequently, the one-step evolution can be broken into a unitary part and a non-unitary part according to²

$$\rho_{\hat{W}}(N+1) = (1-p) \hat{S} \hat{C} \rho_{\hat{W}}(N) \hat{C}^\dagger \hat{S}^\dagger + p \sum_i \mathbb{P}_i \hat{S} \hat{C} \rho_{\hat{W}}(N) \hat{C}^\dagger \hat{S}^\dagger \mathbb{P}_i^\dagger. \quad (4.9)$$

In fact, the projection \mathbb{P}_i and its associated probability does not have to be necessarily seen as a discrete event, but can equivalently describe a quantum system coupled to a Markovian environment with coupling strength p . This picture might be more appropriate for the actual experimental situation. In the following, two different models of decoherence shall be considered for comparison: *position-* and *spin-*decoherence. The quantum walk evolution (4.9) is adjusted accordingly by setting the sum index i to the respective position state index n or spin state index s , respectively. While the latter only runs over the two spin states $\{\uparrow, \downarrow\}$, n needs to consider all possible position states, i.e. $n = \{-N, \dots, N\}$.

Here, it is refrained from attempting to find an analytical solution to (4.9), but instead the individual effects of the decoherence are presented in form of numerical results. Figure 4.2 shows simulations of a 50-steps quantum walk under the presence of different decoherence parameters p for an initially chosen spin-state of $|s_0\rangle = \frac{1}{\sqrt{2}}(|\uparrow\rangle + i|\downarrow\rangle)$. It can be seen that for increasing p the quantum walk loses its characteristic features rather rapidly, and approaches the classical Gaussian distribution. Nevertheless, the two kinds of decoherences reveal distinct behaviours. Under the presence of spin-decoherence the distribution maxima shrink, and a simultaneous rise of a central peak can be notice. Contrary to this, the spatial decoherence first lets the edge peaks disappear almost completely, before the typical classical footprint emerges. Recalling the expected physical origins of the decoherence, it is assumed that the system only experiences spin-decoherence on the time scale of a quantum walk. Scattering events, which would lead to spatial decoherence, only occur with a rate of 10Hz. In addition, previous atom interferometer measurements support the assumption that spatial decoherence can be neglected [10].

As a first estimate, one would expect the level of decoherence to be comparable to the ratio of the duration of a single quantum walk step and the measured coherence

²Note that for reasons of abbreviation, here $(\hat{\mathbb{1}}_{space} \otimes \hat{C}) \rightarrow \hat{C}$

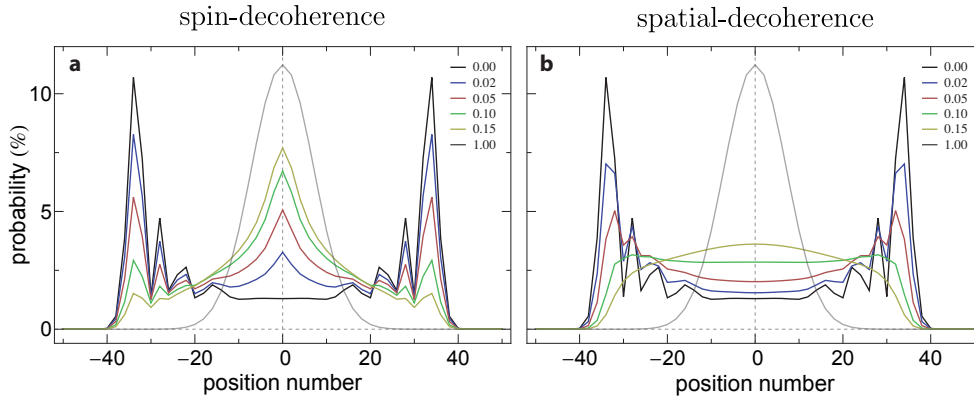


Figure 4.2.: Simulations of a 50-step unbiased quantum walk under the presence of (a) spin- and (b) spatial decoherence for an initially localised spin state of $\frac{1}{\sqrt{2}}(|\uparrow\rangle + i|\downarrow\rangle)$. The spatial probability distribution is plotted for different decoherence parameters p . For both cases the predominant edge-peak feature of the quantum walks vanishes quite rapidly, and the classically expected middle peak emerges.

time. Calculating p for T_2 and T_2^* using the benchmark values above yields 0.23 and 0.11, respectively. This, however, assumes a simple exponentially decreasing coherence contrast (objections to this are found in [42]) and neglects possible additional spin-echo effects due to coin-pulses. Hence, the actual value of p is believed to be smaller than the ones presented above. In fact, figure 4.2 shows that this is inevitable if one wants to successfully accomplish an experimental quantum walk showing all characteristic features. It shall be anticipated at this point already that decoherence effects are indeed not strong enough to qualitatively change the features of a quantum walk up to step numbers of $N = 100$ (see section 4.4). The presented model is still a very general approach to describe the effect of decoherence. A future task should involve the precise identification of the sources and mechanisms of decoherence, and implementing the knowledge about them into (4.9), i.e. expressing p in terms of physical quantities.

4.4. Results

Probability distribution

Following the experimental procedure as outlined in section 4.2, recordings of the quantum walk's probability distributions could be achieved. Figure 4.3 shows different realisations of such. Initial state conditions and step sizes are deliberately varied here in order to show the success of the quantum walk with respect to these parameters. Furthermore, the presented data was taken with considerable temporal separation, proving reproducibility. Again, about 200 atoms contribute to a single probability distribution. The error bars for every position were calculated by means of the Clopper-Person method [57]. The size of the binomial confidence intervals was chosen such that it resembles the typical σ of a corresponding normal distribution, i.e. $\sim 68\%$ confidence. The measured position information is converted into discrete separations of multiples of a single lattice site $\lambda/2$. In the following, however, all spatial information is described in terms of a single relative walking distance of $\lambda/4$, which intuitively compares more clearly to the presented theoretical model.

When looking more closely at the shape of the measured probability distribution one could first realise some deviations from the theoretical expectations: For some

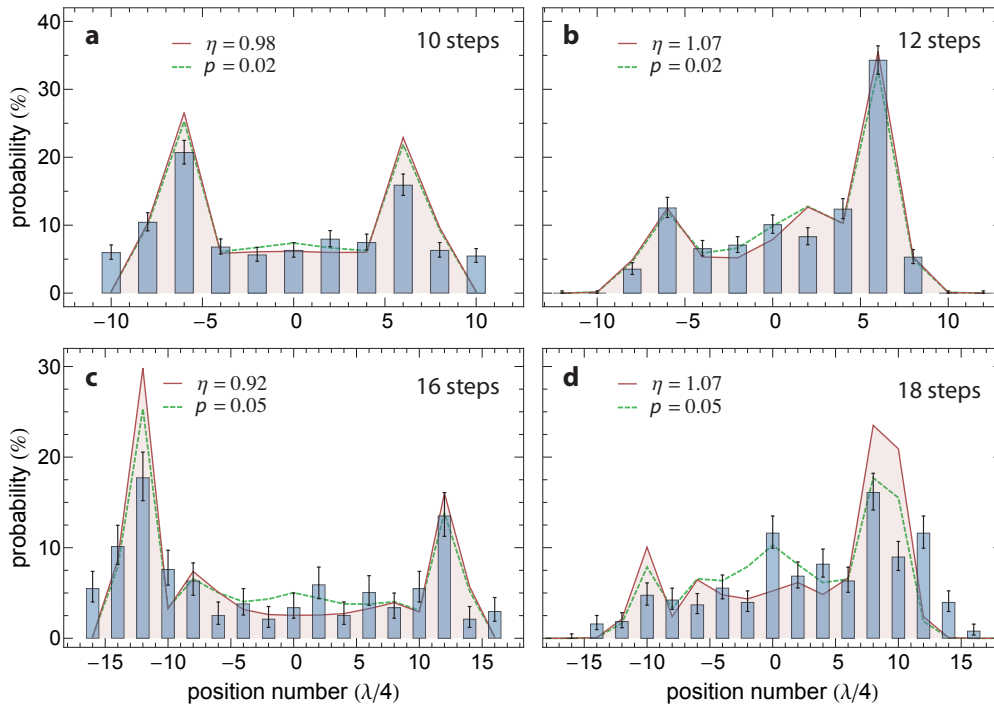


Figure 4.3.: Probability distributions showing the realisation of experimental quantum walks for different parameters. In (a) and (c) an initial spin configuration of $|s_0\rangle = \frac{1}{\sqrt{2}}(|\uparrow\rangle + i|\downarrow\rangle)$, and in (b) and (d) $|s_0\rangle = |\uparrow\rangle$ was chosen. Ideal theoretical curves (red) take an associated coin angle error into account, which is described by η . Estimating the level of decoherence leads to an adjusted curve (green) in every case. Errors on the state preparation in (a) and (c) can be observed in a resulting asymmetry of the probability distribution.

measurements the peaks of the distribution were observed to be closer to the center, and for others farther away for what can be expected from a coin of the form (4.6). This can be explained by an unexpected error on the coin angle. The real applied form of the coin rather reads

$$\hat{C}_{\text{exp}}(\eta) = \begin{pmatrix} \cos(\eta 3\pi/4) & -\sin(\eta 3\pi/4) \\ \sin(\eta 3\pi/4) & \cos(\eta 3\pi/4) \end{pmatrix}, \quad (4.10)$$

where η is a factor describing the experimental deviation from the desired value of $\theta/2 = 3\pi/4$. For $\eta = 1$ the ideal situation is recovered. As could be seen from section 2.2, and more precisely from (2.17) and figure 2.5, the spreading speed of the walk depends on the coin angle. Since the EOM shift direction alternates, enlarging the angle, i.e. $\eta > 1$, will decrease the spreading speed, and $\eta < 1$ will increase it (a systematic description as well as test of this behaviour will be shown below). Due to the strength of this dependence, even slight deviations in the low percent range cause significant differences in the outcome. Although the qubit resonance $\nu_0^{4 \leftrightarrow 3}$ as well as the pulse duration are calibrated on a daily basis by means of a microwave spectrum, it seems that the walk still sees a slightly different coin than desired. The length of the microwave pulse is typically varied in steps of $0.1\mu\text{s}$. The coin calibration takes place using the value for a full π rotation ($\sim 11\mu\text{s}$). This combined could explain a deviation of about 1%. A more dominant origin might be that the correct pulse was not determined carefully enough. Next to these systematic calibration errors, a

potential cause could also be found in the side-effects of the EOM. In its "ramped-up" configuration, the EOM might have a different polarisation impurity than in its 0V-status. This leads to varied differential light shift effects, which in turn give rise to an altered resonance frequency. Hence, every second microwave pulse would be slightly non-resonant, i.e. perform a different coin rotation. A double quantum walk step (4.2) then effectively yields a different angle θ per step. This effect could be investigated by comparing two spectra which had to be taken for both end-configurations of the EOM, respectively.

Nonetheless, the quantum walk's position information can be used to correctly post-calibrate the coin with an accuracy of 1%, i.e. $\eta \pm 0.01$. This is done by fitting the theoretical expectations to the collected data, and minimise the sum of squares by adjusting η . The procedure is typically applied for reasonably small step sizes ($\sim 10 - 16$), where decoherence processes can be generally still neglected (see below). Additionally, an error on the measured π pulse not only effects the coin, but also the initial state preparation. When trying to bring the system into the spin state $|s_0\rangle = \frac{1}{\sqrt{2}}(|\uparrow\rangle + i|\downarrow\rangle)$, an error puts it rather to $|s_0\rangle = \cos(\eta' \frac{\pi}{4})|\uparrow\rangle + i \sin(\eta' \frac{\pi}{4})|\downarrow\rangle$. This leads to an imbalance of the qubit amplitudes, and hence to an asymmetric probability distribution of the walk. Making the assumption that the pulse error originates solely from systematic characterisation errors, i.e. that the outlined potential impact of the EOM is neglected, then $\eta' \approx \eta$, and the imbalance is directly correlated with the spreading speed. In other words, the imbalance is a statement about the quality of the desired microwave pulse. The spin state $|s_0\rangle = |\uparrow\rangle$, on the other hand, is purely prepared by means of optical pumping, and therefore does not show this effect at all.

Figure 4.3 shows the theoretical prediction corresponding to the true coin of the quantum walk (red solid lines) as well as takes into account associated state preparation faults. Comparing these expectations with the data taken, it can be stated that quantum walks up to 20 steps can be performed with a very high reliability. Particularly for smaller step sizes, the probability distribution seems to almost fully agree with the theoretical curve. Moreover, in figures 4.3(a) and (c) the effect of a pulse error on the initial state preparation can be observed. Here, the assumption $\eta' \approx \eta$ seems to fit quite well. Turning the argumentation around, the sensitivity regarding coin shape and initial state configuration allows the quantum walk to be in fact a good quantum measuring tool of such, assuming that sufficiently statistics are provided.

The spin-decoherence model presented in section 4.3 has been applied as well (green dashed lines). Nevertheless, in the cases (a) and (b) this seems negligible, and even in the higher step example (c) it only plays a minor role. In (d), though, the effect seems to become stronger. For walking steps above $N \sim 20$, decoherences start to affect the system considerably, and thus have to be taken into account. The estimation of this is described below.

Spin-decoherence model in action

The decoherence mechanisms in the presented system are not understood to a level that would allow parameter-free fitting of the model outlined in section 4.3. Hence, adjusting the amount of spin-decoherence to the experimental results requires empirical quantification of the decoherence parameter p . In general, this is done by using the determined value for η , and decreasing the sum of all squared probability differences between model and real data by raising p until a minimum is reached. This procedure is usually applied to quantum walks of large enough step sizes ($N \gtrsim 20$), where decoherences do have a significant impact. By doing this for different step numbers of

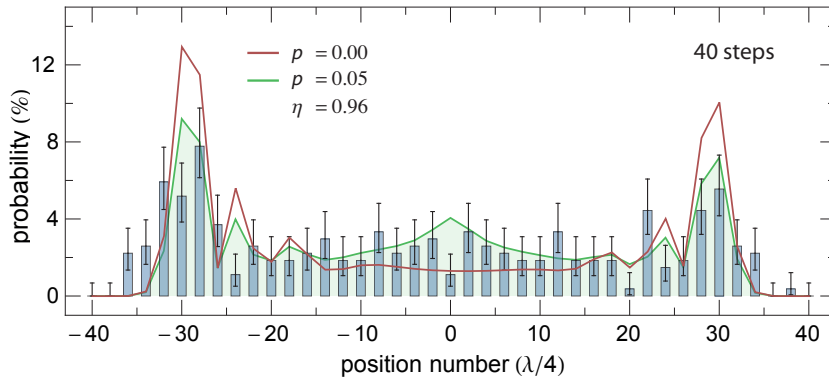


Figure 4.4.: Effect of the spin-decoherence model on an 40-step experimental quantum walk. The paramters η and p were found according to the description in the text.

the same measurement set, a value for p is found with a usual confidence interval of ± 0.01 . Figure 4.4 shows exemplarily the effect of the spin-decoherence model on taken data for a quantum walk of 40 steps ($\eta = 0.96 \pm 0.01$). It can be observed that the discrepancies between measurement and ideal theoretical curve can be nicely explained by this model. All quantum walks of appropriate step size show in general the characteristics of spin-decoherence: The outer peaks shrink, while a central peak emerges. This gives reason that the right model is indeed chosen here, and that the collected data is explained considerably well by this.

Clearly, the level of decoherence depends strongly on the daily performance of the experiment, its calibration and alignment. However, by using the outlined procedure to find p , the value was steadily determined to be around 0.05 for an optimised setup. This contradicts the first a priori guess from section 4.3 that the value should be comparable to the fraction of sequence- and coherence time. In fact, p seems to be smaller, i.e. better, by a factor 4(2) than what would have been assumed from $T_2(T_2^*)$. The reason for this should indeed be found in the relatively rapid application of $\frac{3\pi}{2}$ -pulses, mimicking some kind of spin-echo effect as already suggested. In detail, however, the origin of this phenomenon remains concealed. Finally, by introducing idle times between single walk steps, i.e. intentionally making the system more accessible to decoherences, the transition from quantum to classical behaviour can also be experimentally observed just as in figure 4.2.

Ballistic transport

An alternative way to present the remarkable features of quantum walks is to express the measured probability distributions (as in figure 4.3) in terms of their second moment. The transformation into the corresponding root-mean-square value (RMS³) as well as the associated error propagation happens by standard means. In this picture the global transport property becomes clearly evident. Chapter 2 has shown that an ideal quantum walk should show ballistic spreading. Figure 4.5(a) presents RMS data for a measured quantum walk of up to 100 walking steps for an initial intended spin-state of $|s_0\rangle = \frac{1}{\sqrt{2}}(|\uparrow\rangle + i|\downarrow\rangle)$. The corresponding evolution of the probability distribution is shown in figure 4.5(b) for a selection of walk lengths. The error bars increase strongly

³Here, the RMS-value and not the standard deviation σ was deliberately chosen to be the quantity of interest. The reason is that this value is independent of the initial spin configuration $|s_0\rangle$ and allows for testing the spreading speed.

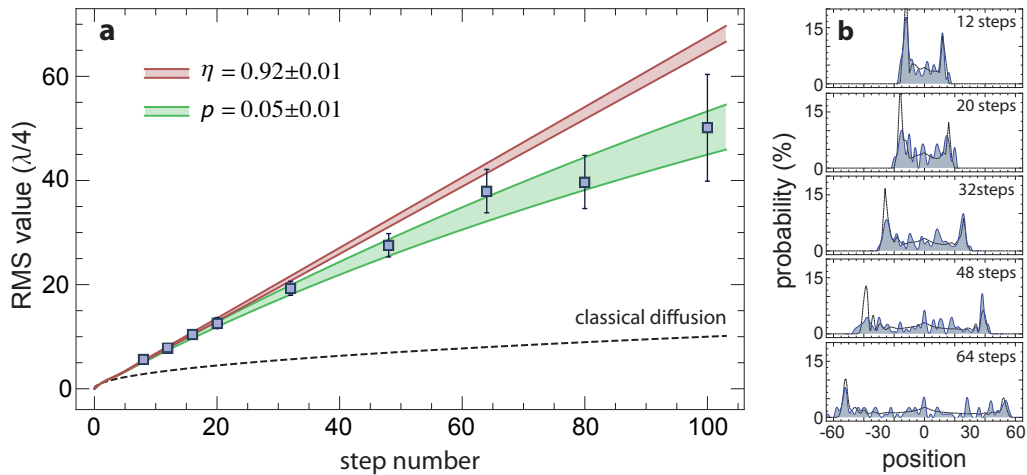


Figure 4.5.: The RMS sizes of an experimental quantum walk for up to 100 steps are shown in (a). Coin imbalance is given by $\eta = 0.92 \pm 0.01$ and the decoherence parameter was found to be $p = 0.05 \pm 0.01$. Plotted curves respect these uncertainties. Up to ~ 20 steps the quantum walk follows nicely the ballistic expansion. Only then decoherence processes become substantial. In (b) corresponding probability distributions, and hence the real space spreading of the walk is exemplarily presented. Here, shaded regions are experimental data, and the theoretical expectation is given by a black solid line.

while moving to larger sequences due to the fact that the number of individual walkers was kept approximately the same. For step sizes of up to about 20 the walk follows very accurately the expected linear behaviour, confirming what has been stated above. Then, however, decoherence processes changes the pure linear relationship. A typical square-root behaviour is superimposed, representing the quantum-to-classical transition. Nonetheless, this effect is far away from destroying coherences completely. This can be seen when comparing the experimental data to the classical RMS-curve (black dashed line). The ideal quantum walk is plotted for a measured coin correction factor of $\eta = 0.92 \pm 0.01$. The decoherence parameter was determined to be $p = 0.05 \pm 0.01$. The upper boundary of the spin-decoherence curve corresponds to a smaller coin angle and lower decoherence level ($\eta = 0.91, p = 0.04$), and vice versa for the curve's lower bound ($\eta = 0.93, p = 0.06$). It can then indeed be observed, that all experimental data points agree within their error bars with the expectation. Since for very high step numbers the range of uncertainty as well as the error bars of the taken data are rather large, a more precisely determined coin and the acquisition of many more measurements is suggested. Nevertheless, the system's dynamics are described very well by the assumed model.

In comparison to previously achieved quantum walks with single caesium atoms [1, 18], the results presented here exceed qualitatively as well as quantitatively what has been shown before. It was possible to observe experimental quantum walks for step sizes that are four times larger than what was done in the past. The coherences could be maintained significantly longer such that almost decoherence-free walks are possible up to almost 20 steps. This, however, has to remain a qualitative statement, since the decoherence model described here was not applied in the previous case. Reasons which might support the improvement can be found in the newly installed two-arm setup and in the enhanced focusing of the dipole trap, respectively. Lowering the beam waist increases the radial trap frequency, and hence narrows the vibrational

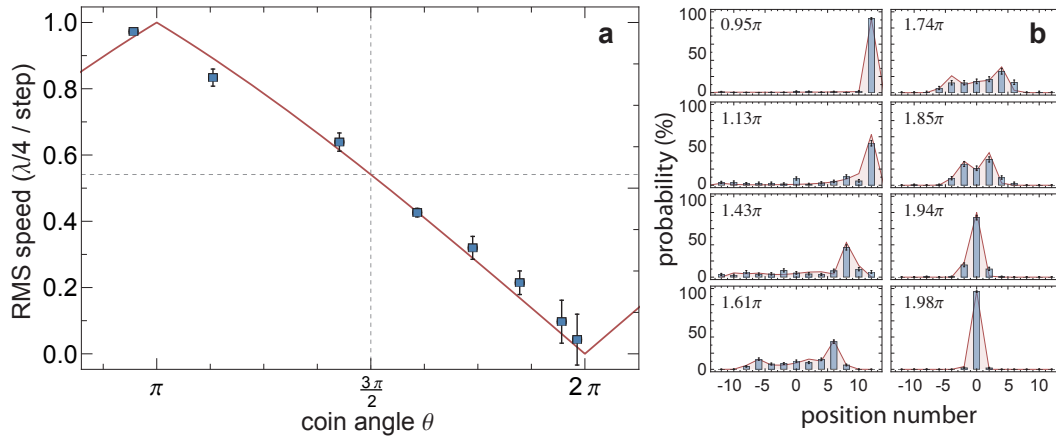


Figure 4.6.: Dependence of the quantum walk’s spreading speed on the coin angle. (a) shows the RMS values of 12-step walks as a function of θ . The corresponding probability distributions are seen in (b). The theoretical curves (red) is given without the effect of decoherence.

state population density distribution. Inhomogeneous dephasing might be suppressed accordingly. Attempts to improve the general set-up on all fronts such as magnetic stray field suppression or the Ti:Sa phase- and frequency stabilisation, for example, certainly further explains the raised quality of the results. Another aspect is the fact that the experiment was performed in a shallower lattice than before. This reduces generally all negative effects associated with the optical potential, and should also give rise to a larger coherence time. The presence of decoherence does not need to be necessarily seen as a pure negative effect, though. Detailed knowledge of the decoherence mechanisms provided, quantum walks could serve as a powerful tool to study the quantum-to-classical transition in more detail.

Spreading speed

The sensitive behaviour of the quantum walk’s spreading speed on the coin angle is a direct consequence of the properties of the underlying energy bands describing this system (c.f. chapter 2). The different measured speeds have so far been identified as unwanted effects. But it is also worthwhile to systematically investigate the RMS spreading as a function of the angle. Figure 2.5 already shows the theoretically expected behaviour for an ideal quantum walk. However, due to the EOM properties it can be shown that for the consequential experimental quantum walk operator (4.2) this curve is shifted in θ by π , i.e. $v_{\text{exp}}^{\text{rms}}(\theta) = v^{\text{rms}}(\theta + \pi)$. An intuitive picture is quickly obtained by realising that the system has to remain localised for pulses that do not change the spin state ($\theta = 0, 2\pi$), and has to travel at maximum speed for those that do ($\theta = \pi$). Now, by varying the length of the applied microwave pulse intentionally, this dependence can be experimentally investigated. Due to the expected symmetry, the corresponding angle is only altered between π and 2π (or equivalently $\eta \in [\frac{2}{3}, \frac{4}{3}]$).

Figure 4.6 presents the experimental data for different values of the angle θ . Here, 12-step quantum walks of an initially prepared spin-up state were recorded. This particular step size was chosen since it is long enough to determine the spreading speed sufficiently, but is still in the range where decoherence effects can be conveniently neglected. Thus, the theoretical curve is presented without the impact of the spin-decoherence model. In figure 4.6(a) this is depicted together with the experimental RMS values. The

corresponding spatial probability distributions are shown in figure 4.6(b). It can be observed that the RMS data as well as the measured distributions agree very nicely with the expected relation. In fact, the deviation to the ideal theoretical curves is minimal. By this, not only the quantum walk's dynamics, but also the properties of the underlying energy bands could be systematically investigated and controlled. It can be concluded that they indeed behave as expected. The next step will be now to test these bands not "statically", but rather to introduce additional dynamics by applying a force to the system. The consequences and effects revealed by the quantum walk system are at the focus of the following chapter.

Chapter 5.

Electric quantum walks

After having presented the experimental realisation of quantum walks in the previous chapter 4, the next step is to explore more the fundamental features of such a system. As shown in section 2.2 the properties of the quantum walk are governed by an underlying band structure. Such systems are very well known from the field of solid state physics, where distinguished bands are the result of interactions between the electrons and nuclei in the solid [58]. The formal similarity to the quantum walk allows to simulate long known and investigated phenomena with the latter. One question that was already addressed by Felix Bloch in 1929 deals with the consequences for a system consisting of energy bands under the presence of a static force. It could be shown that the dynamics are described by an oscillatory motion in this case, resulting in a localised quantum particle. This effect is known as *Bloch oscillations*. Though low coherence times and the lack of accessibility make it impossible to witness this phenomenon in solid materials, it was first demonstrated by the cold atom community in the mid 90's [24–26]. Despite revealing some distinctions, quantum walks make it now possible to study this continuous time effect also in a temporal discretised environment. Since the considered force on electrons is typically caused by an electric field, the quantum walk system experiencing a similar force shall be referred to as an *electric quantum walk*. The concept presented is based on discrete accelerations of the system. This chapter is composed of a theoretical view on the idea of an electric quantum walk and its experimental realisation, including results.

5.1. Theory

5.1.1. Bloch oscillations

Periodic systems can be conveniently viewed in the momentum space representation, since the Brillouin zone has a finite size. The dispersion relation, i.e. the behaviour of the system's energy as a function of the momentum parameter k , can then be entirely folded into this region. This leads to the formation of the so called Bloch bands or energy bands, which are continuous over this interval. The interactions of the system with its environment causes the transition between bands to lose their continuity, and band gaps are the consequences. This situation is most prominently known for electrons in solid materials, where spatially fixed ions create the periodic potential. As long as there is no impact on the quantum particle, the system remains in a given momentum state on a band. However, if an external force is present, e.g. a static electric field on electrons, the system gets accelerated and the momentum experiences a change according to

$$\hbar dk/dt = -F, \quad (5.1)$$

with F being the force applied [58]. Note that (5.1) is a semi-classical approach not allowing for any quantum mechanical tunnelling effects. The system gets dragged

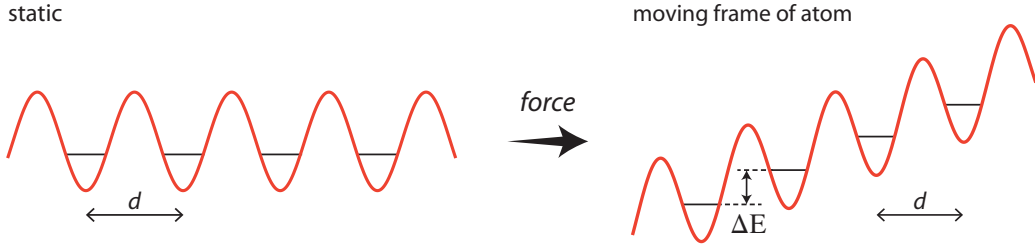


Figure 5.1.: Periodic potential with a characteristic lattice spacing of d shown a) in the static case and b) presented in the co-moving frame of the trapped system while being accelerated. This force lifts the degeneracy of the lattice energy states by an energy differences of $\Delta E = Fd$.

along the energy band in which it is located. Hereby, the particle experiences the full dynamical properties offered by the band. Once the system reaches the edge of the Brillouin zone at π/d it gets reflected and appears at the other edge at $-\pi/d$. Assuming a simple sinusoidal form of the energy band, e.g. $\epsilon = \epsilon_0 [1 - \cos(kd)]$, where d is the lattice spacing, allows to analytically calculate the velocity v and position x of the particle. The expressions yield

$$v = (d\epsilon_0/\hbar) \sin(kd) \quad , \quad x = -\epsilon_0/F [\cos(-Fdt/\hbar) - 1] \quad . \quad (5.2)$$

It is clear that the quantum particle shows oscillatory behaviour regarding velocity as well as position called *Bloch oscillations*. The motional oscillation happens at a frequency of $\omega_B = Fd/\hbar$, the so-called *Bloch frequency*. So the weaker the force, the larger the oscillations (in time). In conclusion, the behaviour of a quantum particle confined to a periodic potential is tremendously different to the free particle case in which the system is accelerated in a constant fashion.

5.1.2. Electric quantum walks in position space

In general, a force can be understood as the derivative of a potential according to $F = -\nabla\Phi$. So the presence of a *static* force superimposes a linear potential onto the existing one. For a given crystalline structure the consequence is a tilt of the lattice. This picture remains the same both for electrons in a solid experiencing an electric field and for neutral atoms in an optical lattice being accelerated by the lattice itself (see section 3.4). As can be seen from figure 5.1, the tilt lifts the degeneracy of the energy levels of the lattice. The shift is proportional to the exerted force. According to the laws of quantum mechanics, the time evolution of a system bound to a static potential depends on its energy state. Here, this evolution will be position-dependent and identical systems on adjacent sites pick up a relative phase according to

$$\hat{U} = e^{i\Delta Et/\hbar} = e^{iFdt/\hbar} = e^{i\phi\tau} \quad \text{with} \quad \phi = \frac{2\pi}{m} \quad , \quad (5.3)$$

where ΔE is the energy difference between adjacent lattice sites, F is the applied force, d is the lattice constant¹ and τ denotes the dimensionless time unit. Additionally, the assumption $\hbar = 1$ shall be made from now on. So in the presence of a crystalline

¹Note that this has to be set to $d/2$ in the presented experimental quantum walk system. The reason is that a single shift operation translates the spin-dependent lattices by only half a lattice site. However, as long as this effective lattice constant is later taken into account (see section 5.2) the theory and its associated conclusions remain the same.

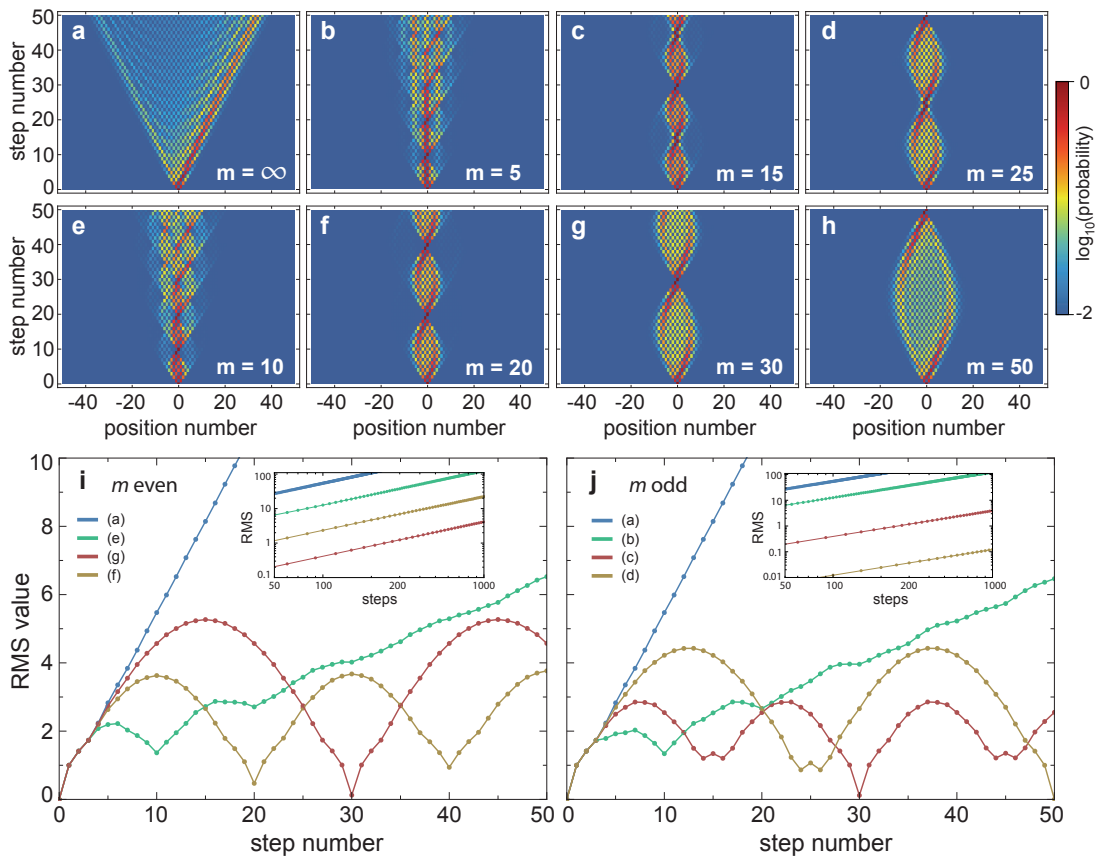


Figure 5.2.: Simulated Bloch oscillations in discrete Hadamard quantum walks for different force parameters m and an initially localised spin-up state $|\psi_0\rangle = |0, \uparrow\rangle$. (a) shows the position space evolution of an ordinary quantum walk as defined in equation (2.3). In (e)-(g) the evolution of a quantum walk under the presence of an even force parameter for $m = 10, 20, 30, 50$ can be seen. The odd values $m = 5, 15, 25$ are presented in (b)-(d). The corresponding RMS values are plotted in (i) and (j), respectively. Contractions are generally better for higher values of m . For odd m -values a proper revival occurs after $2m$, hence an even number of steps. The insets show a double logarithmic plot up to 1000 steps to reveal the asymptotic ballistic nature of every accelerated walk. Here, only the points of local minima at every m for even or $2m$ for odd are plotted, respectively.

potential an applied static force can be reduced to a lattice site-dependent phase accumulation of the system, which can be expressed as a fraction of 2π . In the following the fraction parameter m will be referred to as the force parameter. In general, m can be any real number, but for now it will be chosen to be an integer.

This picture can now be used to formulate the mathematical framework for the acceleration of quantum walks. To maintain the discreteness of the system and its evolution, the force shall be represented by a discrete unitary operator as well. The idea is to multiply the lattice-site dependent phase to the system, hereby simulating the force. The operator is then newly defined as follows

$$\hat{F} = \sum_n e^{-i\phi n} |n\rangle\langle n| \otimes \hat{\mathbb{1}}_{\text{coin}}, \quad (5.4)$$

where the dimensionless time τ is set to one for a single application of \hat{F} . It is clear from the form of (5.4) that the force only acts on the orbital degrees of freedom, i.e.

$\mathcal{H}_{\text{space}}$, and treats both spin states equivalently. The quantum walk as introduced in (2.3) can now be extended to an accelerated system by subsequently letting \hat{F} act on the system. The evolution operator of the "electrified" system can then be formulated as

$$\hat{W}_{\text{el}} = \hat{F} \cdot \hat{S} \cdot (\hat{\mathbb{1}}_{\text{space}} \otimes \hat{C}), \quad (5.5)$$

where \hat{S} and \hat{C} are generally defined according to (2.2) and (2.1), respectively. Iterative application of (5.5) to an initially chosen system yields an accelerated or electric quantum walk after N steps, i.e.

$$|\psi_N\rangle_{\text{el}} = \hat{W}_{\text{el}}^N |\psi_0\rangle. \quad (5.6)$$

As it was the case for the ordinary quantum walk, the exact shape of this kind of walk depends severely on the precise form of the coin \hat{C} . Here, the force parameter m plays an even bigger role. Different behaviour to the normal "walk"-system is expected due to quantum interferences of the relative phases accumulated. In order to obtain a qualitative as well as quantitative picture, one shall fix \hat{C} in the following to the form of the previously defined experimental Hadamard coin \hat{C}_{EH} (see section 2.2). Spin-independent quantum measurements reveal a spatial probability distribution. Simulations of electric quantum walks in position space are shown for different values of m in figure 5.2(a)-(f) for an initial state of $|\psi_0\rangle = |0, \uparrow\rangle$. One can clearly see that the presence of the additional force operator results in an oscillatory behaviour of the probability distribution, which can be analogously seen to the phenomenon of Bloch oscillations. For the first few steps the wave packet travels into the same direction as it is the case without any force applied. Then, however, the peak starts to disappear and to simultaneously emerge on the opposite side. Subsequently, keeping its direction of movement there will be a contraction of the walk. The period of oscillation is given by the value of m . However, only an even number of steps quite clearly allows the system to return to its initial position again. This leads to the fact that for m even a revival at the starting point occurs after m steps, but for odd m values this can only take place after $2m$ steps. It can also be seen that the revivals of the latter case are qualitatively better at $2m$. Nonetheless, despite showing oscillations the walk seems to spread out. The stronger the force, i.e. the smaller the value of m , the faster this spreading occurs.

An alternative way to observe the general oscillatory behaviour is to find the width of the distribution in form of the second moment. In figures 5.2(i) and 5.2(j) the RMS values are plotted against the step number for even and odd m -values, respectively. The predominant feature of revival can be nicely observed in this picture as well. The true periodicity of $2m$ in the odd case can also be noticed. On top of that, by plotting only the revival minima for a larger number of steps in a double-logarithmic fashion (insets), it becomes apparent that electric walks do not experience pure refocussing. They rather asymptotically maintain a ballistic expansion, which is evident from the consistency of all slopes in the log-log plot. This behaviour is totally unexpected from the continuous time example. Nevertheless, in the presence of a force this expansion is much slower than in the non-accelerated case and depends strongly on m . In fact, the dynamics for odd values of m and corresponding even values of $2m$ reveal a very peculiar behaviour: besides the fact that revival position coincide every $2m$ steps, it can be shown that the asymptotic behaviour is exactly the same. Motivation and prove of all these characteristics and peculiarities can be found below.

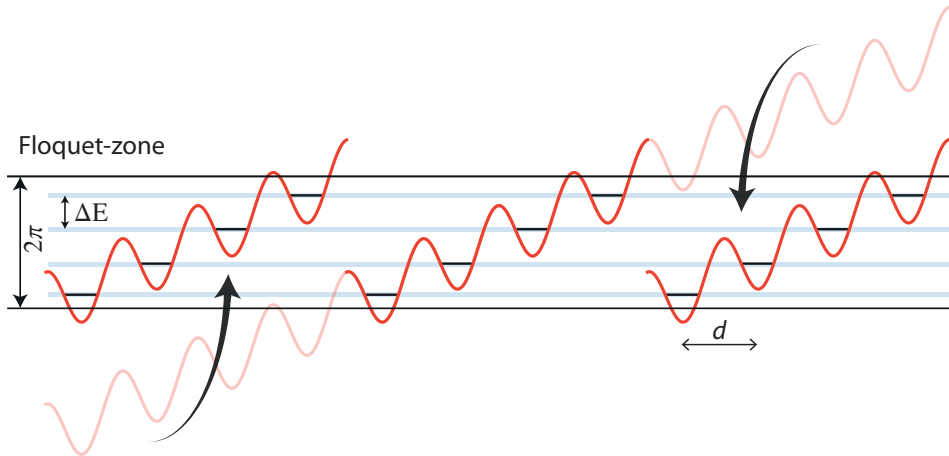


Figure 5.3.: Folded energy states of an accelerated periodic potential into the Floquet-zone $[0, 2\pi]$ as a consequence of the temporal discreteness of the system. The effective potential caused by the acceleration is sawtooth-like rather than purely linear. The new periodicity of md allows for resonant tunnelling and explains the asymptotic ballistic expansion of any commensurate electric quantum walk.

5.1.3. Resonant tunnelling

An ideal periodic potential being accelerated becomes tilted according to figure 5.1, and, hence, the translational invariance gets broken. In the continuous time case, Bloch bands are broken into Wannier-Stark ladder states in the presence of such a washboard-like potential [26]. This results in a full localisation of the particle, and is the origin for the oscillatory motion of a quantum particle in such a system. Despite the fact that the mentioned potential forms also the setting for the quantum walk under consideration, full localisation can not be observed, and every electric quantum walk exhibits ballistic expansion in the asymptotic limit. The insets of figures 5.2(i) and 5.2(j) show electric quantum walks for a large number of steps. To get a physical understanding of this phenomenon it is essential to recall the consequences of having a time discrete system. As explained in chapter 2, energies are only defined up to 2π in rescaled units, i.e. become quasi-energies. This feature requires to fold all energy states into the so-called Floquet-zone [59], which spans from 0 to 2π . The wrapping process of the energy states is illustrated in figure 5.3. The potential generated by the force is locally linear, but after the folding resembles a new periodicity of m lattice sites.

The ballistic expansion originates from the quantum tunnelling occurring across sites sharing the same energy. In the continuous time case the system can tunnel through the potential barriers, hereby causing the transition to another band. This is called *Landau-Zener tunnelling* [26]. Here, tunnelling processes would also be possible, but owing to the energy wrapping this would occur in a resonant fashion. This in turn would allow the system to coherently delocalise in the presence of a force. So keeping the language of continuous time systems, this resonant tunnelling process can be identified as the mechanism causing the ballistic expansion of a quantum walk. Since the tunnelling is more likely if the period of wrapping is smaller, faster expansion generally occurs for stronger forces, i.e. smaller values of m . Note again that in this analogy with continuous time systems tunnelling is not a real process, but rather simulated due to the underlying structure of the quantum walk under acceleration.

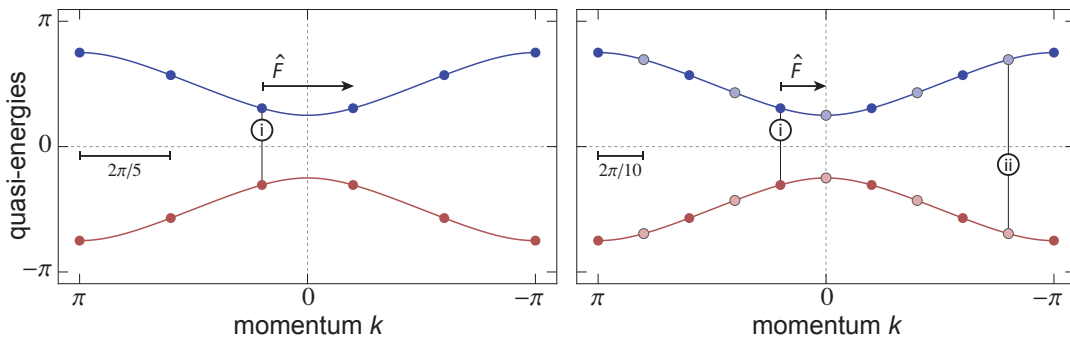


Figure 5.4.: Dispersion relations of the non-accelerated quantum walk \hat{W} showing the translations in k associated with force parameters $m = \{5, 10\}$. The system is assumed to be initially localised at (i) and then translated by $\frac{2\pi}{m}$. Full circles in (a) correspond to a relative shift of $\frac{2\pi}{5}$. Halving the shift adds additional points indicated by fainter ones in (b). Due to the symmetry of the bands and the underlying eigenvectors, projecting a given state on (i) or (ii), respectively, reveals the same dynamics of the system.

5.1.4. The force effect in k -space

The impact of the force shall be studied more fundamentally by looking again at the quantum walk's dispersion relation as shown in figures 2.3 and 2.4. A system that is well localised in momentum space on a given energy band shall be considered. As shown above, in a continuous time system an applied force steadily translates the system along the band until a Bragg reflection occurs. Here, however, the system would be shifted in the momentum parameter k due to the discreteness of the force. According to (5.3) the shift equals $\frac{2\pi}{m}$ in size such that the Brillouin zone is scanned stroboscopically only depending on the force parameter m (see figure 5.4). Clearly, after m steps a total shift of 2π is acquired and a full revolution within the Brillouin zone is experienced. The scanning of the bands allows the system to exhibit different velocities with different directions. This, analogously to the continuous example, explains why a revival of the quantum system takes place after one revolution.

It is crucial to realise now that this picture is not at all complete, since the spin component has been so far neglected. As illustrated in chapter 2, particularly in equation (2.13) and figure 2.3, the spin eigenstates corresponding to the energy bands have an intrinsic dependence on the momentum parameter k . Thus, translating the system in momentum space projects it onto a different set of spin eigenstates. However, the force operator (5.4) only acts on the position space $\mathcal{H}_{\text{space}}$ and leaves the coin space $\mathcal{H}_{\text{coin}}$ untouched, i.e. preserves the real spin of the system. This means that the population of both bands must have been (partially) exchanged after the application of the force. This population transfer requires tunnelling between the two bands, which again can be interpreted as Landau-Zener tunnelling. The entire size of the Brillouin zone corresponds to exactly one revolution of the Bloch vector around the given axis in figure 2.3(b), meaning that the system stays fully in the same band only when its translated by 2π ($m = 1$), which is equivalent to no shift at all. For all other cases there will be a (partial) mapping to the other band. Owing to the symmetry of the energy bands, switching to the quantum state on the other band means also reversing the group velocity. Hence, there will be a certain part of the system that does not experience all different velocities while being discretely transported through the band, but rather remains moving in a particular direction. As a result the system can escape and is not purely localised. In the extreme case of shifting by π , i.e. $m = 2$, the system

is mapped from one to the other band as a whole². This goes hand in hand with mapping onto exactly the same dynamics as before the force was applied. Consequently, this leads to the fact that quantum walks under the presence of a force corresponding to $m = \{1, 2\}$ show identical behaviour to ones that are not subject to a force at all.

Additionally, by using a similar argument it might be explained why odd values of m should reveal the same asymptotic dynamics as even values with $2m$. Figures 5.4(a) and (b) shall give an explicit example for the cases $m = \{5, 10\}$ which would be generally applicable. Consider a system that is initially localised at (i). Upon applying \hat{F} it will be translated by $\frac{2\pi}{5}$ or $\frac{2\pi}{10}$, respectively, and the overlap with the two bands changes accordingly. For the odd case there will never be an overall shift of exactly π after a certain number of application steps. Since only shifting by π fully maps the state onto the other band, and therefore maintains the same velocity, in the odd case every total shift $2\pi\frac{N}{m}$ in k produces a *unique* projection onto the bands. When halving the force now, i.e. doubling m , there appear twice as many positions in the Brillouin zone where the system is shifted to. Hereby, "mirror-positions" to the existing ones in the odd case emerge, meaning that after $m/2$ further steps the system is in total translated by π . An example is given by (ii), which is a mirror position to (i). Projecting the same state onto (i) and (ii), respectively, produces the same velocity. This identity effect which was already shown for the $m = 2$ case, could then also be found in any even m case. Thus, from a dynamics point of view it would be fully equivalent to go around twice the Brillouin zone for m being odd or just once for $2m$. Consequently, these two cases would asymptotically always reveal the same behaviour. When doubling an even m there will also be more shift positions in the k -space, but no complementary emerging ones. This would lead to the fact that here the effect of an equivalent dynamic cannot be observed. However, this intuitive picture still needs mathematical proof.

5.1.5. Spectrum of the electric walk operator

A quantitative treatment of the quantum evolution of electric quantum walks requires the energy spectrum of the newly defined system (5.5) to be determined. It is clear that the presence of the force (5.4) does not allow to treat the system as a 2x2 problem any more as done in chapter 2. Nevertheless, there is a way to keep the problem tractable by redefining the unit cell of the lattice, hereby extending it from one site to m sites. This also regains the property of translational invariance of the system. The corresponding mathematical process shall be called *regrouping*. Here, this regrouping can be either performed spatially or temporally.

Spatial regrouping

As mentioned above the presence of a commensurate force enlarges the unit cell³ of the system from 1 to m . So the position state $|n\rangle$ can be conveniently re-defined as

$$|n\rangle \longrightarrow |nm + j\rangle = |nm\rangle \otimes |j\rangle \quad (5.7)$$

where $n \in \mathbb{Z}$ and $j = \{1, \dots, m\}$. The Hilbert space $\mathcal{H}_{\text{space}}$ spanned by these position states can subsequently be understood as $\mathcal{H}_{\text{space}} = \mathcal{H}_{\text{space}}^n \otimes \mathcal{H}_{\text{space}}^j$. The subspace $\mathcal{H}_{\text{space}}^j$ describes the new unit cell.

²recall that the two Bloch vectors representing both bands are π out of phase with respect to the plane shown in figure 2.3b

³Note that the lattice constant d has been set to 1 for reasons of convenience.

When Fourier transforming $\mathcal{H}_{\text{space}}$ into \mathcal{H}_k the corresponding basis states can be expressed in terms of each other as

$$|nm\rangle \otimes |j\rangle = \frac{1}{\sqrt{2\pi}} \int dk e^{-iknm} e^{-ikj} |k\rangle, \quad (5.8)$$

$$|k\rangle = \frac{1}{\sqrt{2\pi}} \sum_n e^{iknm} |nm\rangle \otimes \sum_j e^{ikj} |j\rangle = |k\rangle_n \otimes \underbrace{\sum_j e^{ikj} |j\rangle}_{|j\rangle_k}. \quad (5.9)$$

Here, the momentum state is also described as a direct product. This is formed by the Fourier-transformed position state $|nm\rangle$ and a newly defined basis state $|j\rangle_k$. In the next step the operators \hat{C} , \hat{S} and \hat{F} shall be Fourier-transformed using these basis sets. The analytical expressions read

$$\hat{C}_k = \int_{-\pi/m}^{\pi/m} dk |k\rangle_n \langle k|_n \otimes \sum_{j'} |j'\rangle_k \langle j'|_k \otimes \hat{C}, \quad (5.10)$$

$$\hat{S}_k = \int_{-\pi/m}^{\pi/m} dk |k\rangle_n \langle k|_n \otimes \left[\underbrace{e^{ik} \sum_{j'} |j'+1\rangle_k \langle j'|_k}_{\hat{S}_k^{j,\uparrow}} \otimes |\uparrow\rangle \langle \uparrow| + e^{-ik} \sum_{j'} |j'-1\rangle_k \langle j'|_k}_{\hat{S}_k^{j,\downarrow}} \otimes |\downarrow\rangle \langle \downarrow| \right], \quad (5.11)$$

$$\hat{F}_k = \int_{-\pi/m}^{\pi/m} dk |k\rangle_n \langle k|_n \otimes \underbrace{\sum_{j'} e^{-i\phi j'} |j'\rangle_k \langle j'|_k}_{\hat{F}_k^j} \otimes [|\uparrow\rangle \langle \uparrow| + |\downarrow\rangle \langle \downarrow|]. \quad (5.12)$$

The momentum k is defined over the Brillouin zone which spans over the range $[-\pi/m, \pi/m]$. Due to the regrouping all operators are diagonal in $|k\rangle_n$, and thus can be reduced to systems of the subspaces $\mathcal{H}_k^j \otimes \mathcal{H}_{\text{coin}}$ only. They can then be represented by unitary matrices of dimensionality $2m \times 2m$, i.e.

$$\hat{C} = \begin{pmatrix} C_{1,1} \hat{\mathbb{1}}_k^j & C_{1,2} \hat{\mathbb{1}}_k^j \\ C_{2,1} \hat{\mathbb{1}}_k^j & C_{2,2} \hat{\mathbb{1}}_k^j \end{pmatrix}, \quad \hat{S} = \begin{pmatrix} \hat{S}_k^{j,\uparrow} & 0 \\ 0 & \hat{S}_k^{j,\downarrow} \end{pmatrix}, \quad \hat{F} = \begin{pmatrix} \hat{F}_k^j & 0 \\ 0 & \hat{F}_k^j \end{pmatrix}. \quad (5.13)$$

The accelerated walk operator can now also be written in the Fourier picture. The form of $\hat{W}_{\text{el},k}$ that acts on $\mathcal{H}_{\text{tot}} = \mathcal{H}_k^n \otimes \mathcal{H}_k^j \otimes \mathcal{H}_{\text{coin}}$ is given by

$$\hat{W}_{\text{el},k} = \hat{\mathbb{1}}_k^n \otimes \left[(\hat{F}_k^j \otimes \hat{\mathbb{1}}_{\text{coin}}) \cdot \hat{S}_k^{j,\text{spin}} \cdot (\hat{\mathbb{1}}_k^j \otimes \hat{C}) \right] = \hat{\mathbb{1}}_k^n \otimes \hat{W}_{\text{el},k}^{j,\text{spin}}, \quad (5.14)$$

meaning that the accelerated walk reduces to the product of the matrices defined in (5.13). Hence, the accelerated walk is sufficiently described by a $2m \times 2m$ matrix as well. The explicit expression of the reduced form yields

$$\hat{W}_{\text{el},k}^{j,\text{spin}} = \hat{C} \cdot \hat{S} \cdot \hat{F} = \begin{pmatrix} C_{1,1} \hat{S}_k^{j,\uparrow} \hat{F}_k^j & C_{1,2} \hat{S}_k^{j,\uparrow} \hat{F}_k^j \\ C_{2,1} \hat{S}_k^{j,\downarrow} \hat{F}_k^j & C_{2,2} \hat{S}_k^{j,\downarrow} \hat{F}_k^j \end{pmatrix} \quad (5.15)$$

Temporal regrouping

Instead of looking at the new spacial periodicity, one can also choose the temporal approach. The m^{th} power of the accelerated quantum walk operator (5.5), i.e. \hat{W}_{el}^m , is again translational invariant. Knowing that the force operator causes a shift in k by ϕ , it can be shown that the Fourier transformation of the defined translational invariant operator reads

$$\hat{W}_{\text{el},k}^m = \hat{W}_k(k + \phi) \cdot \hat{W}_k(k + 2\phi) \cdots \hat{W}_k(k + m\phi). \quad (5.20)$$

Recalling that $\hat{W}_k = \hat{\mathbb{1}}_k \otimes \hat{W}_k^{\text{spin}}$, the translational invariant operator $\hat{W}_{\text{el},k}^m$ is fully described by a 2×2 matrix according to (5.20). This allows to find the characteristic polynomial following the standard form of

$$\det \left[\hat{W}_{\text{el},k}^m - \Lambda \hat{\mathbb{1}} \right] = \det \left[\hat{W}_{\text{el},k}^m \right] - \Lambda \text{Tr} \left[\hat{W}_{\text{el},k}^m \right] + \Lambda^2 \quad (5.21)$$

Using (2.11), it can be shown that

$$\det \left[\hat{W}_{\text{el},k}^m \right] = \left(\det \hat{C} \right)^m = 1, \quad (5.22)$$

since $\hat{C} \in SU(2)$. So the eigensystem of (5.20) is purely determined by its trace. It can be proven⁴ that this trace generally simplifies depending on the parity of m to

$$\text{Tr} \left[\hat{W}_{\text{el},k}^m \right] = (-1)^{m+1} \left[\left(\hat{W}_{k(1,1)}^{\text{spin}} \right)^m + \left(\hat{W}_{k(2,2)}^{\text{spin}} \right)^m \right] + \Theta_m \quad (5.23)$$

$$\text{with} \quad \Theta_m = \begin{cases} 0 & m \text{ odd} \\ (-1)^{\frac{m}{2}+1} 2 \left[\left(\det \hat{C} \right)^{\frac{m}{2}} - \left(\hat{W}_{k(1,1)}^{\text{spin}} \hat{W}_{k(2,2)}^{\text{spin}} \right)^{\frac{m}{2}} \right] & m \text{ even} \end{cases}, \quad (5.24)$$

where again the definition of (2.11) has been used. By substituting this into (5.22) the eigenvalues can be determined. By specifying the coin in the same way as above, it can be confirmed that the form of the characteristic polynomial is identical to (5.17), i.e. the one found in the spatially regrouped case. Thus, both techniques lead to the same set of eigenvalues $\omega_{\pm,j}(m)$.

An additional strength of the temporal picture is a mathematical explanation for the revival. For this to happen after m steps in the even, and $2m$ steps in the odd case the corresponding total operator \hat{W}_{el}^m and \hat{W}_{el}^{2m} , respectively, should be close to the identity in operator norm, i.e.

$$0 \approx \begin{cases} \|\hat{W}_{\text{el}}^{2m} - \hat{\mathbb{1}}\|_{\text{op}} & \text{for } m \text{ odd} \\ \|\hat{W}_{\text{el}}^m - \hat{\mathbb{1}}\|_{\text{op}} & \text{for } m \text{ even} \end{cases}. \quad (5.25)$$

To make a quantitative estimate, the operator is to be replaced by its eigenvalue. Recall that $\Lambda_{\pm} = \lambda_{\pm}^m = e^{\pm im\omega} = e^{\pm i\epsilon}$, where ϵ is defined as in (5.19). For a sufficiently large value of m , the appearing arccos function can be approximated such that

$$\Lambda_{\text{odd}}^2 \approx \left[e^{\pm i(\frac{\pi}{2} - \cos(\epsilon))} \right]^2 \approx -1, \quad (5.26)$$

$$\Lambda_{\text{even}} \approx e^{\pm i \arccos(1)} \approx 1, \quad (5.27)$$

⁴To be published by Prof. R.F. Werner's group (Institut für Theoretische Physik, Leibniz Universität Hannover)

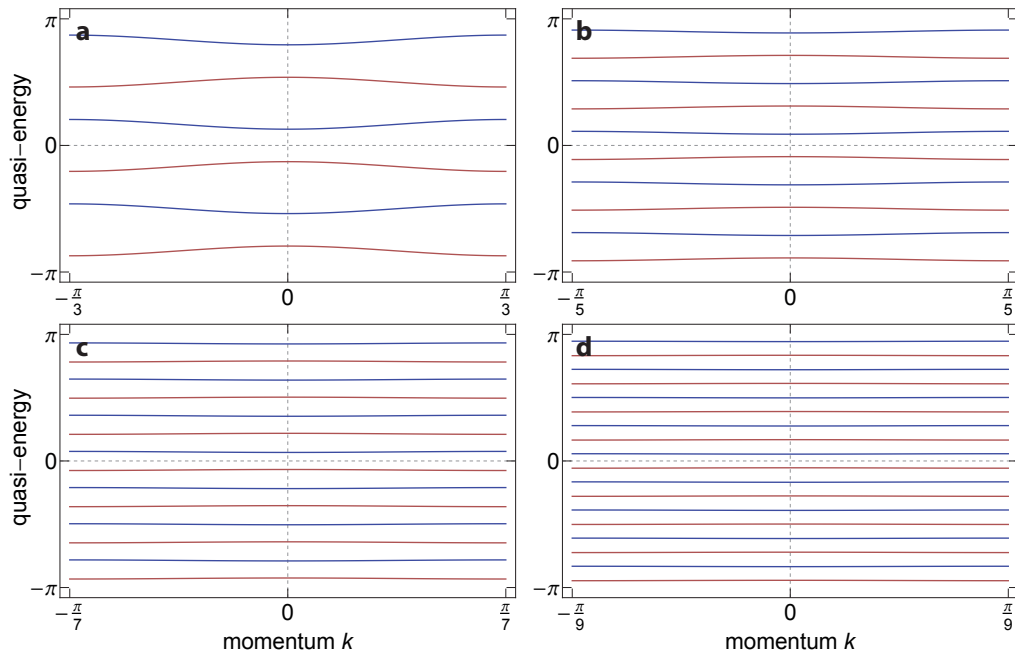


Figure 5.5.: Quasi-energy bands of an electric quantum walk \hat{W}_{el} for an experimental Hadamard coin as defined in the text and different force parameters $m = 3$ (a), 5 (b), 7 (c) and 9 (d). Increasing m reduces the Brillouin zone, increases the number of bands accordingly and lets the bands approach a Wannier-Stark ladder configuration. The flattening of the bands reflects the slower asymptotic ballistic transport.

since $|\cos(\epsilon)| \rightarrow 0$ in the odd and $|\cos(\epsilon)| \rightarrow 1$ in the even case, respectively. Because the minus sign in the odd case is undetectable, the expectation of (5.25) indeed holds true. Hence, it is shown that good revival occurs for m in the even and $2m$ in the odd case. In fact, since the approximation applied in (5.27) holds firmer for larger values of m , the revival is expected to be better for smaller forces. Moreover, the small deviation from the identity adds up after every period causing the revival to become worse for higher step numbers. This supports what has already been shown above.

To continue with an analysis of the asymptotic behaviour of the system, the eigenvalues $\omega_{\pm,j}(m)$ are now plotted as a function of k to reveal the dispersion relations. Figure 5.5 shows these for different force realisations, and an angle set to $\theta = \frac{\pi}{2}$, i.e. an experimental Hadamard coin. As it was the case for the non accelerated quantum walk, the mere existence of these bands gives rise to the ballistic expansion of the system. The changing shapes of the bands then asymptotically explain the lower expansion velocity, and hence the better refocussing, of the system for smaller forces: From figure 5.5 it can be seen that with increasing m -values the bands start to flatten out rather rapidly. This directly translates into a decrease of the corresponding group velocities according to $v_g = \frac{\partial \omega}{\partial k}$, and ultimately, leads to localisation. For these cases, the system is believed to adiabatically follow the bands, hence suppressing Landau-Zener tunnelling and mimicking a continuous time system that is exposed to a weak force. In the latter case the localisation effect of quantum particles is also described by flat bands. The arrangement of those is known as the so-called Wannier-Stark ladder [25].

Looking closer at the bands one can further show that forces with m and $2m$ must reveal the same asymptotic behaviour if m is odd. In figure 5.6 the dispersion relations for the specific cases of $m = 3$ and $m = 6$ are plotted. It can be seen that the bands

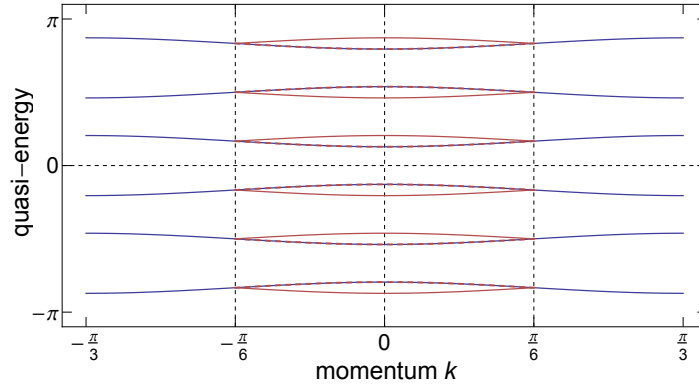


Figure 5.6.: Dispersion relations of two accelerated quantum walk systems for force parameters $m = 3$ (blue), 6 (red). It can be seen that corresponding bands perfectly overlap. As the Brillouin zone is exactly halved for $m = 6$ the bands are folded accordingly.

fully overlap. Since the doubling of m halves the Brillouin zone, the bands are forced to fold into the designated area, still describing the dynamics. By considering (5.18) and (5.19) this equivalence can also be demonstrated analytically. Alternatively, one can focus on the corresponding group velocities $v_g = \partial\omega/\partial k$, where the same property should be seen. In fact, by looking at v_g^2 the non-differentiability at the edges of the Brillouin zone can be removed. Explicit formulas are obtained for

$$\text{odd } m \quad \left(\frac{\partial\omega(m)}{\partial k} \right)^2 = \frac{\cos^{2m}(\frac{\theta}{2}) \sin^2(mk)}{1 - \cos^{2m}(\frac{\theta}{2}) \cos^2(mk)} , \quad (5.28)$$

$$\text{even } m \quad \left(\frac{\partial\omega(m)}{\partial k} \right)^2 = \begin{cases} \frac{\cos^m(\frac{\theta}{2}) \sin^2(\frac{mk}{2})}{1 - \cos^m(\frac{\theta}{2}) \cos^2(\frac{mk}{2})} & \text{for } \frac{m}{2} \text{ odd} \\ \frac{-\cos^m(\frac{\theta}{2}) \sin^2(\frac{mk}{2})}{1 + \cos^m(\frac{\theta}{2}) \cos^2(\frac{mk}{2})} & \text{for } \frac{m}{2} \text{ even} \end{cases} . \quad (5.29)$$

Hence, it is easily seen that

$$\left(\frac{\partial\omega(2m)}{\partial k} \right)^2 = \left(\frac{\partial\omega(m)}{\partial k} \right)^2 \quad \text{for } m \text{ odd} . \quad (5.30)$$

This result confirms that both cases present the same asymptotic dynamics. Furthermore, by using (5.28) and (5.29) one can find the maximum velocity of the system to be

$$|v_g^{\max}| = \cos^m(\theta/2) . \quad (5.31)$$

The impact of changing the angle θ can again be understood as a closing or opening mechanism, respectively, of the band gaps in figure 5.5 (c.f. section 2.2). Consequently, also the bands' curvature gets altered, thus influencing the maximal velocity according to (5.31). This is equivalent to a statement about changing the probability of Landau-Zener tunnelling to occur. It should be noted that (5.31) is highly non-linear for large values of m , i.e. a slight change in θ will have a considerable impact on the dynamics of the accelerated quantum walk.

5.2. Experimental realisation

While the achievement of ordinary quantum walks (chapter 4) required only the experimental tools of coherent internal state manipulation (section 3.2) and spin-dependent transport (section 3.3), the electric version additionally exploits the possible lattice acceleration by means of the home-built DDS box (section 3.4). The precise and flexible way of controlling the output frequencies allows to execute the force operation in a textbook fashion as in (5.4). Further, it can be numerically shown that the experimental operator $\hat{W}_{\text{el,exp}}$, which is analogously defined to \hat{W}_{exp} , i.e.

$$\hat{W}_{\text{el,exp}} = \left[\hat{F} \cdot \hat{S}_{\rightleftharpoons} \cdot (\hat{\mathbb{1}}_{\text{space}} \otimes \hat{C}) \cdot \hat{F} \cdot \hat{S}_{\rightleftharpoons} \cdot (\hat{\mathbb{1}}_{\text{space}} \otimes \hat{C}) \right], \quad (5.32)$$

produces the same results as the theoretical one \hat{W}_{el} applied twice for an initially chosen spin-up state⁵. So a distinguishable effect due to the alternating shift operation as seen for the ordinary quantum walk is not expected here.

5.2.1. Procedure

The general procedure of an accelerated or electric quantum walk (EQW) is exactly the same as for the walk without a force present. Thus, all experimental details stated and described in chapter 4 also apply here. In contrast to the ordinary quantum walk, though, the initial spin configuration is steadily chosen to be $|s_0\rangle = |\uparrow\rangle$, which removes the possible error on the state preparation. This is believed to be particularly advantageous here, because the effect on the spatial distribution is not as clearly to distil as for the ordinary quantum walk, where it manifests itself in an imbalance of the distribution. But the major difference of this experimental sequence is, of course, the implementation of the additional force operation. As defined in (5.5), this occurs in a discrete fashion in every cycle of a single EQW step. Figure 5.7 shows schematically the layout of the actual main sequence. The force, i.e. the corresponding frequency ramp, is exerted upon a trigger received from a waveform generator (similar to triggering the other two operations). The length of an acceleration period τ_{acc} was set to $12.5\mu\text{s}$ due to an expected minimum of the vibrational state excitation (c.f. 3.4.3). Since the acceleration only affects the position degree of freedom, i.e. lets the spin-state untouched, consecutive force- and coin-operations can actually be performed simultaneously in favour of keeping the sequence length at a minimum. Thus, the length of a single EQW step is the same as for an ordinary experimental quantum walk step, i.e. $\sim 45\mu\text{s}$ (recall that $\tau_{\text{acc}} < \tau_{3\pi/2}$).

All necessary parameters characterising the strength of the force are already transferred to the microcontroller before the actual experimental sequence is run. In general, it is desired to express also the experimental system in terms of the unit-less force parameter m . However, the DDS box needs to work with physical quantities, eventually. Using (5.3) the conversion yields

$$m = \frac{2\pi \hbar}{F d \tau_{\text{acc}}} = \frac{16\pi \hbar}{M_{\text{cs}} \lambda^2 \Delta\nu}, \quad (5.33)$$

where M_{cs} is the mass of a Caesium atom, λ is the Ti:Sa wavelength and $\Delta\nu$ denotes the final detuning after a single linear frequency ramp. Note again that d is not the

⁵This statement does not hold for a complex superposition state such as $\frac{1}{\sqrt{2}}(|\uparrow\rangle + i|\downarrow\rangle)$. Contrary to the ordinary quantum walk, here, the possibly complex entries of the force operator matrix cause interferences of both initial parts in the course of the accelerated walk.

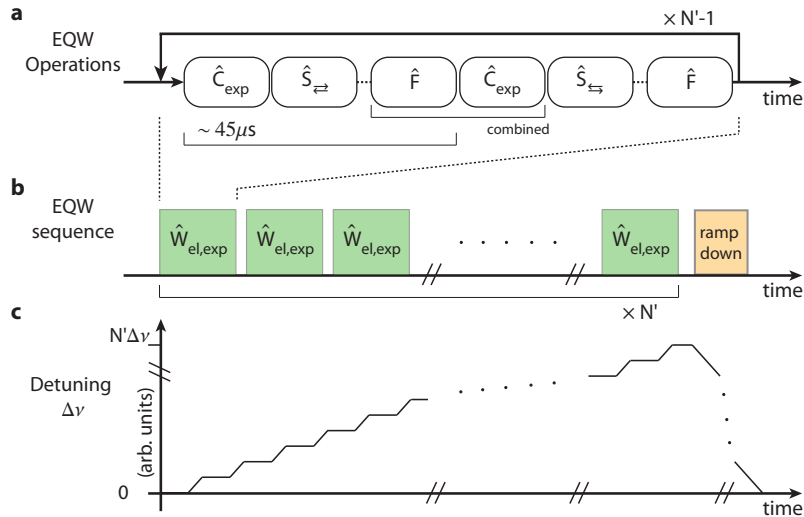


Figure 5.7.: Schematics of an experimental sequence that realises electric quantum walks. The consecutive application of operations and their decomposition into blocks is given in (a) and (b). The behaviour of the total detuning of both lattice arms is given in (c).

real lattice spacing here, but rather the spatial separation between two neighbouring positions before and after an EOM shift operation, i.e. $\sigma/4$. It shall be noted that the limited frequency resolution of the DDS causes a small rounding error when converting the desired m into detuning units. This effect is usually in the sub-percent range, and thus can be neglected. So when employing a linear frequency ramp, the only quantity determining the phase accumulation is the final detuning. However, this immediately lets a problem become apparent: after every acceleration the two laser beams have a non-zero detuning, leading to a constant velocity. This imposes additional dynamics onto the lattice that need to be taken into account when analysing the taken images. It also complicates the necessary behaviour of the detuning over the range of the entire EQW sequence. In the following the associated behaviour of the DDS is outlined in detail.

Frequency ramp As explained in section 3.4.2 the linear sweep mode of the DDS is employed to drive the frequency ramps. The device is programmed such that upon a received trigger it ramps up to a predefined end-frequency and dwells at this value. But this works only for a single step. Since returning to the initial frequency is not possible as the relative phase accumulation would be reversed, the subsequent step requires a ramping to a higher frequency. To ensure the same operation as before, the relative detunings need to be identical. So every step of the sequence adds an additional detuning of $\Delta\nu$ (figure 5.7(c)). The DDS box allows this shape of frequency ramp nicely by its internal functions. It is assumed that the DDS dwells at its programmed end-frequency. Changing this frequency to a higher value, instantly forces the DDS to continue the ramp with identical parameters as before, and crucially in a phase continuous fashion. Hence, the desired ramp shape is achieved by reprogramming the end-frequency after every step. In fact, the microcontroller is programmed such that the DDS receives the corresponding frequency word for the next cycle already when performing the current ramp. The information, however, is only written into the internal buffer, and thus will not be executed until the next trigger. This ensures that the communication delay between the mbed microcontroller and DDS board is eliminated. The only remaining time

lag is then the internal handling of the 32-bit frequency tuning word. Recalling that the fundamental processing time of a single bit is 10 ns, one would assume a remaining delay of about 300 ns, and this is indeed what can be experimentally confirmed. Because this is well below the experiment control's $2\mu\text{s}$ time resolution, no further attention has to be paid to this. By performing the whole frequency ramp as shown in figure 5.7, a considerable total detuning $N'\Delta\nu$ can be picked up at the end of a sequence, depending on the sequence's length and the defined force strength. The associated velocity of the entire system makes it impossible to determine the position with single-site resolution (c.f. smearing effect in figure 3.8). In order to ultimately end up in a static situation, the DDS automatically receives an additional command which changes the direction of the ramp after the actual sequence. Now, the DDS ramps the output frequency from the final value back down to its initial value. The frequency gradient is the same as for the ascending ramps. Once the 80 MHz are recovered, the lattice is static again, and correct imaging of the atoms is possible. Evidently, the initial position of the atom has shifted because of the acceleration process. In order to identify the atoms properly and to interpret their measured positions accurately, this shift has to be known to a precision below the single site resolution limit. For this purpose, a preliminary measurement testing the end position is usually performed. In this test the atom is treated as a scalar particle, and no coin- or shift operations are applied, while the timing sequence is the same as in the actual sequence. The determined final position is then later used to recalibrate every second picture. This, however, can only work as long as the travelling distance is still considerably smaller than the width of the imaging window. For too long sequence lengths or very strong forces, respectively, the atoms start to leave the imaging region, and the presented method is inapplicable. A way around this problem is to run the same frequency ramp a second time after the lattice has come to a halt, but on the other frequency channel. This inverts the effect of movement, and brings the lattice back to its initial position. This opens the door for sequences implementing sensible force strengths, which are only limited by the coherence times of the system.

5.2.2. Results

Testing the phase imprint

Before the acceleration operation is implemented in the sequence as outlined above, it shall be experimentally demonstrated that it indeed gives rise to the intended relative phase accumulation. Generally, the best way to detect phases is an interferometer. So by performing an atom-interferometer measurement [1, 10], one is capable of detecting the induced phase. For this, a simple two-step interferometer is realised. This leads to a spatial separation of two lattice site, i.e. λ , of the two coherent atom parts. The force parameter m gives the relative phase of $\phi = \frac{2\pi}{m}$ over a distance of $\lambda/4$. Thus, applying the force operation after the atom has been separated results in a total relative phase accumulation of $\Phi = 4\phi$. For a multiple consecutive application of the force of n times, the total phase difference is given by $n\Phi$. A subsequent closing of the interferometer, followed by a final $\frac{\pi}{2}$ -pulse results in an effective Ramsey sequence and allows for probing the accumulated relative phase of both atom parts, which is given by the measured phase of the Ramsey fringe.

Putting the force parameter exemplarily to $m = 20$, the expected phase to be gathered becomes $\Phi = \frac{2\pi}{5}$. The corresponding detuning per step is about $\Delta\nu = 1.6\text{ kHz}$. Figure 3.9 reveals that excitation processes for such detunings can be generally neglected. Figure 5.8 shows the measured Ramsey phase for different application num-

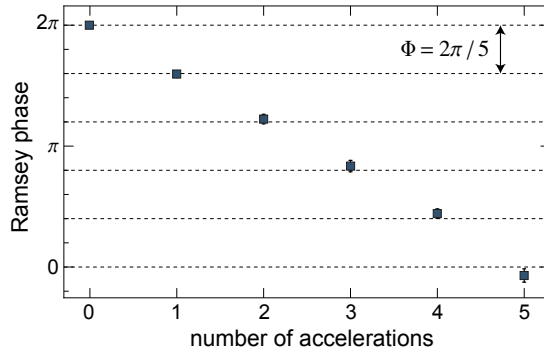


Figure 5.8.: Measured Ramsey phase of a 2-step atom interferometer measurement for an intended phase imprint of $\Phi = \frac{2\pi}{5}$ per acceleration.

bers n . Individual acceleration ramps are separated by an idle time of about $25\mu\text{s}$. Moreover, π -pulses are applied to compensate for inhomogeneous dephasing effects. It can be observed that the measured data follows very nicely the expectations. Additionally, the contrast of the individual Ramsey fringes is unaltered by the acceleration operations. By this, confirmation is gained that not only a single acceleration process, but also a consecutive repetition of such produces indeed a *coherent* phase imprint, and hence proving the desired functionality of the DDS. All pieces are finally gathered to perform electric quantum walks.

Even force parameter

Proceeding as outlined in section 5.2.1 allows to experimentally investigate quantum walks in the presence of a discretised force as defined in (5.5). Two explicit examples of an even force parameter m shall be presented and discussed in detail. The strengths were chosen to be $m = 8$ and $m = 20$, respectively. Figure 5.9 shows the measured results for these two realisations. Just as for ordinary quantum walks (chapter 4) the amount of contributing individual atoms is about 200, and the errors are calculated and propagated by the same means as before. In order to determine the correct coin angle as well as the decoherence level, a set of ordinary quantum walks were taken prior to the actual sequence. With these, η and p could be calibrated as described in section 4.4.

First, the $m = 8$ case shall be at the focus of interest. For this particular force parameter the frequency of dipole trap arm one (DT1) was detuned by about 4 kHz per acceleration step (see (5.33)). Driving up to this detuning in $12.5\mu\text{s}$ causes a constant acceleration strength of $\sim 14\text{g}$. Calculating the actual value of m taking the software rounding error into account yields $m = 7.9993$, and hence the integer assumption is sufficient here. By analysing first the preliminary data of an ordinary quantum walk, coin correction factor and decoherence level were determined to be $\eta = 0.98 \pm 0.01$ and $p = 0.07 \pm 0.01$, respectively. Then, walk sequences with integrated acceleration steps were performed for 4, 8, 12 and 16 steps. The corresponding probability distributions can be observed in figure 5.9(a)-(d). Following the theoretical considerations, an oscillation should occur with a periodicity of 8. The revival is damped owing to decoherence processes, but is clearly visible by looking at the experimental data. The second expected contraction after 16 steps, however, is not very distinct any more. Qualitatively, the taken data for all steps follow quite accurately the expectations made by the employed spin-decoherence model. Hereby, the simulation of Bloch oscillations in quantum

walks is successfully confirmed. The same effect should also manifest itself in the associated RMS value. However, when looking at figure 5.9(e) the data points do not show a strong sign of oscillation. It is indeed revealed that the walk's spatial spreading is hampered in the presence of a force, but it seems that in this picture the measurements might also be described sufficiently well by the classical model. Having said this, up to 12 steps the recorded data agrees within its error bars with the expectation taking decoherence into account. Nonetheless, while the RMS picture is suitable to describe the dynamics of an ordinary quantum walk, it is not necessarily advantageous to use it here. Instead one shall solely focus on the remarkable feature of the revival. A full and ideal revival will yield the system with almost unity probability at the initial spatial position $|n_0\rangle = |0\rangle$. Figure 5.9(f) gives the probability $P_{\{0\}}$ with which the system could be found at $|0\rangle$ as a function of the step size. While the curves for the classical diffusion as well as for the ordinary quantum walk decrease rapidly, the predicted revivals cause peaks. Although theoretical predictions are not fully matched, the contraction of the system's wave function to the initial state can be clearly observed for 8 steps.

In the other presented example a weaker force of $m = 20$ was exerted, which corresponds to a detuning per step of $\Delta\nu = 1.6$ kHz and an acceleration of about 5.5 g. The rounding leads to an effective m of 19.94, which is still below one percent deviation from the ideal value. For this set of measurements a coin correction of $\eta = 0.98 \pm 0.01$ and a slightly unusual high decoherence level of $p = 0.10 \pm 0.01$ was found. Due to an expected oscillation period of 20, the step size was varied from 10 to about 30. Selected probability distributions can be found in figure 5.9(g)-(j) for step numbers of 14, 18, 20 and 24. It can be nicely observed how the delocalised distribution contracts and subsequently spreads again. Decoherences again smear out this effect to a certain extend. But as in the previous case, the theoretical decoherence curve describes the measured data qualitatively very well. Moreover, the movement of the wave packet across the revival can be inferred. Theoretical predictions showed (c.f. figure 5.2) how for an initial spin-up state the electric walk, or rather its mean position, maintains its moving direction at all times. So the distribution's "center of mass" is expected to move across the zero position when varying the step size across the value where the revival is to occur. Exactly this effect is beautifully revealed by the shown data, illustrating that not only the feature of revival is experimentally demonstrated, but also additional dynamical properties. In the RMS picture this spatially directional behaviour can de facto not be observed, but even the general contraction of the electric walk is washed out (see figure 5.9(k)). This holds for the experimental data, but also the theoretical decoherence curve loses almost all signs of periodic motion for $p = 0.10$. Though the data points do show hints for an oscillation, it is not enough to sufficiently distinguish these from the pure classical curve. Similar to what was done above, the focus will be on the zero-position probability instead. In fact, since here larger steps sizes are involved, which potentially leads to a wider spreading of the walk, the accumulated probability over the set⁶ $\{-2, 0, 2\}$ is considered, i.e.

$$P_{\{-2,0,2\}} = \sum_{n=\{-2,0,2\}} P_{|n\rangle} = \sum_{n=\{-2,0,2\}} |\langle n|\psi_N\rangle_{\text{el}}|^2. \quad (5.34)$$

The summed probability (5.34) is depicted in figure 5.9(l). While the curve describing ideal theoretical predictions shows a clean oscillation ranging up to unity probability, the one respecting decoherence has a significantly lowered amplitude. Nonetheless, the oscillating behaviour can be impeccably attributed. Experimental data agrees mostly

⁶Recall that for even step sizes odd position states are unoccupied

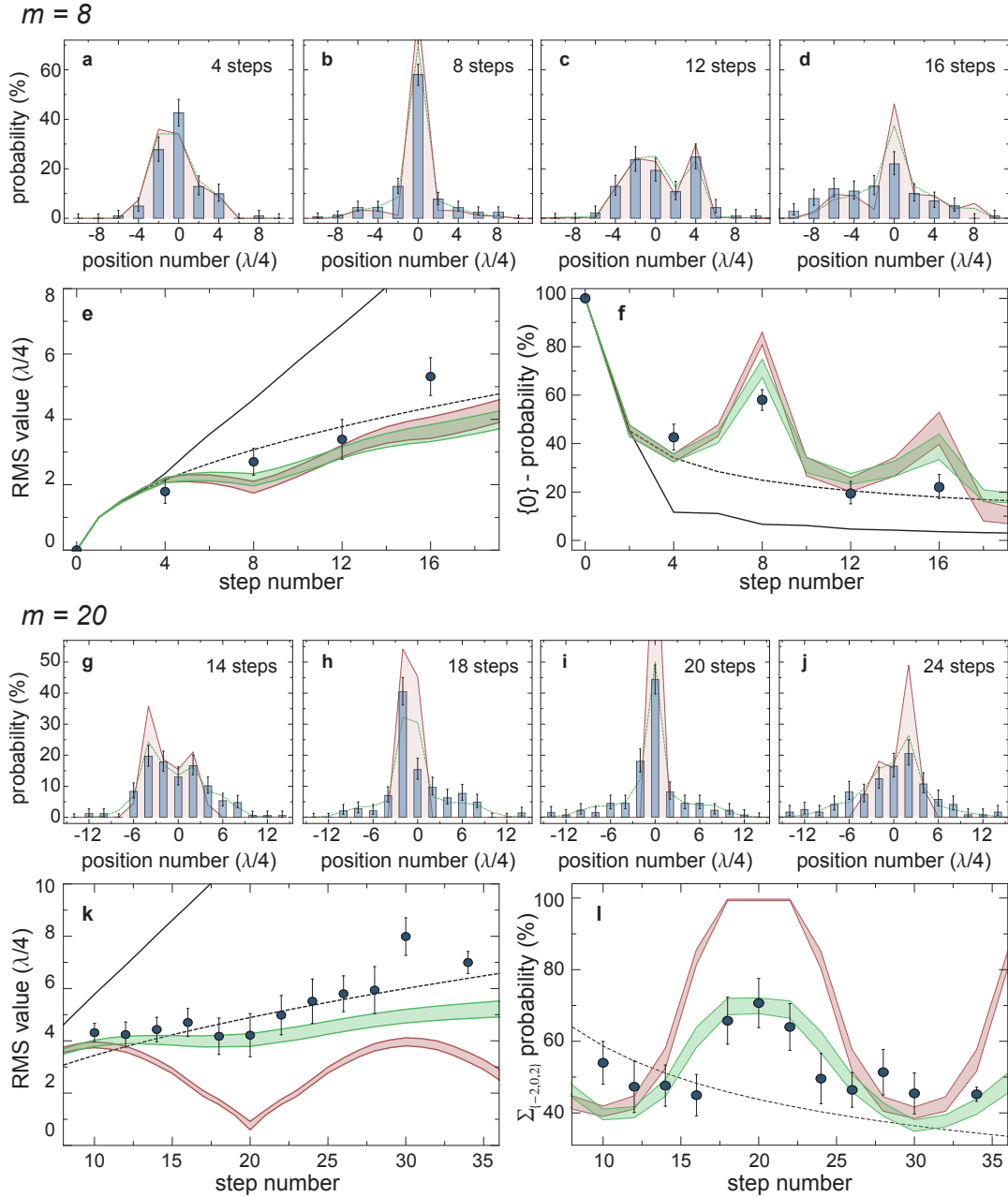


Figure 5.9.: Experimental accelerated quantum walks for $m = 8$ and $m = 20$, respectively. All measured distributions are given in (a)-(d) for the first, and a selection of such in (g)-(j) for the second case. The corresponding root mean square values are plotted in (e) and (k), respectively. The real coin parameter was determined for both cases to be $\eta = 0.98 \pm 0.01$. The decoherence level is estimated to be $p = 0.07 \pm 0.01$ for $m = 8$ and $p = 0.10 \pm 0.01$ for $m = 20$. While for $m = 6$ the zero-position probability is depicted as a function of the step number in (f), the same is done for the accumulated probability over the $\{-2, 0, 2\}$ -positions in the $m = 20$ case (l). Ideal theoretical curves is generally plotted in red and ones respecting decoherence in green. An ordinary quantum walk is represented by a black solid line, and its classical counterpart by a dashed one. For detailed description and analysis see text.

with this curve, particularly within the region of expected revival. This gives additional prove that also for this weaker force, and associated longer walking sequences than above, the effect of an electric field on a charged quantum particle could have been simulated.

Having said this, negative effects and their impacts need to be discussed, particularly with regard to the quality of the RMS plots. Whereas for ordinary walks, which show in any case a spatially wider distribution, a miscount does not significantly impact the RMS value, the electric version is highly sensitive to such bad events. Particularly around the revival case, i.e. where the RMS approaches zero for full contraction, unwanted events disturb the outcome tremendously. Here, an unnoticed drop of the single-site resolution efficiency due to a small drift of the objective position, for example, could have a huge impact. Furthermore, when enlarging the number of steps, the experimental radius of interest becomes larger as well. This increases the probability of unwanted recordings such as rare cases of hopping atoms, which imprints an additional offset onto the RMS curve. Such an offset can indeed be seen by looking at figure 5.9(k), for example. But even in the case of model-like decoherence, the oscillatory effect washes out rather swiftly in the RMS picture. It has been presumed that the additional force operation does not induce further decoherence. However, this assumption might not be fully correct, leading to an additional reduction of the RMS oscillation, and poorer data quality in general. Particularly longer sequences could be further negatively affected, if the value of total detuning might start to significantly change the AOM diffraction properties. An altered trap depth would be the consequence leading to additional undesired effects. Generally, increasing the length of the sequence increases also the relevance of decoherence, making it even more difficult to properly show the asymptotic behaviour of a quantum walk experiencing acceleration. A possible additional effect that has been neglected so far is the intrinsic shape of the lattice. Locally, the potential is perfectly well described by a sinusoidal form, but the real shape is that of a Gaussian beam. This leads to an inevitable potential gradient across the lattice [10]. While for ordinary quantum walk sequences of moderate step sizes this is believed to be negligible, here, the additional movement along the lattice axis (particularly for strong forces, and long sequences) might let the system explore this extra effective force. The consequence would be additional interference processes, which could give rise to a reduction of the revival. A quantitative analysis of this is not performed, though. In conclusion, while the decoherence model describes the measured probability distributions very well and results here mainly in quantitative discrepancies, the presentation in the RMS picture suffers severely from decoherences and other unwanted effects also in a qualitative fashion. Nonetheless, the occurrence of revivals, and hence the simulated phenomenon of Bloch oscillations could be demonstrated.

Pure ballistic transport in the strong force regime

Section 5.1.4 has intuitively described how the demonstrated effect of the applied force is removed in two cases of the strong regime by tuning m correctly. For the values $m = 1, 2$ the momentum translation and the associated mapping to the energy bands should give rise to the same dynamics as $m = \infty$, i.e. where no force is present at all. Figure 5.10 shows the experimental investigation of the phenomenon.

The paramters $m = \{1, 2\}$ correspond to a per-step detuning of $\Delta\nu = \{32, 16\}$ kHz and an associated acceleration strength of $a = \{82, 41\}$ g. Note that even these strong⁷

⁷Here, the *strong* force regime is referred to the situation where $\frac{2\pi}{m}$ approaches 2π .

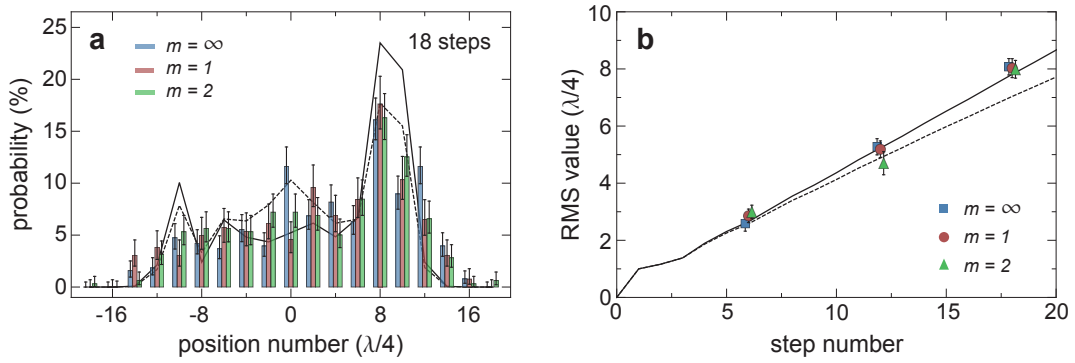


Figure 5.10.: Electric quantum walks for $m = \infty, 1, 2$. In (a) the probability distributions of all three cases are compared to each other for the exemplary case of an 18-steps walk. Coin correction factor $\eta = 1.07$ leads to the ideal theoretical curve (solid) and estimated coherence level of $p = 0.05$ corrects this (dashed). The RMS value of three different walk lengths are shown in (b). Here, for reasons of visibility the data points have been horizontally shifted relative to each other and the expectations are plotted without their confidence interval.

forces can be comfortably sustained by the system (c.f. figure 3.9). First, looking at the individual probability distributions for $m = \infty$ the coin correction factor and the decoherence parameter could be determined to be $\eta = 1.07 \pm 0.01$ and $p = 0.05 \pm 0.01$, respectively. The corresponding theoretical curves can then be compared to the experimental data. Figure 5.10(a) exemplarily shows the probability distributions of all three m realisations for a 18-steps accelerated quantum walk. Comparing these to each other reveals that they all follow the same shape. The discrepancies between data and theory regarding the peaks is again well explained by the decoherence model. However, the shown probability distributions for $m = 1, 2$ suggest that p might have been overestimated, since here the characteristic feature of an emerging center peak is absent.

Figure 5.10(b) gives the RMS picture for walks of different step lengths. The equivalent behaviour of this dynamical property for all three cases becomes apparent. In fact, the RMS values of a respective walk length fully agree to each other within their error bars. Moreover, it can be observed that all data points rather follow the ideal curve (solid) than the one taking decoherence into account (dashed). This can be explained by an overestimation of the decoherence together with the uncertainty in the coin correction factor η . Nevertheless, this is a mutual effect and does not alter the conclusion of the measurement: It could be experimentally shown that an applied strong force according to $m = \{1, 2\}$ indeed produces the same result as in the $m = \infty$ case, where the system is not subject to a force at all. Consequently, the theoretical considerations from section 5.1.4 can hereby be confirmed.

Hints for odd-even equivalence

Theory predicts that the asymptotic behaviour of electric quantum walks for odd values of m is the same as for even values of $2m$. Experimentally, this is very challenging to confirm since a) the step sizes are limited due to the present decoherence (so pure asymptotic testing is not possible at all at the moment) and b) the quantity of interest to show collective dynamics of the walk is the root-mean-square value. It is already shown above that this way of presenting the data might not be sufficient for proving

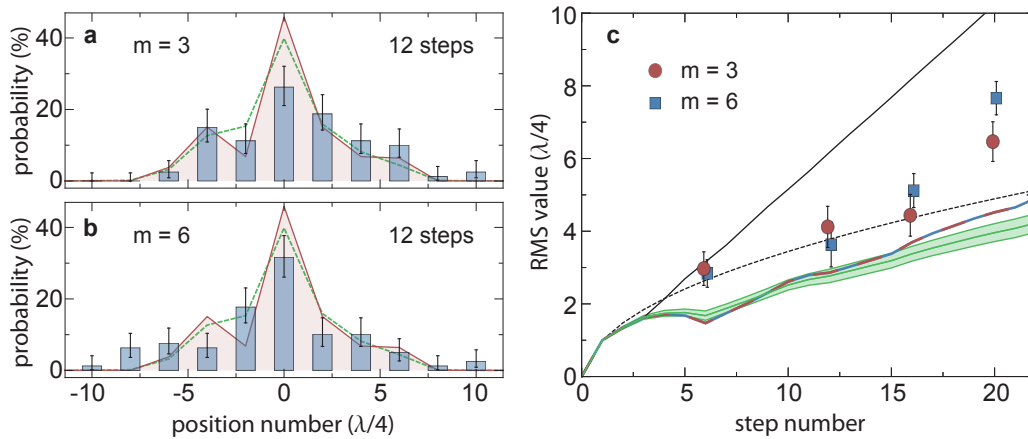


Figure 5.11.: Comparison of two electric quantum walks for $m = \{3, 6\}$. Measured probability distributions are shown in (a) and (b) for a walk length of 12 steps. The corresponding RMS values are depicted in (c). Here, only the decoherence curve ($p = 0.10 \pm 0.01$) is plotted with its confidence interval for reasons of visibility. The ideal theory for $\eta = 1.02$ is represented by a solid line (red-blue).

the desired effects. Nevertheless, an attempt to see the remarkable phenomenon has been undertaken. In order to keep the necessary step sizes at small values the two force parameters $m = 3$ and $m = 6$ were chosen. It can be numerically observed that these two cases do not only show identical asymptotic behaviour, but give equivalent results. This simplifies the situation since a direct comparison of the probability distributions is possible.

Figure 5.11(a)-(b) shows a pair of these distributions for a 12-step walk. Coin correction factor and decoherence level were here determined to be $\eta = 1.02 \pm 0.01$ and $p = 0.10 \pm 0.01$. It can be observed that the distributions show very similar characteristics. Even when going to the RMS picture (figure 5.11(c)), it can be seen that the corresponding values strongly agree with each other. However, huge deviations can be noticed, if these are compared to the decoherence curve. Possible reasons are already discussed above. So although the measured data does show some similarity between the two cases, the quality of the measured second moment is not sufficient to fully support what has been shown theoretically. A different approach to this problem might be to consider weaker forces and compare solely the revival strengths. This was not doable in the present case, since the strength of the respective forces causes strong Landau-Zener tunnelling that suppresses good revivals after just one period.

Towards incommensurate forces

So far, electric quantum walks have been investigated theoretically as well as experimentally under the assumption that the force parameter m is an integer number. But what happens if m is to become incommensurate? This is a very interesting and non-trivial case to study from the theoretical side, since the lack of periodicity in this system prohibits to apply the trick of regrouping as used in section 5.1. Numerically, however, the electrified walk operator (5.5) is applied as before⁸. It can then be shown that the behaviour of the resulting walk depends on the type of the irrational number, but shows extreme localisation in certain cases. One of such cases is where the force parameter is

⁸Having said this, no real computer is able to realise pure irrational numbers, but it is assumed that such a machine can approximate it sufficiently well.

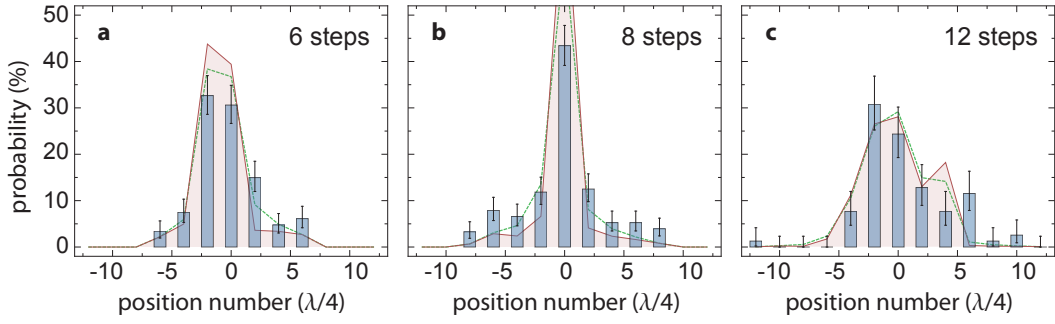


Figure 5.12.: Probability distributions of an accelerated quantum walk with $m = \frac{1+\sqrt{5}}{2}$ for (a) 6, (b) 8 and (c) 12 steps. Corresponding characterisation are $\eta = 0.98 \pm 0.01$ and $p = 0.10 \pm 0.01$. As usual, red shows ideal theoretical and green decoherence curve.

chosen to be $m = \frac{1+\sqrt{5}}{2}$ (~ 1.6180), i.e. the *golden ratio*. Performing a simulation for a quantum walk of 1000 steps reveals a very strong and steady spatial confinement, in which the RMS-value never exceeds 3. This occurs despite the fact that the system experiences a very strong force.

Figure 5.12 shows probability distributions of an experimental electric quantum walk implementing $m = \frac{1+\sqrt{5}}{2}$ for different step sizes. Calibrated quantum walk parameters are here $\eta = 0.98 \pm 0.01$ and $p = 0.10 \pm 0.01$, respectively. The internal software rounding processes result in an effective force parameter of $m = 1.6174$ which can be approximated by the rational fraction 1543/954. Although the irrational nature is lost, the numerical deviation for the pure golden ratio is hereby only around 0.04%. A numerical analysis of the two slightly different values of m for a realistic experimental sequence length of 100 steps reveals no noticeable mismatch between the ideal golden ratio and the experimentally applied one. Indeed, it can be observed that the recorded probability distributions in figure 5.12(a)-(c) follow rather well the theory curves, which assume an ideal golden ratio as the parameter m . The discussed sensitivity of the electric walk, its quality regarding the corresponding RMS value as well as the generally limited number of steps prevent the analysis of the remarkable feature of strong and permanent confinement, though. Nonetheless, it seems that incommensurate force parameters can be approximated sufficiently, and hence their effect on the quantum walk can in principle be tested. The investigation of phenomena related to such type of numbers, for example the difference between individual irrational values of m , is therefore suggested. Having said this, further improvement of the presented system is essential such that the testing of asymptotic behaviour can be accomplished.

Chapter 6.

Conclusion and Outlook

So far, quantum walks with single caesium atoms were strongly limited with respect to step sizes. The accumulated effects of decoherence resulted in strong non-quantum signatures already after about 20 steps. In the course of this thesis, however, quantum walks of up to 100 steps maintaining firm signs of quantum coherences could be successfully demonstrated. By carefully improving all experimental aspects as well as employing a shallower optical trap during sequences, these results could be achieved. In addition, the application of a spin-decoherence model allowed to accurately explain the discrepancies between recorded data and theoretical expectations. The level of decoherence had to be individually found by fitting the model to the data. The determination of a direct connection between model parameters and experimentally measurable quantities is proposed as a future task.

Furthermore, the quantum walk was investigated with respect to its dynamical properties. Theoretical considerations reveal that the quantum walk is asymptotically governed by an effective energy band structure. The properties of these bands strongly depend on the form of the coin operation. Appropriate adjustment of the applied microwave radiation field, allowed for systematic testing of this relation. Here, measurements indeed fully agree with the theory, revealing the quantum simulator properties of the quantum walk system.

Embarking on this theoretically, the quantum transport behaviour of quantum walks was further studied by applying a discrete force operator on the system. Since this process resembles the evolution of a charged quantum particle under the presence of an electric field, such a walk system is named *electric quantum walk*. In order to test the remarkable properties of this time discrete system experimentally, within this thesis a method has been implemented that allows to exert forces on a single atom system in a one-dimensional optical trap. Hereby, the entire lattice is accelerated by appropriate relative detuning of the two lattice arms, which is achieved by a direct digital synthesizer to a very high level of reliability.

Internal functions of the DDS device offer the opportunity to employ also discrete force operations on trapped system. Extending the typical experimental quantum walk sequence by this action lead to the realisation of electric quantum walks. Accompanied by theoretical predictions, electric walks were recorded for a set of chosen forces. It could be successfully demonstrated that the walk's probability distribution reveals spatial contractions for the tested force parameters $m = 8, 20$, hereby effectively simulating the phenomenon of *Bloch oscillations*. Additionally, it could be experimentally illustrated how the effect of the force is eliminated by setting the force parameter to $m = 1, 2$, respectively. This phenomenon is theoretically linked to the occurrence of pure Landau-Zener tunnelling for these respective forces. Moreover, the theoretical model demonstrates the asymptotic equivalence of electric walks for forces corresponding to an odd value of m and its even counterpart $2m$. Although this could not be fully confirmed, experimental hints were shown. In a last step, approximations of incom-

mensurate forces and their impact on electric walks were considered. Here, experimental limitations prevented to reveal the expected strong confinement properties of such a walk.

The general limiting factor of all experimental sequences was the coherence time of the system. Whereas for ordinary quantum walks this can be sufficiently compensated with the applied decoherence model, the investigation of an electric quantum walk, particularly regarding its asymptotic behaviour, is very demanding with respect to experimental optimisation. Here, the quantum effects get rapidly washed out by the presence of decoherence. Hence, it is suggested to attempt boosting the coherence time by the exchange of technological devices. In this context the most promising approach is to replace the EOM. By establishing longer coherence times, it is believed that further testing of the remarkable asymptotic behaviour of electric walks should become possible. Hereby, further simulations of potentially complex systems could be achieved by this time discrete system [20].

On top of that, the preparation of momentum states would experimentally allow to perform spectroscopy of the quantum walk's band structure. By employing such states it would also be possible to simulate relativistic dynamics and their associated phenomena such as Zitterbewegung or the Klein-paradox with the presented set-up [60, 61]. Schemes which could potentially realise such momentum states are under current consideration and development. Finally, by utilising additional quantum levels, the quantum walk could be performed in a higher dimensional space. This could lead to the simulation of strong magnetic fields, and ultimately to the demonstration of the resulting fractional energy level structure, the so-called *Hofstadter Butterfly* [62].

Appendix A.

DDS box

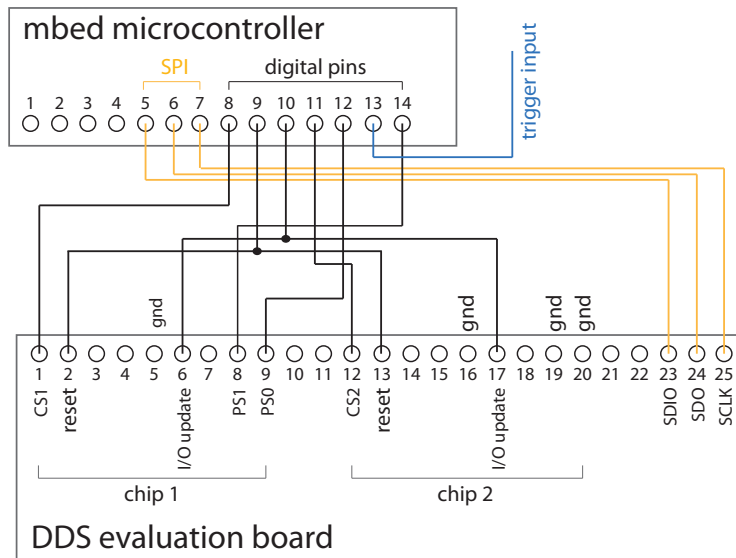


Figure A.1.: Schematics of the DDS-mbed pin connection. Detailed information about individual pins can be found in [48]. The connection to the ground is abbreviated by "gnd".

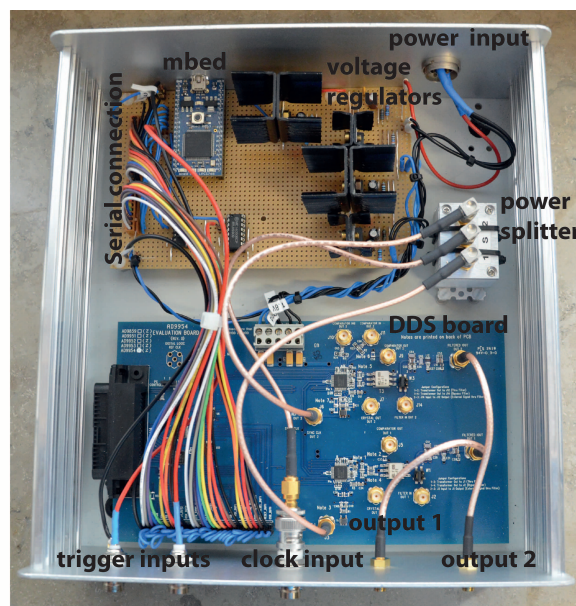


Figure A.2.: Picture showing the interior of the home-built DDS box.

Appendix B.

Characteristic polynomial of the electric walk operator

Here, a recurrence relation shall be derived which gives rise to the form of the characteristic polynomial (5.17) describing the $2m \times 2m$ matrix representing the accelerated quantum walk. Recall (5.15)

$$\hat{W}_{acc,k}^{j,spin} = \hat{C} \cdot \hat{S} \cdot \hat{F} = \begin{pmatrix} C_{1,1} \hat{S}_k^{j,\uparrow} \hat{F}_k^j & C_{1,2} \hat{S}_k^{j,\uparrow} \hat{F}_k^j \\ C_{2,1} \hat{S}_k^{j,\downarrow} \hat{F}_k^j & C_{2,2} \hat{S}_k^{j,\downarrow} \hat{F}_k^j \end{pmatrix}. \quad (\text{B.1})$$

Assume $\det[\hat{C}] = 1$ and all coin elements to be real, then $C_{1,1} = C_{2,2} = c_i$ and $C_{1,2} = -C_{2,1} = c_{ii}$, since $\hat{C} \in SU(2)$. The characteristic polynomial of matrix (5.16) can then be found to be

$$\det \left[\hat{W}_{acc,k}^{j,spin} - \lambda \hat{\mathbb{1}}_{2m} \right] = \det \begin{bmatrix} c_i \hat{S}_k^{j,\uparrow} \hat{F}_k^j - \hat{\mathbb{1}}_m & -c_{ii} \hat{S}_k^{j,\uparrow} \hat{F}_k^j \\ c_{ii} \hat{S}_k^{j,\downarrow} \hat{F}_k^j & c_i \hat{S}_k^{j,\downarrow} \hat{F}_k^j - \hat{\mathbb{1}}_m \end{bmatrix} \quad (\text{B.2})$$

$$= \det \left[\lambda^2 \hat{\mathbb{1}}_m - c_i \hat{F}_k^j \left(\hat{S}_k^{j,\uparrow} + \hat{S}_k^{j,\downarrow} \right) \lambda + \hat{F}_k^j \hat{S}_k^{j,\uparrow} \hat{F}_k^j \hat{S}_k^{j,\downarrow} (c_i^2 + c_{ii}^2) \right] \quad (\text{B.3})$$

$$= \det \left[\lambda^2 \hat{\mathbb{1}}_m - c_i \hat{F}_k^j \left(\hat{S}_k^{j,\uparrow} + \hat{S}_k^{j,\downarrow} \right) \lambda + e^{i2\pi/m} \left(\hat{F}_k^j \right)^2 \right] \quad (\text{B.4})$$

$$= \det \begin{bmatrix} \chi_1 & \zeta_1 & & \xi_m \\ \xi_1 & \chi_2 & \ddots & \\ & \ddots & \ddots & \zeta_{m-1} \\ \zeta_m & & \xi_{m-1} & \chi_m \end{bmatrix}, \quad (\text{B.5})$$

$$\text{with } \chi_n = \lambda^2 + e^{i2\pi(2n+1)/m} \quad (\text{B.6})$$

$$\zeta_n = -c_i e^{ik} e^{i2\pi n/m} \quad (\text{B.7})$$

$$\xi_n = -c_i e^{-ik} e^{i2\pi(n+1)/m}, \quad (\text{B.8})$$

where $n = \{1, \dots, m\}$. This special form of a tridiagonal matrix can be solved by the general solution according to [63], yielding

$$\det \left[\hat{W}_{acc,k}^{j,spin} - \lambda \hat{\mathbb{1}}_{2m} \right] = (-1)^{m+1} (\zeta_m \cdots \zeta_1 + \xi_m \cdots \xi_1) \quad (\text{B.9})$$

$$+ \text{Tr} \left[\begin{pmatrix} \chi_m & -\zeta_{m-1} \xi_{m-1} \\ 1 & 0 \end{pmatrix} \cdots \begin{pmatrix} \chi_m & -\zeta_1 \xi_1 \\ 1 & 0 \end{pmatrix} \begin{pmatrix} \chi_m & -\zeta_m \xi_m \\ 1 & 0 \end{pmatrix} \right]$$

$$\det \left[\hat{W}_{acc,k}^{j,spin} - \lambda \hat{\mathbb{1}}_{2m} \right] = (-1)^m c_1^m (e^{imk} + e^{-mik}) + \text{Tr} \left[\begin{pmatrix} \Xi_m & \Gamma_m \\ \Upsilon_m & \Omega_m \end{pmatrix} \right] \quad (\text{B.10})$$

$$= (-1)^m 2 c_1^m \cos(mk) + (\Xi_m + \Omega_m), \quad (\text{B.11})$$

$$\text{where} \quad \begin{pmatrix} \Xi_m & \Gamma_m \\ \Upsilon_m & \Omega_m \end{pmatrix} = \begin{pmatrix} \chi_m & -\zeta_{m-1}\xi_{m-1} \\ 1 & 0 \end{pmatrix} \cdot \begin{pmatrix} \Xi_{m-1} & \Gamma_{m-1} \\ \Upsilon_{m-1} & \Omega_{m-1} \end{pmatrix}, \quad (\text{B.12})$$

$$\text{and} \quad \begin{pmatrix} \Xi_1 & \Gamma_1 \\ \Upsilon_1 & \Omega_1 \end{pmatrix} = \begin{pmatrix} \chi_1 & -\zeta_m \xi_m \\ 1 & 0 \end{pmatrix}, \quad (\text{B.13})$$

$$\begin{pmatrix} \Xi_0 & \Gamma_0 \\ \Upsilon_0 & \Omega_0 \end{pmatrix} = \begin{pmatrix} 1 & 0 \\ 0 & 1 \end{pmatrix}. \quad (\text{B.14})$$

From this, respective recurrence relations can then be derived. They read

$$\Xi_n = \chi_n \Xi_{n-1} - \zeta_{n-1} \xi_{n-1} \Xi_{n-2} \quad (\text{B.15})$$

$$\Gamma_n = \chi_n \Gamma_{n-1} - \zeta_{n-1} \xi_{n-1} \Gamma_{n-2} \quad (\text{B.16})$$

$$\Upsilon_n = \chi_{n-1} \Upsilon_{n-1} - \zeta_{n-2} \xi_{n-2} \Upsilon_{n-2} \quad (\text{B.17})$$

$$\Omega_n = \chi_{n-1} \Omega_{n-1} - \zeta_{n-2} \xi_{n-2} \Omega_{n-2} \quad (\text{B.18})$$

Since the full set of parameters $\{\chi_n, \zeta_n, \xi_n\}$ is known, any of the above recurrence relations can be calculated. Hereby, calculation of the sum $(\Xi_m + \Omega_m)$, i.e. of the occurring trace in (B.9) is possible. This leads directly to the determination of the characteristic polynomial of (B.1). Owing to the fact that the coefficients $\{\chi_n, \zeta_n, \xi_n\}$ depend intrinsically on the parameter n , standard methods to solve these recurrence relations cannot be applied. However, a consecutive calculation for different forces, i.e. values of m , allows to deduce a general relation describing the characteristic polynomial (see (5.17)). Here, the peculiarity regarding the parity of m becomes apparent. A rigorous proof for the correctness of this relation was delivered by the alternative approach of temporal regrouping of the walk-operator¹.

¹To be published by Prof. R.F. Werner's group (Institut für Theoretische Physik, Leibniz Universität Hannover).

Bibliography

- [1] M. Karski, *State-selective transport of single neutral atoms*. PhD thesis, Universität Bonn, 2010.
- [2] R. P. Feynman, “Quantum Mechanical Computers,” *Optics News*, vol. 11, no. 2, pp. 11–20, 1985.
- [3] T. Hänsch and A. Schawlow, “Cooling of gases by laser radiation,” *Optics Communications*, vol. 13, no. I, pp. 68–69, 1975.
- [4] H. Hess, “Evaporative cooling of magnetically trapped and compressed spin-polarised hydrogen,” *Physical Review B*, vol. 34, no. 5, pp. 3476–3479, 1986.
- [5] K. Davis, M. Mewes, and M. Andrews, “Bose-Einstein condensation in a gas of sodium atoms,” *Physical Review Letters*, vol. 75, no. November, pp. 3969–3973, 1995.
- [6] M. H. Anderson, J. R. Ensher, M. R. Matthews, C. E. Wieman, and E. a. Cornell, “Observation of Bose-Einstein condensation in a dilute atomic vapor,” *Science*, vol. 269, pp. 198–201, July 1995.
- [7] K. W. Madison, F. Chevy, W. Wohlleben, and J. Dalibard, “Vortex Formation in a Stirred Bose-Einstein Condensate,” *Physical Review Letters*, vol. 84, no. 5, pp. 806–809, 2000.
- [8] M. Greiner, O. Mandel, T. Esslinger, T. W. Hänsch, and I. Bloch, “Quantum phase transition from a superfluid to a Mott insulator in a gas of ultracold atoms,” *Nature*, vol. 415, no. 3, pp. 39–44, 2002.
- [9] D. Schrader, S. Kuhr, W. Alt, M. Müller, V. Gomer, and D. Meschede, “An optical conveyor belt for single neutral atoms,” *Applied Physics B: Lasers and Optics*, vol. 73, pp. 819–824, Dec. 2001.
- [10] A. Steffen, A. Alberti, W. Alt, N. Belmechri, S. Hild, M. Karski, A. Widera, and D. Meschede, “Digital atom interferometer with single particle control on a discretized space-time geometry,” *Proceedings of the National Academy of Sciences*, pp. 1–5, June 2012.
- [11] Y. Aharonov, L. Davidovich, and N. Zagury, “Quantum random walks,” *Physical Review A*, vol. 48, no. 2, pp. 1687–1690, 1993.
- [12] A. Childs, “Universal Computation by Quantum Walk,” *Physical Review Letters*, vol. 102, pp. 1–4, May 2009.
- [13] J. Kempe, “Quantum random walks: an introductory overview,” *Contemporary Physics*, vol. 44, pp. 307–327, Mar. 2003.

- [14] F. Zähringer, G. Kirchmair, R. Gerritsma, E. Solano, R. Blatt, and C. F. Roos, “Realization of a Quantum Walk with One and Two Trapped Ions,” *Physical Review Letters*, vol. 104, pp. 1–4, Mar. 2010.
- [15] H. Schmitz, R. Matjeschk, C. Schneider, J. Glueckert, M. Enderlein, T. Huber, and T. Schaetz, “Quantum Walk of a Trapped Ion in Phase Space,” *Physical Review Letters*, vol. 103, pp. 1–4, Aug. 2009.
- [16] B. Sanders, S. Bartlett, B. Tregenna, and P. Knight, “Quantum quincunx in cavity quantum electrodynamics,” *Physical Review A*, vol. 67, pp. 1–4, Apr. 2003.
- [17] A. Schreiber, K. N. Cassemiro, V. Potoček, A. Gábris, P. J. Mosley, E. Andersson, I. Jex, and C. Silberhorn, “Photons Walking the Line: A Quantum Walk with Adjustable Coin Operations,” *Physical Review Letters*, vol. 104, pp. 1–4, Feb. 2010.
- [18] M. Karski, L. Förster, J.-M. Choi, A. Steffen, W. Alt, D. Meschede, and A. Widera, “Quantum walk in position space with single optically trapped atoms,” *Science (New York, N.Y.)*, vol. 325, pp. 174–7, July 2009.
- [19] A. Schreiber, A. Gábris, P. P. Rohde, K. Laiho, M. Stefanák, V. Potocek, C. Hamilton, I. Jex, and C. Silberhorn, “A 2D Quantum Walk Simulation of Two-Particle Dynamics,” *Science (New York, N.Y.)*, vol. 55, Mar. 2012.
- [20] S. Lloyd, “Universal Quantum Simulators,” *Science*, vol. 273, pp. 1073–8, Aug. 1996.
- [21] A. Ahlbrecht, A. Alberti, D. Meschede, V. B. Scholz, A. H. Werner, and R. F. Werner, “Bound Molecules in an Interacting Quantum Walk,” *arxiv: quant-ph/1105.1051*, pp. 1–9, 2011.
- [22] A. Ahlbrecht, V. B. Scholz, and A. H. Werner, “Disordered quantum walks in one lattice dimension,” *Journal of Mathematical Physics*, vol. 52, no. 10, p. 102201, 2011.
- [23] T. Kitagawa, M. S. Rudner, E. Berg, and E. Demler, “Exploring Topological Phases With Quantum Walks,” *Physical Review A*, vol. 82, p. 033429, Mar. 2010.
- [24] E. E. Mendez and G. Bastard, “Wannier-Stark Ladders and Bloch Oscillations in Superlattices,” *Physics Today*, vol. 46, no. 6, p. 34, 1993.
- [25] S. Wilkinson, C. Bharucha, K. Madison, Q. Niu, and M. Raizen, “Observation of atomic Wannier-Stark ladders in an accelerating optical potential,” *Physical review letters*, vol. 76, no. 24, pp. 4512–4515, 1996.
- [26] M. Raizen, C. Salomon, and Q. Niu, “New light on quantum transport,” *Physics Today*, vol. 50, no. 7, p. 30, 1997.
- [27] E. Fama, “Random walks in stock market prices,” *Financial Analysts Journal*, vol. 21, no. 5, pp. 55–59, 1965.
- [28] H. Berg, *Random Walks in Biology*. Princeton University Press, 1993.
- [29] M. Rosenblatt, *Random Processes*. Oxford University Press, 1962.

-
- [30] D. Chruściński, “Geometric Aspects of Quantum Mechanics and Quantum Entanglement,” *Journal of Physics: Conference Series*, vol. 30, pp. 9–16, Feb. 2006.
- [31] C. J. J. Philip G. Burke, *Theory of Electron-Atom Collisions: Pt.1 Potential scattering*. New York: Plenum Press, 1995.
- [32] a. Ahlbrecht, H. Vogts, a. H. Werner, and R. F. Werner, “Asymptotic evolution of quantum walks with random coin,” *Journal of Mathematical Physics*, vol. 52, no. 4, p. 042201, 2011.
- [33] F. Bloch, “Über die Quantenmechanik der Elektronen in Kristallgittern,” *Zeitschrift für Physik A Hadrons and Nuclei*, vol. 52, no. 7, pp. 555–600, 1929.
- [34] L. Förster, *Microwave control of atomic motion in a spin dependent optical lattice*. PhD thesis, Universität Bonn, 2010.
- [35] Stefan Kuhr, *A controlled quantum system of individual neutral atoms*. PhD thesis, Universität Bonn, 2003.
- [36] S. Chu, L. Hollberg, J. Bjorkholm, A. Cable, and A. Ashkin, “Three-dimensional viscous confinement and cooling of atoms by resonance radiation pressure,” *Physical Review Letters*, vol. 55, no. 1, 1985.
- [37] H. J. Metcalf and P. van der Straten, *Laser Cooling and Trapping*. New York: Springer-Verlag, 1999.
- [38] D. A. Steck, “Cesium D Line Data.”
- [39] R. Grimm, M. Weidemüller, and Y. Ovchinnikov, “Optical dipole traps for neutral atoms,” *Advances in Atomic, Molecular and Optical Physics*, vol. 42, no. 95, 2000.
- [40] D. Meschede, *Optik, Licht und Laser*. Wiesbaden: Vieweg+Teubner, 3. ed., 2008.
- [41] L. Allen and J. H. Eberly, *Optical Resonance and Two-Level Atoms*. Dover Publications, 1987.
- [42] S. Kuhr, W. Alt, D. Schrader, I. Dotsenko, Y. Miroshnychenko, a. Rauschenbeutel, and D. Meschede, “Analysis of dephasing mechanisms in a standing-wave dipole trap,” *Physical Review A*, vol. 72, pp. 1–12, Aug. 2005.
- [43] N. F. Ramsey, “Successive oscillatory fields at radio to optical frequencies,” *Applied Physics B Laser and Optics*, vol. 60, no. 2-3, pp. 85–88, 1995.
- [44] D. Döring, *Ein Experiment zum zustandsabhängigen Transport einzelner Atome*. PhD thesis, Universität Bonn, 2007.
- [45] F. Schwabl, *Quantenmechanik - QM I*. Heidelberg: Springer, 6. ed., 2006.
- [46] W. Alt, *Optical control of single neutral atoms*. PhD thesis, Universität Bonn, 2004.
- [47] D. Schrader, *A neutral atom quantum register*. PhD thesis, Universität Bonn, 2004.
- [48] “Direct Digital Synthesizer AD9954 - Data Sheet,” tech. rep., Analog Devices, 2009.

- [49] “A Technical Tutorial on Digital Signal Synthesis,” tech. rep., Analog Devices, 1999.
- [50] “Hewlett Packard 8640B - Specifications,” tech. rep., Hewlett Packard.
- [51] D. W. Ricker, *Echo Signal Processing*. Kluwer Academic Publishers, 2003.
- [52] J. J. Sakurai, *Modern Quantum Mechanics*. 1994.
- [53] T. Savard, K. O’Hara, and J. Thomas, “Laser-noise-induced heating in far-off resonance optical traps,” *Physical Review A*, vol. 56, pp. R1095–R1098, Aug. 1997.
- [54] M. E. Gehm, T. A. Savard, and J. E. Thomas, “Dynamics of noise-induced heating in atom traps,” vol. 58, no. 5, pp. 3914–3921, 1998.
- [55] M. A. Schlosshauer, *Decoherence and the Quantum-to-Classical Transition*. Frontiers Collection, Springer, 2007.
- [56] V. Kendon, “Decoherence in quantum walks - a review,” *Mathematical Structures in Computer Science*, vol. 17, no. 6, pp. 1169–1220, 2007.
- [57] C. Clopper and E. Pearson, “The use of confidence or fiducial limits illustrated in the case of the binomial,” *Biometrika*, vol. 26, no. 1, 1934.
- [58] C. Kittel, *Einführung in die Festkörperphysik*. Oldenbourg Verlag, 2005.
- [59] F. Faisal and J. Kaminski, “Floquet-Bloch theory of high-harmonic generation in periodic structures,” *Physical Review A*, vol. 56, no. 1, pp. 748–762, 1997.
- [60] F. Strauch, “Relativistic quantum walks,” *Physical Review A*, vol. 73, pp. 2–5, May 2006.
- [61] D. Witthaut, “Quantum walks and quantum simulations with Bloch-oscillating spinor atoms,” *Physical Review A*, vol. 82, p. 033602, Sept. 2010.
- [62] D. R. Hofstadter, “Energy levels and wave functions of Bloch electrons in rational and irrational magnetic fields,” *Physical Review*, vol. 14, no. 6, pp. 2239–2249, 1976.
- [63] L. G. Molinari, “Determinants of block tridiagonal matrices,” *Linear Algebra and its Applications*, vol. 429, no. 8-9, 2008.

Acknowledgements

I would like to thank all people who helped me directly or indirectly to complete this project. Particularly, I want to thank Prof. Meschede for providing me with this very interesting topic, and also for the support throughout the last year. The same share goes to Prof Schlemmer, who made it possible in the first place that I was able to follow my personal interests, and write the thesis at an external institution.

All my gratitude goes to the people working on the same experiment, Adreas Steffen and Noomen Belmechri, for their help and guidance in the lab, and open ears for new and long discussions. Particularly Adreas was always a great help, and without him the data acquisition would have been much more difficult. I would also like to thank Dr. Andrea Alberti, who was never short of new ideas, and always of great assistance. Dr. Wolfgang Alt deserves my gratitude for not being shy to share his tremendous experimental knowledge.

Long working days can be tiring and exhausting, but it was always fun in the office with Rene Reimann, Tobias Kampschulte, Carsten Robens und Stefan Brakhane. I really enjoyed the "off-physics" debates and heated discussions.

I am indebted to all the people who supported me personally not just over the last 12 months. Without the help and support of friends and family this thesis could not have been completed. At the very end, I want to thank my brother and my parents for their unmeasurable and undivided support throughout the years. I could not have accomplished all this without them.

Thank you.

Declaration

I hereby declare that this thesis is my original work and that I have not received outside assistance. Only the sources cited have been used and parts that are direct quotes or paraphrases are identified as such.

Cologne, 23.10.2011

(Maximilian Genske)